

Strong lensing of gravitational waves: A new probe of cosmology and the nature of dark matter

A Thesis

Submitted to the
Tata Institute of Fundamental Research, Mumbai
for the degree of Doctor of Philosophy

In Physics

by

Souvik Jana

International Centre for Theoretical Sciences,
Tata Institute of Fundamental Research, Bengaluru

June 16, 2025

Dedicated to my parents

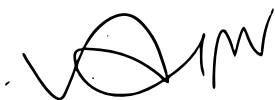
Declaration

This thesis is a presentation of my original research work. Wherever contributions of others are involved, every effort is made to indicate this clearly, with due reference to the literature, and acknowledgement of collaborative research and discussions.

The work was done under the guidance of Professor Parameswaran Ajith, at the International Centre for Theoretical Sciences, Tata Institute of Fundamental Research, Bangalore.

Souvik Jana.
Souvik Jana

In my capacity as supervisor of the candidate's thesis, I certify that the above statements are true to the best of my knowledge.



Parameswaran Ajith
Date: 16 June, 2025

Acknowledgements

The completion of this doctoral thesis represents not only years of dedicated research and academic pursuit, but also the culmination of a journey made possible through the support, guidance, and encouragement of many individuals. I am deeply grateful to all those who have contributed to my growth as a researcher. Looking back, I am humbled by the countless interactions, discussions, and moments of support that have shaped this journey, made meaningful by the mentors, colleagues, friends, and family who stood beside me.

First and foremost, I would like to express my deepest and most heartfelt gratitude to my supervisor, Prof. Parameswaran Ajith, whose mentorship has profoundly shaped my development as a researcher and scientist. His remarkable ability to approach complex research problems with methodical clarity has not only guided my research but has fundamentally influenced my scientific thinking. What stands out most is his exceptional intuition – his ability to distill complicated research problem into their essential elements and predict outcomes that invariably align with the results of rigorous numerical calculations. While I have strived to absorb this skill, it remains a source of continuous inspiration. His mentorship offered a perfect balance between guidance and independence, creating an environment where I felt both supported and free to explore. Beyond the technical aspects of research, he has been pivotal in shaping my academic journey through his guidance on crucial decisions, his emphasis on research ethics, and his invaluable inputs in developing my presentation skills and writings. His influence extends far beyond what can be captured in words. I could not have wished for a more supportive, understanding, and brilliant supervisor – someone who not only guided my research but also showed me what true mentorship means.

I would like to express my sincere gratitude to my co-supervisor, Prof. Tejaswi Venumadhav, for his invaluable guidance throughout my research projects. Each discussion with him was a learning experience, enriching my understanding not only of my research but of many other fields as well. His remarkable breadth and depth of knowledge across different areas has been truly inspiring and has greatly influenced my scientific perspective.

A special thank you goes to Prof. Shasvath Kapadia, who was a postdoc at ICTS during my early PhD years and was my close mentor. His ability to generate novel research ideas and chart clear paths forward never ceased to amaze me. During those crucial initial years, his guidance and significant contributions helped shape my re-

search journey. I am also grateful to Prof. Surhud More for his valuable insights and contributions to my work. I feel incredibly fortunate to have had such a remarkable team of mentors and collaborators: Ajith, Shasvath, Tejaswi, and Surhud, each bringing their unique perspective and expertise to my research.

I am deeply grateful to the past and present members of our Astrophysical Relativity group at ICTS who have enriched my PhD journey. The early postdocs - Apratim, Arif, and Kanhaiya - taught me many practical things of Gravitational wave research that was invaluable. A special thanks to Akash Kumar Mishra for our many engaging discussions, both academic and personal - our shared outlook on science, sports, and life made the journey more beautiful. I'm thankful to the other postdocs - Shalabh, Vaishak, Krishnendu, Prasad, Rajesh, Anuj, and Samanwaya - for their insights and contributions to our various group activities. The former graduate students - Aditya Vijaykumar, Srashti, and Aditya Sharma, Soumyadip - were always generous with their help and made our discussions, whether research-related or casual, truly enriching. I also want to thank my juniors - Alorika, Koustav, Ankur, Akash Maurya and Neha - whose company during lunch and dinner conversations added joy to our daily routine. I thank Bala and Prayush for their valuable insights, discussions, and continuous encouragement throughout this journey. While this list cannot capture everyone who has contributed to my growth, I extend my heartfelt thanks to all past and present members of our research group whom I've had the privilege to interact with during my PhD journey. Having such an interesting and supportive group of people around made the research journey not just productive but also thoroughly enjoyable.

I am deeply grateful to the people who made ICTS feel like home, especially Ud-depta, Mukesh, and Anup, who became more than just colleagues. With them, every day brought new joy - from cooking meals together to cycling adventures, from casual evening hangouts to movie nights, and trips, countless outings and late night card games. Our discussions, ranging from science to sports, politics and non sciences, created a tapestry of unforgettable memories. Their friendship made the challenges of PhD life much easier to navigate. Our circle grew wider with time, welcoming Ankur, Koustav, Alorika, Sumi, Divyajyoti and Kaushik, each adding their own unique warmth to our group. The memories we created together have been a cherished part of this journey, and I can't imagine my PhD years without their presence and support. Their friendship transformed what could have been a solitary academic pursuit into an adventure filled with laughter, understanding, and shared experiences.

I want to express my gratitude to my batchmates - Ankush, Harshit, Mahaveer, Bhanu, Omkar, Priyadarshi, and Tuneer - for their support throughout this journey, both academic and personal. I am thankful to Basudev da, Joydeep da, Kohinoor da, Sparsh, Saikat and Soumav for their help and encouragement, and to my office mates Bikram, Sridhar, and Shasvat for creating a pleasant work environment. The courses taught by ICTS Professors significantly enriched my knowledge and scientific thinking, and I particularly thank Loga for the valuable discussions during my early days. I am grateful to our center director, Prof. Rajesh Gopakumar, for his support and encouragement. The vibrant scientific atmosphere at ICTS was made possible by all its members, and

I am thankful to the entire community. The support from the scientific, technical, and administrative staff has been invaluable. Special thanks to Prasanth and Hemanta for their prompt help with laptop and computing issues. I appreciate the canteen and cafeteria staff for providing healthy and delicious meals. I also want to thank Basavraj and Suresh for their help with various matters. A special mention to all my football companions whose company brought joy and refreshing breaks from research.

Before coming to ICTS, my foundation in physics was shaped by many remarkable teachers. I am deeply grateful to my JNU professors - Prof. Debasish Ghoshal, Prof. Ram Ramaswamy, Prof. Sanjay Puri, and Prof. Shankar Prasad Das - for deepening my understanding of physics. My journey in physics began at Visva Bharati, and I am thankful to all my professors there for sharpening my fundamental knowledge. I would particularly like to thank Sudipta di, whose support and encouragement continue to this day. A special mention and thanks to Late Somnath da, whose course on Fundamentals of Astrophysics sparked my passion for research in this field.

I would like to express my profound gratitude to all my high school teachers whose quality instruction and unwavering support built my foundation in science and other subjects. While I am indebted to all of them, I wish to specially acknowledge Mr. Sujit Manna, Mr. Sanjib Mahato, Mr. Billweswar Mondal, Mr. Buddhadev Das, Mr. Utpal Manna, Mrs. Nandita Das, Mrs. Mala Hatui, Mrs. Kanika Jana, and our beloved principal, Mr. Biswajit Jana. My interest in science, particularly physics, was ignited by Mr. Shivshankar Kar, to whom I owe immense thanks. I am also grateful to Mr. Soumen Manna, Mr. Chandan Darbar, Mr. Dilip Patra, Mr. Debutta, Mr. Bamdev Das and Mr. Manik Manna, along with many others whose names I may have overlooked but whose knowledge has profoundly enriched me. I extend special thanks to my primary school teachers, Mr. Nagendranath Adak and Mr. Anath Bandhu Mandal, whose love and encouragement extended beyond academics during a crucial, formative period when I lacked focus. Finally, I am deeply grateful to all the teachers with whom I have interacted throughout my journey; the lessons I learned from them have been invaluable to my academic development and success. I continue to be inspired by their strong character, knowledge, and moral principles.

My academic journey has been enriched by wonderful friendships that have enriched both my academic and personal life. From my undergraduate years, I am grateful to Deepanjan, Sayan Ghosh, Nilanjan, Rishiraj, Sayan Chowdhuri, Subhodeep, and many others who made my BSc experience memorable. My MSc years were made memorable by Himanshu, Amit, Palash, Ritam, Arindam, Prasenjit, Debmalya, Amit Haldar and Amlan whose friendship I continue to cherish.

I am thankful to my school friends - Pradip, Sourav, Krishnendu, Suvasish and others - who have stood by my side since the very beginning. Through every up and down, they have been an unwavering source of support, lifting my spirits when needed and offering constant encouragement. Their friendship has enriched my life in countless ways. I would also like to express my heartfelt thanks to all the friends I've met throughout my journey.

I am forever grateful to my late Dadu, Thakumoni, Mama-dadu, and Dida, who showed me endless affection and always believed in my abilities. Special thanks to my Mejo-Jethu, Dr. Ananda Mohan Jana, who remains my strongest supporter and has always encouraged me to pursue my dreams in physics. His own passion for science has been truly inspiring. I am thankful to all my family members who have contributed to my journey in their own special ways.

Words fall short when it comes to expressing my gratitude to my Maa and Baba. Everything I am today and everything I have achieved is because of them. Their selfless love, endless support, and unwavering faith in me have brought me to this point in life. Thank you for always believing in me and encouraging me to excel. This thesis is dedicated to both of you - I hope it makes you proud.

Finally, I would like to thank all Indian citizens who believe in science and help in nurturing scientific temperament in our society.

Abstract

The observation of gravitational waves (GWs) has opened up an entirely new window into the universe, validating general relativity and enriching our understanding of astrophysics and cosmology. Some of the observable GWs will be strongly lensed, where these waves are deflected by massive celestial structures like galaxies and galaxy clusters, producing multiple observable copies of the GW signals. Third-generation detectors are expected to detect millions of GW events during their observing period, with tens of thousands strongly lensed. The precise number of lensed events as well as the distribution of lensing time delay (between multiple images) contain imprints of cosmology and the nature of dark matter (DM). Thus, strong lensing of GWs holds remarkable potential for cosmological investigation.

This thesis examines the potential of using a population of strongly lensed GWs as a probe of cosmology and properties of DM. We develop statistical methods to measure cosmological parameters and to constrain the nature of DM from the observed number of strongly lensed events and the lensing time delay distribution. We also forecast expected constraints from third-generation GW detectors, and discuss the potential systematic errors in such a measurement and possible solutions to some of them.

Chapter 1 provides a pedagogical introduction to the physics and astronomy of GWs. Chapters 2 and 3 present a similar introduction to the theory of gravitational lensing and cosmology, thus introducing the necessary tools and concepts. In Chapter 4 we develop a statistical framework to perform cosmography using strongly lensed GWs from binary black hole (BBH) mergers. We model the expected population of lensed events and their time delay distributions, demonstrating how future observations can constrain cosmological parameters through Bayesian inference. Our analysis also addresses key systematic effects involved in this measurement, and possible solutions to some of them. Chapter 5 extends this framework to probe the nature of DM, showing how strongly lensed GWs can constrain the mass of the DM particle. We present expected constraints for both warm and fuzzy DM models and examine the impact of systematic effects on these measurements. Chapter 6 presents some concluding remarks and future work. Our work demonstrates that future GW observations will provide a powerful new window into cosmology and DM, complementing existing probes while exploring previously inaccessible regimes.

Contents

1	Gravitational Waves	15
1.1	Linearized theory	15
1.2	Sources of gravitational waves	18
1.2.1	Human made sources	18
1.2.2	Gravitational wave bursts from core collapse	18
1.2.3	Compact binary coalescences	18
1.2.4	Black hole ringdown	19
1.2.5	Stochastic background	20
1.3	Gravitational wave detectors	20
1.3.1	Future Networks	21
1.3.2	Space based detection	22
1.4	Gravitational wave astronomy: Achievements and future prospects	23
2	Gravitational lensing	27
2.1	Propagation of gravitational waves in curved spacetime	27
2.2	Geometric optics in curved spacetime	28
2.3	Focusing of gravitational waves and breakdown of geometrical optics	29
2.4	Derivation of the lens equation	30
2.4.1	Approximate metrics of isolated, slowly moving, non-compact matter distributions	30
2.4.2	Deflection of gravitational waves by quasistationary, isolated mass distributions	31
2.4.3	Lens equation	33
2.5	Properties of lens mapping	35
2.5.1	Lensing potential	35

2.5.2	Magnification and distortion	36
2.5.3	Time delay function	39
2.5.4	Necessary and sufficient conditions for multiple imaging or strong lensing	41
2.6	Lensing degeneracies	41
2.6.1	Similarity transformations	42
2.6.2	Mass-sheet degeneracy	43
2.6.3	Other degeneracies	43
2.7	Simple lens models	44
2.7.1	Point mass lens	44
2.7.2	Axially symmetric lenses	46
2.7.3	Singular isothermal sphere	50
3	Cosmology and Structure Formation	53
3.1	Cosmological Framework	53
3.1.1	The Hubble parameter and cosmic density parameters	54
3.1.2	Cosmic history and evolution	55
3.2	Structure formation in linear regime	56
3.2.1	Particle motion in expanding universe	57
3.2.2	Vlasov equation	57
3.2.3	Multi-fluid extension	59
3.2.4	Evolution of dark matter perturbations	60
3.3	Simpler way to understand the growth of dark matter perturbations	61
3.3.1	Mode outside the horizon: $\lambda > d_H$	61
3.3.2	Mode inside the horizon; $\lambda < d_H$	62
3.4	The free streaming length scale	63
3.5	The Halo Mass Function	65
3.5.1	Approximative analytical approach	66
3.5.2	Fits from numerical simulations	67
3.5.3	Dependence on redshift and cosmology	68
4	Cosmography Using Strongly Lensed Gravitational Waves from Binary Black Holes	71

4.1	Introduction	71
4.2	Bayesian inference of cosmological parameters	75
4.3	Modelling the expected number of lensed events and lensing time delays	76
4.3.1	Expected number of lensed events:	76
4.3.2	Expected distribution of lensing time delays:	79
4.4	Expected constraints on cosmological parameters	81
4.5	Cosmography systematics	84
4.5.1	Effect of source distribution models	85
4.5.2	Effect of errors in measuring the source redshift distribution	87
4.5.3	Effect of lens distribution	89
4.5.4	Effect of contamination	92
4.6	Conclusions	94
5	Probing the nature of dark matter using strongly lensed gravitational waves from binary black holes	97
5.1	Introduction	97
5.2	Warm dark matter	100
5.3	Bayesian inference of m_{WDM}	101
5.4	Modeling the expected number of lensed events and time delay distribution	102
5.4.1	Expected number of lensed events	102
5.4.2	Expected distribution of lensing time delays	102
5.5	Expected constraints on warm dark matter	103
5.6	Systematic errors	107
5.6.1	Effect of source distribution models	108
5.6.2	Effect of measurement errors in reconstructing the source redshift distribution	110
5.6.3	Lens distribution	111
5.6.4	Correlation with cosmological parameters	113
5.6.5	Effect of contaminations	114
5.6.6	Effect of core	118
5.7	Conclusions	120
6	Conclusions and Future Directions	123

List of Figures	III
List of Tables	VII
Bibliography	IX

1 | Gravitational Waves

1.1 *Linearized theory*

In 1905, Einstein published his groundbreaking paper "On the Electrodynamics of Moving Bodies," introducing the theory of special relativity (SR). This work revolutionized physics by unifying space and time into a single four-dimensional spacetime fabric—the only entity with absolute meaning, in contrast to the previously held concepts of absolute space and absolute time. Einstein formulated SR on two fundamental postulates: the laws of physics are identical in all non-accelerating reference frames, and the speed of light remains constant in vacuum.

Building upon this foundation, Einstein made an even more remarkable advancement by developing the theory of general relativity (GR), which provides our current understanding of gravitation in modern physics. The cornerstone of this theory was the principle of equivalence, which states that a gravitational field in a sufficiently small region of spacetime is indistinguishable from an accelerated reference frame. By extending SR (which applies in the absence of gravitation) to accelerating observers, Einstein discovered that gravity manifests as curved spacetime. The formulation of GR represented a monumental breakthrough in modern physics. It transformed our understanding of gravity from Newton's concept of a force to a geometric phenomenon arising from the dynamic curvature of spacetime induced by the presence of matter. Einstein expressed this theory using tensor mathematics, adhering to the principle of general covariance, which requires that physical laws maintain their form in all reference frames. This culminated in Einstein's field Equations ¹:

$$G_{\mu\nu} \equiv R_{\mu\nu} - \frac{1}{2}g_{\mu\nu}R = \frac{8\pi G}{c^4}T_{\mu\nu}. \quad (1.1)$$

This remarkable equation establishes the fundamental relationship between geometry (represented by the left-hand side) and matter (encoded in the stress-energy tensor). It completes the unification of gravity and geometry, revealing spacetime as an active participant in physical phenomena rather than a passive background. This relationship

¹ $G_{\mu\nu}$ represents the Einstein tensor, constructed from the Ricci tensor ($R_{\mu\nu}$), the Ricci scalar (R), and the metric tensor ($g_{\mu\nu}$). The constants G and c denotes gravitational constant and the speed of light in vacuum. $T_{\mu\nu}$ is the stress energy tensor. The indices μ and ν range over all four spacetime coordinates, taking values (0,1,2,3), where 0 corresponds to the temporal component and (1,2,3) represent the spatial components

represents one of the most profound paradigm shifts in the history of physics.

The many remarkable predictions of GR include the existence of GWs [1, 2]. In the weak field limit of his field equations, Einstein showed that spacetime perturbations propagate as waves. Specifically, in the weak field regime, the metric can be decomposed into the flat Minkowski metric plus a small perturbation that satisfies a wave equation, analogous to retarded potentials in electromagnetism.

To derive GWs from the field equations, we need to expand the field equations around flat spacetime, therefore we write

$$g_{\mu\nu} = \eta_{\mu\nu} + h_{\mu\nu}, \quad |h_{\mu\nu}| \ll 1. \quad (1.2)$$

Expanding the equations of motion to linear order in $h_{\mu\nu}$ yields the linearized theory. In what follows, we present the key aspects of linearized theory, following [3, 4]. Linearized theory is invariant under Poincaré transformation (group formed by translation and Lorentz transformations). The allowed gauge symmetry is then

$$x^\mu \rightarrow x'^\mu = x^\mu + \xi^\mu. \quad (1.3)$$

The linearized field equation can be written more compactly by defining:

$$\begin{aligned} h &= \eta^{\mu\nu} h_{\mu\nu}, \\ \bar{h}_{\mu\nu} &= h_{\mu\nu} - \frac{1}{2} \eta_{\mu\nu} h. \end{aligned} \quad (1.4)$$

Expanding the field equation around flat spacetime to linear order in $h_{\mu\nu}$ and making use of the gauge freedom ², yields the wave equation:

$$\square \bar{h}_{\mu\nu} = -\frac{16\pi G}{c^4} T_{\mu\nu}. \quad (1.5)$$

Outside the source region, this reduces to:

$$\square \bar{h}_{\mu\nu} = 0. \quad (1.6)$$

The harmonic gauge condition remains invariant under coordinate transformations $x^\mu \rightarrow x^\mu + \xi^\mu$ where:

$$\square \xi_\mu = 0. \quad (1.7)$$

Under this transformation, $h_{\mu\nu}$ transforms as:

$$\bar{h}_{\mu\nu} \rightarrow \bar{h}'_{\mu\nu} = \bar{h}_{\mu\nu} - (\partial_\mu \xi_\nu + \partial_\nu \xi_\mu - \eta_{\mu\nu} \partial_\rho \xi^\rho). \quad (1.8)$$

Defining:

$$\xi_{\mu\nu} \equiv \partial_\mu \xi_\nu + \partial_\nu \xi_\mu - \eta_{\mu\nu} \partial_\rho \xi^\rho, \quad (1.9)$$

we can subtract now $\xi_{\mu\nu}$ from $h_{\mu\nu}$ to impose four conditions on $h_{\mu\nu}$. We can choose

²The Lorentz (Hilbert/harmonic/De Donder) gauge condition $\partial^\nu \bar{h}_{\mu\nu} = 0$ reduces the degrees of freedom from 10 to 6 independent components of the symmetric 4×4 matrix $h_{\mu\nu}$

ξ_μ to impose $\bar{h} = 0$ (implying $\bar{h}_{\mu\nu} = h_{\mu\nu}$) and $h^{0i} = 0$ ($i \in 1, 2, 3$). The Lorentz gauge condition then implies h_{00} is time-independent, representing the static Newtonian potential. Setting $h_{00} = 0$ for GWs, we obtain:

$$\square h_{\mu\nu} = 0. \quad (1.10)$$

Making use of the remaining gauge degrees of freedom, we can choose the following gauge, called the transverse-traceless (TT) gauge, in which the metric perturbations obey the following conditions:

$$\begin{aligned} h^{0\mu} &= 0, \\ h_i^i &= 0 \quad (\text{Traceless}), \\ \partial^j h_{ij} &= 0 \quad (\text{Transverse}). \end{aligned} \quad (1.11)$$

The solution, with two degrees of freedom, takes the plane wave form:

$$h_{ij}^{TT}(x) = e_{ij}(\mathbf{k}) \exp(i\mathbf{k}\mathbf{x}), \quad (1.12)$$

where $k^\mu = (\frac{\omega}{c}, \mathbf{k})$, $\frac{\omega}{c} = |\mathbf{k}|$, and $e_{ij}(\mathbf{k})$ is the polarization tensor. For GWs propagating along $\hat{\mathbf{n}} = \frac{\mathbf{k}}{|\mathbf{k}|}$ aligned with the z-axis:

$$h_{ij}(t, z) = \begin{bmatrix} h_+ & h_\times & 0 \\ h_\times & -h_+ & 0 \\ 0 & 0 & 0 \end{bmatrix}_{ij} \cos[\omega(t - z/c)]. \quad (1.13)$$

Here h_+ and h_\times represent the amplitudes of plus ('+') and cross ('×') polarizations. The effect of '+' and '×' polarized GW on a ring of test particle is shown in Figure 1.1.

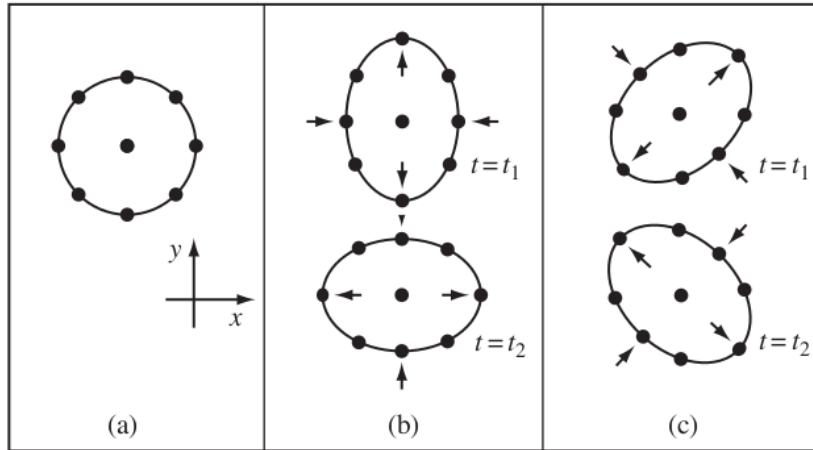


Figure 1.1: (a) Free particles on a circle in the $x - y$ plane before a GW traveling in the z direction reaches to them. (b) Distortions of the circle produced by a '+' polarized GW. The two pictures represent the same wave at phases separated by 180° . (c) Same as (b) but for '×' polarized GW. This figure is taken from [4].

1.2 Sources of gravitational waves

GWs can be produced by various astrophysical sources, ranging from man-made devices to violent cosmic events. While theory suggests many potential sources, only those producing sufficiently strong signals can be detected by current or planned detectors. Here we briefly discuss the major classes of sources and provide order-of-magnitude estimates of their GW emission. This overview draws substantially from [5].

1.2.1 Human made sources

The possibility of artificially generating detectable GWs can be quickly dismissed through simple calculations. Consider an extreme example of a rotating system with two masses of 10^3 kg each at opposite ends of a 10m beam, rotating at 10 Hz. The nonspherical velocity is $v_{\text{nonsph}}^2 \approx 10^5 \text{ m}^2\text{s}^{-2}$. At one Earth diameter away, this produces waves with amplitude:

$$h \sim 5 \times 10^{-43}. \quad (1.14)$$

This amplitude is far too small for any conceivable detector. Nature, however, provides much more powerful sources through astrophysical systems.

1.2.2 Gravitational wave bursts from core collapse

Core-collapse supernovae and the formation of neutron stars or black holes can produce bursts of GWs if the collapse is non-spherical. For a typical supernova at a distance of 10 kpc within our galaxy, assuming an energy release of $10^{-7} M_{\odot}$ at frequency 1 kHz for duration 1 ms [5]:

$$h \sim 6 \times 10^{-21} \left(\frac{E}{10^{-7} M_{\odot}} \right)^{1/2} \left(\frac{1 \text{ ms}}{T} \right)^{1/2} \left(\frac{1 \text{ kHz}}{f} \right) \left(\frac{10 \text{ kpc}}{r} \right). \quad (1.15)$$

While this amplitude is potentially detectable by current instruments, the event rate within 10 kpc is expected to be quite low. Simulations suggest that GWs might carry away between 10^{-7} and 10^{-5} of the total available mass-energy in core-collapse events and the typical frequency might lie in the range of $\sim 200 - 1000$ Hz [6, 7].

1.2.3 Compact binary coalescences

Compact binary systems are among the most promising sources of GWs. As two compact objects (neutron stars or black holes) orbit each other, they emit gravitational radiation and slowly spiral inward. The GW amplitude from a binary is characterized by:

$$h_{\text{binary}} \sim \frac{1}{r} \mathcal{M}^{5/3} \Omega^{2/3}. \quad (1.16)$$

Here, \mathcal{M} denotes the chirp mass while Ω represents the orbital angular frequency. The chirp mass is expressed as:

$$\mathcal{M} = \mu^{3/5} M^{2/5} = \nu^{3/5} M, \quad (1.17)$$

where, $\mu = \frac{m_1 m_2}{m_1 + m_2}$, is the reduced mass, $M = m_1 + m_2$, is the total mass and $\nu = \frac{\mu}{M}$ is the symmetric mass ratio.

For circular orbits near the last stable orbit ($R = 6M$), the frequency becomes:

$$f_{\text{LSO}} \sim 220 \left(\frac{20M_{\odot}}{M} \right) \text{ Hz}. \quad (1.18)$$

Binary systems provide excellent tests of general relativity through systems like the Hulse-Taylor pulsar PSR B1913+16. This binary system's orbital decay matches theoretical predictions within measurement precision, providing strong validation of general relativity.

Supermassive black holes (SMBHs) with masses 10^6 - $10^9 M_{\odot}$ are believed to exist in most galactic centers. When galaxies merge, their central black holes can form binaries that eventually merge through GW emission. For a binary with two $10^6 M_{\odot}$ black holes, characteristic frequencies are:

$$f_{\text{LSO}} = 4 \text{ mHz} \quad (\text{Last Stable Orbit}), \quad (1.19)$$

$$f_{\text{QNM}} = 24 \text{ mHz} \quad (\text{Quasi-Normal Mode}), \quad (1.20)$$

where f_{QNM} is the frequency of the dominant quasi-normal mode produced by the black hole ring down.

1.2.4 Black hole ringdown

When black holes form or are perturbed, they emit characteristic ringdown radiation. The characteristic strain amplitude for stellar-mass black holes forms at a distance 200 Mpc from Earth due to merger of compact objects in binary the amplitude is given by:

$$h_{\text{eff}} \approx 10^{-21} \left(\frac{\nu}{0.25} \right) \left(\frac{M}{20M_{\odot}} \right) \left(\frac{200 \text{ Mpc}}{r} \right), \quad (1.21)$$

where ν is the symmetric mass ratio of the merging compact objects and M is the final mass of the resulting black hole.

Supermassive black holes can produce significantly stronger signals despite cosmological distances:

$$h_{\text{eff}} \approx 3 \times 10^{-17} \left(\frac{\nu}{0.25} \right) \left(\frac{M}{2 \times 10^6 M_{\odot}} \right) \left(\frac{6.5 \text{ Gpc}}{r} \right). \quad (1.22)$$

For $10M_{\odot}$ binary mergers, the radiation emerges at 500 Hz, potentially detectable by ground-based instruments. At cosmological distances ($z \sim 1$), a $100M_{\odot}$ black hole plunging into a 10^6M_{\odot} black hole emits at 15 mHz (redshifted from 30 mHz), within the detection range of the upcoming space-based detector LISA. More dramatically, 10^6M_{\odot} SMBH mergers produce signals of 3×10^{-17} at 7.5mHz, allowing detailed analysis of pre- and post-merger masses and spins to test fundamental black hole properties.

1.2.5 Stochastic background

Beyond individual sources, a stochastic background of GWs is expected from the superposition of many unresolved sources and potentially from fundamental processes in the early universe. The energy density (as a fraction of critical density of the universe) in GWs is characterized by:

$$\Omega_{\text{gw}}(f) = \frac{10\pi^2}{3H_0^2} f^3 S_{\text{gw}}(f). \quad (1.23)$$

Here $S_{\text{gw}}(f)$ is the mean square GW amplitude per unit frequency. Constraints from Big Bang nucleosynthesis require $\Omega_{\text{gw}} < 10^{-5}$. Detection of this background would provide unique information about the very early universe and high-energy physics inaccessible to conventional experiments.

1.3 Gravitational wave detectors

Modern GW detection represents a triumph of precision engineering and physics. These instruments measure spacetime distortions through the strain $h = \frac{\delta L}{L}$, where L denotes reference point separation and δL represents the induced displacement. Current detectors achieved extraordinary displacement sensitivities better than 10^{-18} meters to detect typical GW strains of $\sim 10^{-21}$.

Ground-based observatories utilize advanced Michelson interferometry with suspended mirrors as test masses. The Advanced LIGO detectors [8] employ 4km arms, complemented by Virgo [9] and KAGRA [10] with 3km arms. These detectors are engineered with remarkable precision, considering that their required displacement sensitivity is smaller than a proton's radius ($\sim 8.5 \times 10^{-16}$ m).

The interferometers implement sophisticated isolation systems, with mirrors suspended from multi-stage pendulums. Above ~ 1 Hz (the resonant frequency), these effectively create local inertial frames. Combined seismic isolation achieves remarkable 10^{12} -fold reduction in ground motion effects between 1 Hz and 10 Hz [11, 12].

The sensitivity of a detector is characterised by its frequency-dependent noise power spectral density $S(f)$. The detector noise budget [13] comprises:

$$S_{\text{total}}(f) = S_{\text{seismic}}(f) + S_{\text{thermal}}(f) + S_{\text{quantum}}(f) + S_{\text{Newtonian}}(f) + S_{\text{technical}}(f). \quad (1.24)$$

Here, $S_{\text{seismic}}(f)$ is for seismic noise due to direct coupling of seismic vibrations to the detector. $S_{\text{thermal}}(f)$ encompasses mirror and suspension thermal noise [14], dominant in the mid-frequency range (50 – 500 Hz) due to Brownian motion in the mirror coatings and suspensions [15]. $S_{\text{quantum}}(f)$ combines shot noise and radiation pressure noise [16], limiting sensitivity at high frequencies (> 500 Hz) and low frequencies (< 50 Hz) respectively. $S_{\text{Newtonian}}(f)$ represents gravitational gradient noise, i.e. fluctuation in local gravitational field from ground and atmospheric density perturbations [17], particularly significant below 20 Hz and fundamentally limiting terrestrial detectors. $S_{\text{technical}}(f)$ includes instrumental effects like laser noise, scattered light, and stochastic electromagnetic (EM) forces and deposition of energy by energetic particles, etc. which can be mitigated through careful engineering but never completely eliminated.

1.3.1 Future Networks

The Cosmic Explorer (CE) [18] is planned as a next-generation GW observatory with two possible locations. The current plans propose CE-A in both 40km and 20km configurations, while CE-B is planned as a 20km detector. These future facilities are designed to complement the existing LIGO network, which includes observatories at Hanford (LHO) and Livingston (LLO), along with the planned Aundha (LAO) installation targeted for the early 2030s. All LIGO facilities are expected to be upgraded to A# sensitivity, comparable to Voyager specifications, forming a comprehensive global detection network.

The Einstein Telescope (ET) [19] is a revolutionary design concept as an underground triangular facility with 10km arm length. Various configurations and their scientific potential have been studied in [20]. The design incorporates three interferometers, and its strategic subterranean location is specifically chosen to significantly reduce seismic disturbances and Newtonian noise, which traditionally limit the performance of terrestrial facilities below 8 Hz. The targeted timeline calls for the first observations to commence by the mid-2030s, marking a significant milestone in GW astronomy.

In the transition period before the XG era, several significant detector developments are planned. The LIGO Voyager detector design [21] represents a crucial upgrade to the existing LIGO observatories, proposed for later this decade. Voyager's innovative design promises to achieve approximately double the sensitivity of Advanced LIGO Plus, marking a significant step forward in detection capabilities. Complementing these developments, the Neutron star Extreme Matter Observatory (NEMO) [22] has been proposed for construction in Australia. Designed as a specialized 4-km observatory, NEMO specifically targets neutron star GW astrophysics, with projected sensitivity levels matching those of ET and CE at frequencies above 2 kHz, particularly optimized for post-merger signals from binary neutron star (BNS) coalescences.

1.3.2 *Space based detection*

The frontier of GW astronomy extends beyond Earth's atmosphere with space-based detectors accessing frequency ranges unreachable from the ground. The Laser Interferometer Space Antenna (LISA) [23], scheduled for deployment in the mid-2030s, represents humanity's first dedicated space-based GW observatory. This ambitious mission will comprise three spacecraft forming an equilateral triangle with 2.5 million kilometer arms, trailing Earth's orbit around the Sun. Operating in the frequency range of 100 μHz to 100 mHz, LISA will investigate an entirely new population of sources. Its primary scientific objectives encompass tracking the evolution of black holes from cosmic dawn to the present era, observing mergers of intermediate-mass and lighter supermassive black holes (ranging from 10^2 to $10^7 m_\odot$), and scrutinizing extreme mass ratio inspirals that probe spacetime in the strongest gravitational fields known to physics. Additionally, LISA may serve as an early warning system for stellar-mass binary mergers, alerting ground-based observatories years in advance.

Several innovative approaches to space-based GW detection are being developed worldwide. China's TianQin project [24] proposes a constellation of three spacecraft orbiting Earth with 100,000 km arm lengths, designed to operate in the same frequency band as LISA but optimized for specific source types. The Taiji program [25], also led by Chinese scientists, plans a LISA-like detector with 3-million-kilometer arms in a heliocentric orbit. Japan's DECIGO (DECi-hertz Interferometer GW Observatory) [26, 27] aims to operate in the decihertz frequency range, bridging the gap between LISA and ground-based detectors. With 1000-kilometer arms and a unique frequency coverage, DECIGO would be particularly sensitive to intermediate-mass black hole mergers and stochastic GW backgrounds from the early universe. Taking an entirely different approach, the Lunar Gravitational Wave Antenna (LGWA) [28] proposes to utilize Earth's natural satellite as a detector. This innovative concept would deploy an array of cutting-edge seismometers on the lunar surface to monitor the Moon's normal modes within the 1 mHz to 1 Hz frequency range (decihertz band). The Moon offers unique advantages for GW detection due to its substantial mass, absence of atmospheric and oceanic interference, proximity to Earth, and minimal seismic activity. Historical data from Apollo missions confirms the Moon's exceptionally quiet seismic environment, with only minor disturbances from moonquakes and meteoroid impacts. The LGWA could operate concurrently with other space-based and next-generation ground-based observatories in the 2030s, with its capabilities improving as sensor technology advances.

In the nanohertz to microhertz frequency band, Pulsar Timing Arrays (PTAs) function as naturally occurring GW detectors. These arrays utilize precise timing measurements of millisecond pulsars, effectively creating an observatory spanning the Milky Way. PTAs are particularly sensitive to GWs generated by the cosmic population of supermassive black hole binaries in their early orbital evolution stages, offering insights into galaxy formation and evolution across cosmic time. The remarkable precision of pulsar timing enables the detection of minuscule variations in arrival times of radio pulses caused by

passing GWs, making PTAs a crucial complement to other detection methods.

1.4 Gravitational wave astronomy: Achievements and future prospects

The detection of GW by LIGO in 2015 marked the beginning of a new era in astronomy [29]. The first observation, GW150914, originated from the merger of two black holes ($\sim 36M_{\odot}$ and $\sim 29M_{\odot}$) approximately 1.3 billion light-years away, confirming Einstein's century-old prediction of GWs. This event provided the first direct evidence of BBH systems and their mergers, while also enabling unprecedented tests of general relativity in the strong-field regime [30].

In 2017, during the second observing run (O2), the landmark detection of GW170817 [31] marked the first observation of GWs from a BNS merger. This historic moment was made even more significant by accompanying EM observations spanning the entire spectrum, marking the beginning of multi-messenger astronomy. This event definitively established the connection between BNS mergers and short gamma-ray bursts (sGRBs), with the detection of GRB 170817A by Fermi-GBM just 1.7 seconds after the merger [32]. The measured time delay between the merger and the GRB onset provided constraints on the speed of gravity relative to the speed of light at the 10^{-15} level [33]. The subsequent discovery of the kilonova AT2017gfo provided the first direct evidence for r-process (rapid neutron capture) nucleosynthesis [34], demonstrating that BNS mergers are primary sites for the production of heavy elements beyond iron. The kilonova exhibited a rapid blue component from lighter r-process elements and a longer-lasting red component from lanthanides, confirming theoretical predictions [35]. The event also served as a standard siren, providing an independent measurement of the Hubble constant ($H_0 = 70.0_{-8.0}^{+12.0}$ km s $^{-1}$ Mpc $^{-1}$) [36].

The third observing run (O3) brought several significant discoveries. GW190412 was the first BBH system with definitively asymmetric masses (mass ratio ~ 0.28) and showed clear evidence for higher-order multipole moments in the gravitational radiation [37], providing new tests of general relativity. GW190521, the most massive BBH system detected to date, revealed a final black hole of $\sim 142M_{\odot}$, providing the first clear evidence for intermediate-mass black holes [38]. This system's primary component ($\sim 85M_{\odot}$) lies within the pair-instability supernova mass gap, challenging our understanding of stellar evolution and black hole formation mechanisms [39].

GW190814 represented another milestone, involving a $23M_{\odot}$ black hole merging with a $2.6M_{\odot}$ compact object - potentially either the heaviest neutron star or lightest black hole ever observed [40]. This system's high mass ratio ($q \sim 0.112$) and the secondary's mass falling within the hypothesized lower mass gap have profound implications for our understanding of compact object formation and evolutionary channels. The detection of GW190425, involving a significantly more massive BNS system (total mass $\sim 3.4M_{\odot}$) than those observed in our galaxy, has expanded our knowledge of binary evolution channels [41].

The first neutron star-black hole (NSBH) mergers, GW200105 and GW200115, were

detected during O3 [42], filling a crucial gap in our cosmic census of compact binary mergers. These systems, with mass ratios of ~ 0.22 and ~ 0.26 respectively, provide insights into the formation and evolution of mixed compact object binaries. While no EM counterparts were detected for these events, they established upper limits on the rates of NSBH mergers and their contribution to r-process element production.

Multiple BBH detections have revealed a diverse population of black holes with varying masses, spins, and orbital eccentricities [43]. Systems like GW190521 and GW190814 have challenged conventional formation scenarios, suggesting contributions from both isolated binary evolution and dynamical assembly in dense stellar environments [44]. The growing number of detections with mass ratios significantly different from unity suggests that asymmetric systems may be more common than previously thought [45].

The network of detectors, including LIGO, Virgo, and KAGRA, has demonstrated the power of multi-messenger astronomy. These observations have provided stringent constraints on the neutron star equation of state through tidal deformability measurements [46], particularly from GW170817 and GW190425. The combined analysis of multiple events has enabled population studies of compact objects, revealing features such as the presence of a mass gap between neutron stars and black holes, and potential peaks in the black hole mass distribution that might reflect fundamental aspects of stellar evolution [45].

Looking ahead, the field aims to detect new classes of sources including continuous waves from rotating neutron stars, stochastic backgrounds from the early universe, and signals from core-collapse supernovae. Particular emphasis is placed on understanding the diversity of kilonova emissions, which could reveal the distribution of heavy element production across cosmic time [47]. Future detectors like the Einstein Telescope [19] and Cosmic Explorer [18] promise improved sensitivity across a broader frequency range, potentially allowing us to probe the universe back to cosmic dawn. The enhanced sensitivity will enable detection of sub-solar mass black holes, if they exist, providing constraints on primordial black holes and DM candidates. Together with space-based observatories like LISA [23], GW astronomy will continue to unveil the secrets of the most extreme events in our cosmos, from the physics of matter under extreme conditions to the nature of gravity itself.

GW lensing represents a powerful new tool for exploring fundamental questions in cosmology and astrophysics [48]. The gravitational lensing of GWs from binary compact object mergers by massive galaxies or clusters will create multiple images with distinct magnifications and time delays, providing enhanced capabilities for source localization, constraining the Hubble constant, and understanding merger formation scenarios [49, 50]. GW lensing will offer unique opportunities to test general relativity and probe DM substructure in lens galaxies [51–54]. The absence of both microlensing and strong lensing signatures in LIGO-VIRGO-KAGRA’s first three observing runs has placed limits on the abundance of compact DM between $10^2 - 10^9 M_\odot$ [55, 56]. The future CE and ET detectors will usher in a new era of statistical studies, with their enhanced detection rates enabling precise measurements of cosmological parameters and constraining the nature of the DM through strongly lensed GWs [57, 58]. This convergence of next-generation

detectors and sophisticated analysis methods will establish lensed GWs as an essential probe of both cosmology and fundamental physics.

2 | Gravitational lensing

Gravitational lensing, one of the remarkable predictions of GR, occurs when gravitational fields bend the path of light and other forms of radiation. This phenomenon has become a powerful tool in modern astronomy and cosmology, enabling us to study distant galaxies, detect exoplanets, measure cosmic distances, and probe DM distributions [59, 60]. Now, with the dawn of GW astronomy, we stand at the beginning of a new frontier: the gravitational lensing of GWs. The principles governing the lensing of GWs are similar to those of EM waves, but with some important differences [61, 62]. This chapter provides a pedagogical overview of gravitational lensing, beginning with the propagation of GWs in curved spacetime and developing the mathematical framework needed to understand strong lensing phenomena. We first discuss the fundamental concepts of wave propagation and geometric optics in curved spacetime, followed by a detailed derivation of the lens equation. We then explore various properties of lens mapping, including magnification, time delays, and conditions for multiple imaging. The chapter concludes with a discussion of lensing degeneracies and commonly used lens models that are essential for practical applications. The presentation throughout this chapter follows the pedagogical approaches and theoretical frameworks established in [63] and [59].

2.1 *Propagation of gravitational waves in curved spacetime*

Having analyzed GWs as perturbations of flat spacetime through linearized Einstein field equations, we now extend our framework to understand GW propagation and its effects in curved spacetime. In this broader context, we consider GWs as perturbations over a curved dynamical background metric $g_{\mu\nu}(x)$:

$$g_{\mu\nu}(x) = \bar{g}_{\mu\nu}(x) + h_{\mu\nu}(x), \quad |h_{\mu\nu}| \ll 1. \quad (2.1)$$

The key challenge lies in distinguishing between background and perturbative components. This separation becomes natural when considering characteristic scales. In an appropriate coordinate system, the metric can be written as in Equation 2.1, where $\bar{g}_{\mu\nu}$ varies on a spatial length scale L_B , while superimposed perturbations have a characteristic length scale λ , satisfying:

$$\lambda \ll L_B, \quad (2.2)$$

where $\lambda = \frac{\lambda}{2\pi}$ is the reduced wavelength. This separation of scales enables us to decompose the Einstein equations into two distinct parts:

- Low-frequency modes (long wavelengths): Describe the dynamics of the background metric $\bar{g}_{\mu\nu}$ and define the energy-momentum tensor of the perturbations $h_{\mu\nu}$.
- High-frequency modes (short wavelengths): Govern the propagation of perturbations on the curved background spacetime

For the high-frequency modes, outside the source region and under the transverse-traceless Lorentz gauge conditions:

$$\nabla^\nu h_{\mu\nu} = 0 \text{ and } h^\mu{}_\mu = 0, \quad (2.3)$$

the propagation equation takes the form [3, 64]:

$$\nabla^\rho \nabla_\rho h_{\mu\nu} + 2\bar{R}_{\mu\rho\nu\sigma} h^{\rho\sigma} = 0. \quad (2.4)$$

Here, ∇ denotes covariant derivatives with respect to $\bar{g}_{\mu\nu}$, and $\bar{R}_{\mu\rho\nu\sigma}$ is the background Riemann tensor. Furthermore, the term $\bar{R}_{\mu\rho\nu\sigma} h^{\rho\sigma} = \mathcal{O}\left(\frac{h}{L_B^2}\right)$ while $\nabla^\rho \nabla_\rho h_{\mu\nu} = \mathcal{O}\left(\frac{h}{\lambda^2}\right)$, where $h \equiv \mathcal{O}(|h_{\mu\nu}|)$. Retaining terms to leading and next-to-leading order in $\frac{\lambda}{L_B}$, we obtain:

$$\nabla^\rho \nabla_\rho h_{\mu\nu} = 0. \quad (2.5)$$

Equations 2.3 and 2.5 together describe GW propagation in curved background spacetime.

2.2 Geometric optics in curved spacetime

The propagation equation for GWs (Equation 2.5) can be solved using the eikonal approximation in geometric optics. This approximation is valid when the reduced wavelength is much smaller than both the characteristic scales of variation of the background metric and of the amplitude/polarization:

$$\lambda \ll L_B \text{ and } \lambda \ll L_c, \quad (2.6)$$

where L_B and L_c represent these characteristic scales respectively. In particular, λ must be much smaller than the curvature radius of the wavefront. Under these conditions, we seek a solution with a rapidly varying phase θ (varying on scale λ) and a slowly varying amplitude (changing on scale $L = \min(L_B, L_c)$). We make the ansatz:

$$h_{\mu\nu}(x) = [A_{\mu\nu}(x) + \epsilon B_{\mu\nu}(x) + \dots] e^{\frac{i\theta(x)}{\epsilon}}, \quad (2.7)$$

where $\epsilon \equiv \mathcal{O}\left(\frac{\lambda}{L}\right)$ is a fictitious parameter (ultimately set to unity) used to track terms order by order in the expansion.

We define the wave vector $k_\mu = \partial_\mu \theta$ and write the amplitude tensor as $A_{\mu\nu} = A e_{\mu\nu}$, where $e_{\mu\nu}$ is the polarization tensor (normalized as $e^{\mu\nu} e_{\mu\nu}^* = 1$) and A is the scalar amplitude. Substituting the ansatz (Equation 2.7) into equations 2.3 and 2.5 yields the following properties of GW propagation in the geometric optics approximation [3]:

- Polarisation tensor $e_{\mu\nu}$ is orthogonal to the wave vector:

$$k^\nu e_{\mu\nu} = 0. \quad (2.8)$$

- Wave vector is null:

$$k^\rho k_\rho = 0. \quad (2.9)$$

- GW propagates along the null geodesics of background spacetime:

$$k^\mu \nabla_\mu k_\nu = 0. \quad (2.10)$$

- The number of graviton is conserved:

$$\nabla_\mu (A^2 k^\mu) = 0. \quad (2.11)$$

- polarisations are parallelly transported:

$$k^\rho \nabla_\rho e_{\mu\nu} = 0. \quad (2.12)$$

In the geometric optics limit, both gravitons and photons follow null geodesic paths through spacetime. This means GWs traverse curved spacetime in the same way as light. One notable consequence is gravitational lensing, where their path is bent by the curvature of spacetime around massive bodies just like photons.

2.3 Focusing of gravitational waves and breakdown of geometrical optics

Geometric optics approximations fail at caustics - points where multiple light rays from a source intersect. To understand what actually happens at these points, we need to consider wave optics effects like diffraction (or from a quantum perspective, the uncertainty principle).

Consider a circular ring of rays that is part of a plane wave passing near a star of mass M at an impact parameter b (see Figure 2.1). The gravitational field of the star deflects these rays. According to Einstein's classical result, the deflection angle, $\theta = \frac{2R_S}{b}$, where $R_S = \frac{2GM}{c^2}$ is the Schwarzschild radius of the star. This causes all rays in the ring to

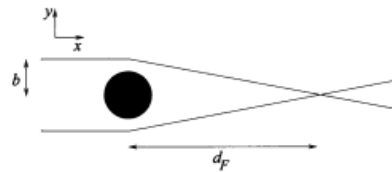


Figure 2.1: Focusing of GWs. This figure is taken from [3].

focus at a single point at a focal distance d_F , given by:

$$d_f \simeq \frac{b^2}{2R_S}. \quad (2.13)$$

In theory, focusing a one-dimensional surface (the ring) to a point would create infinite luminosity. However, diffraction prevents such perfect focusing in reality. We can use the uncertainty principle to determine when geometric optics breaks down. The error in y position is Δy and $\Delta y \leq b$. Then by the uncertainty principle, this creates an uncertainty in transverse momentum:

$$\Delta k_y \gtrsim \frac{\hbar}{b}. \quad (2.14)$$

This leads to angular spreading of:

$$\Delta \theta_y \simeq \frac{\Delta k_y}{k_x} \gtrsim \frac{\lambda}{b}. \quad (2.15)$$

At the focal distance d_F , this creates a transverse spread of:

$$\begin{aligned} \Delta y &\simeq d_F \Delta \theta_y \gtrsim \frac{\lambda b}{2R_S}, \\ \frac{\Delta y}{b} &\gtrsim \frac{\lambda}{2R_S}. \end{aligned} \quad (2.16)$$

For significant focusing to occur, Δy must be much smaller than b , which means:

$$\lambda \ll 2R_S. \quad (2.17)$$

This condition determines when geometric optics remains valid. For a lens with mass $\sim M_\odot$, according to 2.17, we require $\lambda \ll \mathcal{O}(6)$ km, which corresponds to frequencies $f \gg \mathcal{O}(10)$ kHz. While EM waves in the visible spectrum easily satisfy this condition, GW sources do not emit at frequencies $f \gg \mathcal{O}(10)$ kHz. As a result, significant amplification cannot be achieved with typical stellar-mass lenses. This represents a key distinction between gravitational lensing of EM waves and GWs.

2.4 Derivation of the lens equation

2.4.1 Approximate metrics of isolated, slowly moving, non-compact matter distributions

The metric produced by isolated slowly moving (non-relativistic) source is given by

$$ds^2 = - \left(1 + \frac{2\Phi}{c^2}\right) c^2 dt^2 + \frac{2A_i}{c} c dt dx^i + \left(1 - \frac{2\Phi}{c^2}\right) dl^2, \quad (2.18)$$

where $dl^2 = dx^2 + dy^2 + dz^2$ and

$$\begin{aligned}\Phi(t, \mathbf{x}) &\equiv -G \int \frac{\rho(t, \mathbf{y})}{|\mathbf{x} - \mathbf{y}|} d^3 \mathbf{y}; \\ A_i(t, \mathbf{x}) &\equiv -\frac{4G}{c^2} \int \frac{(\rho v_i)(t, \mathbf{y})}{|\mathbf{x} - \mathbf{y}|} d^3 \mathbf{y}.\end{aligned}\quad (2.19)$$

The perturbation Φ is the Newtonian potential generated by the mass distribution ρ , while A_i emerges as a vector potential due to mass currents in the system. Now define $A_i = \frac{4}{c^2} V_i$ where

$$V_i = -G \int \frac{(\rho v_i)(t, \mathbf{y})}{|\mathbf{x} - \mathbf{y}|} d^3 \mathbf{y}.\quad (2.20)$$

Then we can write the line element as

$$ds^2 = -\left(1 + \frac{2\Phi}{c^2}\right) c^2 dt^2 + \frac{\mathbf{V} \cdot d\mathbf{x}}{c^3} 8c dt + \left(1 - \frac{2\Phi}{c^2}\right) dl^2.\quad (2.21)$$

The post-Minkowskian metric satisfies the weak field approximation $|h_{\alpha\beta}| \ll 1$ precisely when the Newtonian potential Φ of the mass distribution ρ satisfies

$$\Phi \ll c^2,\quad (2.22)$$

which implies that

$$\left|\frac{\mathbf{V}}{c^3}\right| \leq \left|\frac{\mathbf{v}}{c}\right| \cdot \left|\frac{\Phi}{c^2}\right| \ll 1.\quad (2.23)$$

For spherically symmetric objects, condition 2.22 implies $R_S \ll R$. This excludes compact objects such as black holes and neutron stars from the domain of validity. Furthermore, condition 2.23 indicates that in the near zone, the metric is dominated by the Newtonian potential to lowest order.

2.4.2 Deflection of gravitational waves by quasistationary, isolated mass distributions

Considering that the configuration of local distribution of the matter remains approximately constant during the transit time of GW, and treating the metric in Equation 2.21 as time-independent, we obtain the effective refractive index of the gravitational field [65]:

$$n = 1 - \frac{2\Phi}{c^2} + \frac{4}{c^3} \mathbf{V} \cdot \mathbf{e},\quad (2.24)$$

where $\mathbf{e} \equiv \frac{d\mathbf{x}}{dl}$ is the unit tangent vector of a ray and $dl = |d\mathbf{x}|$ denotes the Euclidean arc length. From now due to the smallness of the effect (Equation 2.23) we will ignore the term $\frac{4}{c^3} \mathbf{V} \cdot \mathbf{e}$.

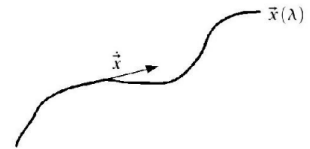


Figure 2.2: $dl = \left|\frac{d\mathbf{x}}{d\lambda}\right| d\lambda$, where λ is an arbitrary curve parameter. This figure is taken from [63].

Let $x(l)$ be a path of ray (see Figure 2.2), now from the variational principle

$$\begin{aligned} \delta \int n[\mathbf{x}(l)] dl &= 0, \\ \delta \int d\lambda n(\mathbf{x}(\lambda)) \left| \frac{d\mathbf{x}}{d\lambda} \right| &= 0. \end{aligned} \quad (2.25)$$

From Euler-Lagrange equation we obtain

$$\frac{d}{d\lambda} (n(\mathbf{x})\mathbf{e}) - (\nabla n) |\dot{\mathbf{x}}| = 0. \quad (2.26)$$

We can choose the curve parameter along the ray path, λ , such that $|\dot{\mathbf{x}}| = 1$, so now we have,

$$\frac{dn}{d\lambda} \mathbf{e} + n \frac{d\mathbf{e}}{d\lambda} = \nabla n, \quad (2.27)$$

$\frac{dn}{d\lambda}$ is the change along the ray, so $\frac{dn}{d\lambda} = (\nabla n \cdot \mathbf{e})$. So using this we have

$$\begin{aligned} \frac{d\mathbf{e}}{d\lambda} &= \frac{\nabla n - (\nabla n \cdot \mathbf{e}) \mathbf{e}}{n} \\ &= \frac{\nabla_{\perp} n}{n}. \end{aligned} \quad (2.28)$$

Finally we have

$$\dot{\mathbf{e}} = \nabla_{\perp} \ln n. \quad (2.29)$$

Let us define deflection angle

$$\hat{\alpha} \equiv \mathbf{e}_{\text{in}} - \mathbf{e}_{\text{out}}. \quad (2.30)$$

Now $n = 1 - \frac{2\Phi}{c^2}$ and $\frac{\Phi}{c^2} \ll 1$ implies $\ln n \approx -\frac{2\Phi}{c^2}$. So total deflection angle of the ray path,

$$\hat{\alpha} = \frac{2}{c^2} \int_{\lambda} \nabla_{\perp} \Phi d\lambda. \quad (2.31)$$

Suppose a ray starts into $+\mathbf{e}_z$ direction and passes by a point mass lens of mass M located at $z = 0$, with impact parameter b (Figure 2.3). The resulting deflection angle can be expressed as:

$$\hat{\alpha}(b) = \frac{2}{c^2} \int_{-\infty}^{+\infty} \nabla_{\perp} \Phi dz. \quad (2.32)$$

For a point mass $\Phi = -\frac{GM}{r}$, with $r = \sqrt{b^2 + z^2}$. Then for a point mass lens we will obtain [63]

$$|\hat{\alpha}| = \frac{4GM}{c^2 b}. \quad (2.33)$$

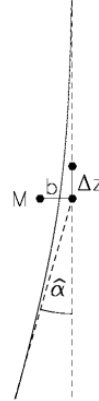


Figure 2.3: Deflection of ray by a point mass, M . This figure is taken from [63].

The deflection angle given in Equation 2.33 exhibits a linear relationship with mass M . Consider a planar distribution of N point masses, where each mass M_i is located at position ξ_i ($1 \leq i \leq N$). By applying the principle of superposition, for a ray passing through the plane at position ξ , the total deflection angle is:

$$\hat{\alpha}(\xi) = \sum_i \hat{\alpha}(\xi - \xi_i) = \frac{4G}{c^2} \sum_i M_i \frac{\xi - \xi_i}{|\xi - \xi_i|^2}. \quad (2.34)$$

In realistic scenarios, effective lenses for GW are predominantly galaxies and galaxy clusters. Since the lens size is substantially smaller than the involved distances (distances between source, lens and observer), the deflection occurs along a very short section of the light path. Thus, the lens can be approximated as a planar distribution of matter, the lens plane. This approximation is called the *thin screen approximation*. Similarly, the sources are assumed to lie on a plane, called the source plane. Under this approximation, the lensing matter distribution is fully described by its surface density,

$$\Sigma(\xi) = \int \rho(\xi, z) dz, \quad (2.35)$$

where ξ is a two dimensional vector on the lens plane and ρ is the three dimensional density.

As long as the thin screen approximation holds, the total deflection angle is obtained by summing the contribution of all the mass elements $\Sigma(\xi') d^2\xi'$:

$$\hat{\alpha}(\xi) = \frac{4G}{c^2} \int \frac{(\xi - \xi')\Sigma(\xi')}{|\xi - \xi'|^2} d^2\xi'. \quad (2.36)$$

This is the continuum limit of Equation 2.34.

2.4.3 Lens equation

Consider a gravitational lensing system illustrated in Figure 2.4. In this configuration, we have a source at redshift z_s located at an angular diameter distance D_s from the observer, and a lensing mass distribution at redshift z_ℓ with an angular diameter distance D_L .

The *angular diameter distance* relates transverse physical size of an object to its angular size (measured in radians). Such distances are essential for converting angular separations observed in telescope images into proper physical separations at the source position. The angular diameter distances are defined as:

$$D_L = \frac{1}{1 + z_\ell} D_M(0, z_\ell). \quad (2.37)$$

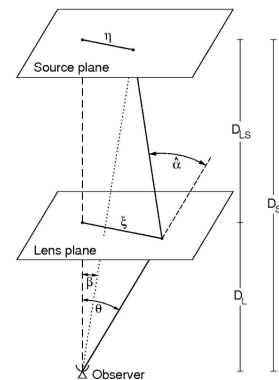


Figure 2.4: Sketch of gravitational lensing system. Figure from [63].

Here, D_M represents the transverse comoving distance. When two events occur at the same redshift or distance but are separated by an angle θ on the sky, their transverse comoving separation is given by $D_M\delta\theta$. In a flat universe, D_M is equivalent to the line-of-sight comoving distance (D_C)¹. Assuming a flat universe, we can express the transverse comoving distance as:

$$D_M(z_1, z_2) = D_C(z_1, z_2) = \frac{c}{H_0} \int_{z_1}^{z_2} \frac{dz'}{E(z')}, \quad (2.38)$$

where H_0 denotes the Hubble constant and $E(z) = \sqrt{\Omega_M(1+z)^3 + \Omega_\Lambda}$. Here, Ω_M represents the matter density parameter and Ω_Λ represents the dark energy density parameter.

The optical axis, depicted as a dashed line in Figure 2.4, passes through the observer and intersects the lens and source planes orthogonally, providing a reference for angular measurements in both planes. A source with angular position β lies in the source plane, displaced from the optical axis by a transverse distance $\eta = \beta D_S$. Rays from this source are deflected by an angle $\hat{\alpha}$ upon reaching the lens plane at impact parameter $\xi = \theta D_L$, causing the observer to perceive the source at an apparent angular position θ . In the small-angle approximation where θ , β , and $\hat{\alpha}$ are small, their geometric relationship is captured by the fundamental *lens equation*:

$$\theta D_S = \beta D_S + \hat{\alpha} D_{LS}. \quad (2.39)$$

Let us introduce a reduced deflection angle:

$$\alpha(\theta) = \frac{D_{LS}}{D_S} \hat{\alpha}(\theta). \quad (2.40)$$

Now using this definition in Equation 2.39, we arrive at the *lens equation*

$$\beta = \theta - \alpha(\theta). \quad (2.41)$$

Despite its deceptively simple form, this equation encapsulates the rich physics of gravitational lensing through the dependence of α on θ .

To express the lens equation (Equation 2.41) in dimensionless form, we introduce characteristic scales: ξ_0 in the lens plane and its corresponding scale $\eta_0 = \frac{\xi_0 D_S}{D_L}$ in the source plane. We then define dimensionless coordinates:

$$\mathbf{x} = \frac{\xi}{\xi_0}; \quad \mathbf{y} = \frac{\eta}{\eta_0}. \quad (2.42)$$

The deflection angle can be similarly scaled:

$$\alpha(\mathbf{x}) = \frac{D_L D_{LS}}{\xi_0 D_S} \hat{\alpha}(\xi_0 \mathbf{x}). \quad (2.43)$$

¹see [66] for the relationship between D_M and D_C in non-flat universes.

With these definitions, Equation 2.39 reduces to the dimensionless form:

$$\mathbf{y} = \mathbf{x} - \boldsymbol{\alpha}(\mathbf{x}). \quad (2.44)$$

2.5 Properties of lens mapping

2.5.1 Lensing potential

The *effective lensing potential*, $\hat{\Psi}$, characterizes extended mass distributions, derived by projecting the three-dimensional Newtonian potential, Φ , onto the lens plane with appropriate scaling:

$$\hat{\Psi}(\boldsymbol{\theta}) = \frac{D_{LS}}{D_L D_S} \frac{2}{c^2} \int \Phi(D_L \boldsymbol{\theta}, z) dz. \quad (2.45)$$

Its dimensionless form is given by:

$$\Psi = \frac{D_L^2}{\xi_0^2} \hat{\Psi}. \quad (2.46)$$

This potential yields two fundamental quantities: The scaled deflection angle, obtained from its gradient in the lens plane:

$$\nabla_x \Psi(\mathbf{x}) = \boldsymbol{\alpha}(\mathbf{x}). \quad (2.47)$$

And the convergence, given by its Laplacian:

$$\nabla_x^2 \Psi(\mathbf{x}) = 2\kappa(\mathbf{x}). \quad (2.48)$$

Here, convergence represents the dimensionless surface density:

$$\kappa(\mathbf{x}) = \frac{\Sigma(\mathbf{x})}{\Sigma_{\text{cr}}}. \quad (2.49)$$

where $\Sigma_{\text{cr}} = \frac{c^2}{4\pi G} \frac{D_S}{D_L D_{LS}}$ is the critical surface mass density—a characteristic quantity of the lens system determined by the angular diameter distances to the lens and source. The Equation 2.48 can be derived from the Poisson equation

$$\nabla^2 \Phi = 4\pi G \rho. \quad (2.50)$$

Note that, above ∇^2 is the three dimensional Laplacian. Now the surface mass density

$$\Sigma(\boldsymbol{\theta}) = \frac{1}{4\pi G} \int_{-\infty}^{+\infty} \nabla^2 \Phi dz, \quad (2.51)$$

and the dimensionless surface mass density using Equation 2.49

$$\kappa(\boldsymbol{\theta}) = \frac{1}{c^2} \frac{D_L D_{LS}}{D_S} \int_{-\infty}^{+\infty} \nabla^2 \Phi dz. \quad (2.52)$$

Introducing a two-dimensional Laplacian operator:

$$\nabla_{\theta}^2 = \frac{\partial^2}{\partial^2 \theta_1^2} + \frac{\partial^2}{\partial^2 \theta_2^2} = D_L^2 \left(\frac{\partial^2}{\partial^2 \xi_1^2} + \frac{\partial^2}{\partial^2 \xi_2^2} \right) = D_L^2 \left(\nabla^2 - \frac{\partial^2}{\partial z^2} \right). \quad (2.53)$$

This allows us to decompose the three-dimensional Laplacian:

$$\nabla^2 \Phi = \frac{1}{D_L^2} \nabla_{\theta}^2 \Phi + \frac{\partial^2 \Phi}{\partial z^2}. \quad (2.54)$$

Substituting this expression into Equation 2.52 yields:

$$\kappa(\boldsymbol{\theta}) = \frac{1}{c^2} \frac{D_L D_{LS}}{D_S} \left[\nabla_{\theta}^2 \int_{-\infty}^{+\infty} \Phi dz + D_L^2 \int_{-\infty}^{+\infty} \frac{\partial^2 \Phi}{\partial z^2} dz \right]. \quad (2.55)$$

For a gravitationally bound lens, $\frac{\partial \Phi}{\partial z}$ vanishes at the boundaries, eliminating the second term. Using Equation 2.45, we can write:

$$\kappa(\boldsymbol{\theta}) = \frac{1}{2} \nabla_{\theta}^2 \hat{\Psi} = \frac{1}{2} \frac{\xi_0^2}{D_L^2} \nabla_{\theta}^2 \Psi. \quad (2.56)$$

Given the relation:

$$\nabla_{\theta}^2 = D_L^2 \nabla_{\xi}^2 = \frac{D_L^2}{\xi_0^2} \nabla_x^2. \quad (2.57)$$

We can finally express the dimensionless surface mass density κ from Equation 2.56 as:

$$\kappa(\boldsymbol{x}) = \frac{1}{2} \nabla_x^2 \Psi(\boldsymbol{x}). \quad (2.58)$$

To obtain an expression for Ψ in terms of κ , we need to integrate Equation 2.48. Through this integration, we can express the effective lensing potential in terms of the convergence (κ) as:

$$\Psi(\boldsymbol{x}) = \frac{1}{\pi} \int_{\mathcal{R}^2} \kappa(\boldsymbol{x}') \ln |\boldsymbol{x} - \boldsymbol{x}'| d^2 \boldsymbol{x}'. \quad (2.59)$$

From this expression, we can write the scaled deflection angle:

$$\boldsymbol{\alpha}(\boldsymbol{x}) = \frac{1}{\pi} \int_{\mathcal{R}^2} \kappa(\boldsymbol{x}') \frac{\boldsymbol{x} - \boldsymbol{x}'}{|\boldsymbol{x} - \boldsymbol{x}'|} d^2 \boldsymbol{x}'. \quad (2.60)$$

2.5.2 Magnification and distortion

A fundamental characteristic of gravitational lensing is its ability to induce morphological distortions in extended sources. When a source of finite, non-negligible angular size undergoes gravitational lensing, differential deflection of light bundles results in systematic shape deformation. This phenomenon is particularly evident in EM gravitational lensing, where galaxies can manifest as elongated arclike structures.

The precise image morphology can be determined by applying the lens equation to

each point within the extended source distribution. For sources whose angular extent is substantially smaller than the characteristic scale over which the lens properties vary, the source-to-image mapping can be linearized. This linearized mapping is characterized by the Jacobian matrix.

$$\mathcal{A} \equiv \frac{\partial \mathbf{y}}{\partial \mathbf{x}} = \left(\delta_{ij} - \frac{\partial \alpha_i(\mathbf{x})}{\partial x_j} \right) = \left(\delta_{ij} - \frac{\partial^2 \Psi(\mathbf{x})}{\partial x_i \partial x_j} \right), \quad (2.61)$$

where x_i represents the i -component of \mathbf{x} on the lens plane ($i = 1, 2$). The Jacobian matrix can thus be expressed in terms of second-order derivatives of the lensing potential Ψ . For notational convenience, we introduce:

$$\frac{\partial^2 \Psi(\mathbf{x})}{\partial x_i \partial x_j} \equiv \Psi_{ij}. \quad (2.62)$$

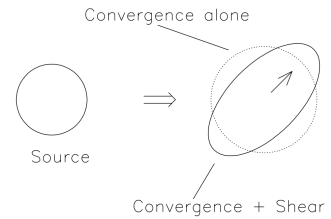
The Jacobian matrix can be decomposed by isolating its isotropic component:

$$\begin{aligned} \left(A - \frac{1}{2} \text{tr} \mathcal{A} \cdot I \right)_{ij} &= \delta_{ij} - \Psi_{ij} - \frac{1}{2} (1 - \Psi_{11} + 1 - \Psi_{22}) \delta_{ij} \\ &= -\Psi_{ij} + \frac{1}{2} (\Psi_{11} + \Psi_{22}) \delta_{ij} \\ &= \begin{bmatrix} -\frac{1}{2}(\Psi_{11} - \Psi_{22}) & -\Psi_{12} \\ -\Psi_{12} & \frac{1}{2}(\Psi_{11} - \Psi_{22}) \end{bmatrix}. \end{aligned} \quad (2.63)$$

The resulting trace-free, antisymmetric matrix is the shear matrix, which characterizes projection of the the gravitational tidal field. This matrix quantifies how the gradient of the gravitational force induces distortions in background sources.

On the lens plane, we can introduce a shear pseudo-vector $\gamma = (\gamma_1, \gamma_2)$ with components defined as:

$$\begin{aligned} \gamma_1(\mathbf{x}) &= \frac{1}{2} (\Psi_{11} - \Psi_{22}), \\ \gamma_2(\mathbf{x}) &= \Psi_{12} = \Psi_{21}. \end{aligned} \quad (2.64)$$



The shear matrix exhibits eigenvalues of $\pm\gamma = \pm\sqrt{\gamma_1^2 + \gamma_2^2}$. There exists a coordinate rotation by an angle ϕ , the shear matrix admits the representation:

$$\begin{bmatrix} \gamma_1 & \gamma_2 \\ \gamma_2 & -\gamma_1 \end{bmatrix} = \gamma \begin{bmatrix} \cos 2\phi & \sin 2\phi \\ \sin 2\phi & \cos 2\phi \end{bmatrix}. \quad (2.65)$$

The remaining component of the Jacobian can be expressed

Figure 2.5: Distortions effects due to gravitational lensing on a circular source. Figure from [60].

as:

$$\begin{aligned}
\frac{1}{2}\text{tr}\mathcal{A} &= \left[1 - \frac{1}{2}(\Psi_{11} + \Psi_{22})\right] \delta_{ij} \\
&= \left(1 - \frac{1}{2}\Delta\Psi\right) \delta_{ij} \\
&= (1 - \kappa)\delta_{ij}.
\end{aligned} \tag{2.66}$$

This leads to the complete form of the Jacobian matrix:

$$\begin{aligned}
\mathcal{A} &= \begin{bmatrix} 1 - \kappa - \gamma_1 & -\gamma_2 \\ -\gamma_2 & 1 - \kappa + \gamma_1 \end{bmatrix} \\
&= (1 - \kappa) \begin{bmatrix} 1 & 0 \\ 0 & 1 \end{bmatrix} - \gamma \begin{bmatrix} \cos 2\phi & \sin 2\phi \\ \sin 2\phi & \cos 2\phi \end{bmatrix}.
\end{aligned} \tag{2.67}$$

The physical significance of convergence and shear becomes evident through this decomposition. Convergence produces isotropic distortion, uniformly rescaling images across all directions. In contrast, shear induces anisotropic distortion by elongating the intrinsic shape of the source along a preferred direction. As illustrated in Figure 2.5, when both κ and γ are non-zero, a sufficiently small circular source, which is small enough compared to the scale of the lens is transformed into an ellipse. The resulting semi-major and semi-minor axes are given by:

$$a = \frac{r}{1 - \kappa - \gamma}, \quad b = \frac{r}{1 - \kappa + \gamma}, \tag{2.68}$$

where r represents the original source radius. Magnification emerges as a fundamental consequence of gravitational lensing distortion. The lens equation describes how a source's solid angle element $\delta\beta^2$ (alternatively expressed as the surface element δy^2) undergoes transformation into the observed solid angle $\delta\theta^2$ (corresponding to surface element δx^2). Gravitational lensing neither creates nor destroys photons or gravitons, and according to Liouville's theorem, the source's surface brightness remains constant. Consequently, when the solid angle under which we observe the source changes, this results in a corresponding magnification or demagnification of the source's observed flux.

The magnification can be quantitatively expressed through the determinant of the inverse of the Jacobian matrix (see Equation 2.61). The inverse transformation matrix, denoted as $\mathcal{M} = \mathcal{A}^{-1}$, is consequently termed the magnification tensor. This leads us to define

$$\mu \equiv \det\mathcal{M} = \frac{1}{\det\mathcal{A}} = \frac{1}{(1 - \kappa)^2 - \gamma^2}. \tag{2.69}$$

The eigenvalues of \mathcal{M} quantifies the amplification in the tangential and in the radial

direction and are given by

$$\begin{aligned}\mu_t &= \frac{1}{\lambda_t} = \frac{1}{1 - \kappa - \gamma}, \\ \mu_r &= \frac{1}{\lambda_r} = \frac{1}{1 - \kappa + \gamma}.\end{aligned}\tag{2.70}$$

When either λ_t or λ_r vanishes, the magnification becomes theoretically infinite. These conditions define two distinct curves in the lens plane: the *tangential* and *radial critical curves*. Images formed near the tangential critical curve exhibit strong distortion parallel to the curve itself, while those near the radial critical curve are elongated perpendicular to it.

2.5.3 Time delay function

The travel time for a lensed ray propagating from source to observer can be decomposed into two separate components:

$$t = t_{\text{geom}} + t_{\text{grav}}.\tag{2.71}$$

Here, t_{geom} represents the geometric time delay, which emerges from the difference in path length between the actual lensed trajectory and the unperturbed null geodesic. This term scales with the squared angular separation between the source position (β) and the image location (θ). The second component, t_{grav} , known as the gravitational or Shapiro delay, is characterized by the lensing potential (Ψ). This delay occurs because GWs or light experience reduced propagation speeds within the gravitational field of the lens compared to empty space, thereby increasing the travel duration along an equivalent path length.

Considering a lens at redshift z_ℓ , the total time delay (between the lensed and unperturbed geodesic) caused by gravitational lensing at the position \mathbf{x} on the lens plane is given by [65]

$$t(\mathbf{x}) = \frac{1 + z_\ell}{c} \frac{D_S \xi_0^2}{D_L D_{LS}} \left[\frac{1}{2} (\mathbf{x} - \mathbf{y})^2 - \Psi(\mathbf{x}) \right].\tag{2.72}$$

This is known as time delay function, $t(\mathbf{x})$. Now from equations 2.44 and 2.47, we can see that the lens equation can be written as

$$\begin{aligned}(\mathbf{x} - \mathbf{y}) - \nabla \Psi(\mathbf{x}) &= 0, \\ \nabla t(\mathbf{x}) &= 0.\end{aligned}\tag{2.73}$$

So the images are located at the stationary points of the time delay surface. The height difference between two stationary points on $t(\mathbf{x})$ gives the relative time delay between the corresponding images. Any variability in the source is observed first in the image corresponding to the lowest point on the surface, which means out of all images it arrives first, followed by the extrema located at successively larger values of t .

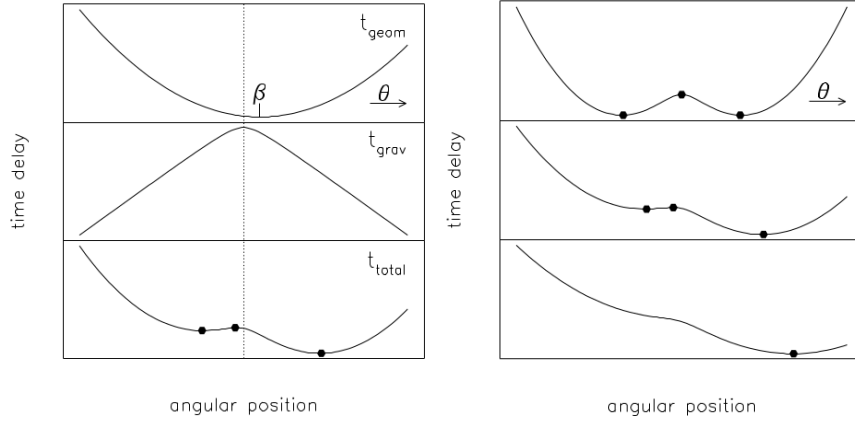


Figure 2.6: *Left:* Time delay components for an off-axis source in a circularly symmetric gravitational lens system, showing geometric delay, Shapiro delay, and their sum. The lens center is denoted by the dotted vertical line, while β indicates the source location. The resultant images form at the stationary points of the total time delay curve, marked by dots in the lower panel. *Right:* Time delay functions for varying source-lens configurations. (Top) Time delay function for the case of perfect source-lens alignment. (Middle) Time delay function when the source is moderately offset from the lens. (Bottom) Time delay function for a large angular separation between source and lens. Adapted from [60]

The hessian matrix of the time delay surface is

$$T = \frac{\partial^2 t(\mathbf{x})}{\partial x_i \partial x_j} \propto (\delta_{ij} - \Psi_{ij}) = \mathcal{A}. \quad (2.74)$$

The time delay surface exhibits three types of stationary points characterized by the eigenvalues of the Hessian matrix. Type I images form at minima, where positive eigenvalues ($\det \mathcal{A} > 0$, $\text{tr} \mathcal{A} > 0$) indicate upward curvature in both coordinate directions, resulting in positive magnification. Type II images occur at saddle points where opposite-signed eigenvalues create upward curvature in one direction and downward in another, resulting in negative magnification ($\det \mathcal{A} < 0$) and image parity inversion. Type III images emerge at maxima, characterized by negative eigenvalues ($\det \mathcal{A} > 0$, $\text{tr} \mathcal{A} < 0$) that produce downward curvature in both directions, yielding positive magnification. The three images shown in the left panel of Figure 2.6 represent, in left-to-right sequence, a saddle point, a maximum, and a minimum of the time delay surface.

The inverse magnification of lensed images is characterized by the curvature of the time delay function $t(\mathbf{x})$. Low curvature along a coordinate direction corresponds to high magnification, while steep curvature yields low magnification. For a circularly symmetric lens, the image multiplicity depends on the source-lens separation: a large offset produces a single image, while small separations generate three images. As the source position varies, image pairs can merge and disappear at critical lines in the lens plane, with corresponding caustic points in source plane. The curvature of

$t(\boldsymbol{x})$ approaches zero as $\delta\boldsymbol{x} \rightarrow 0$ near these merging points, resulting in maximum magnification just before image coalescence. Critical lines and caustics are fundamental properties of the lens mapping that identify regions of high magnification and separate domains of different image multiplicities.

A source positioned far from the gravitational lens produces a single image, which manifests as a minimum of the time delay surface. Additional extrema of the time delay surface emerge in pairs, as demonstrated in right panel of Figure 2.6. This paired creation of extrema leads to odd number image theorem [67], which states that non-singular lenses always produce an odd number of images.

2.5.4 Necessary and sufficient conditions for multiple imaging or strong lensing

The formation of multiple images by a gravitational lens depends critically on its dimensionless surface mass density κ . We can establish two key criteria that determine whether a given matter distribution will produce multiple images of background sources.

1. Multiple image formation in gravitational lensing occurs if and only if there exists a point where $\det\mathcal{A}(\boldsymbol{x})$ is negative. This criterion arises because a consistently positive $\det\mathcal{A}(\boldsymbol{x}) > 0$ means the lens mapping is one-to-one, precluding multiple images. Conversely, a negative $\det\mathcal{A}(\boldsymbol{x}_0)$ at any point \boldsymbol{x}_0 indicates a saddle point in the time delay surface, which by the odd-number theorem necessitates at least two more images at the extrema points.
2. A simple sufficient condition for multiple imaging is the existence of a point where $\kappa(\boldsymbol{x}) > 1$. When this occurs at a point \boldsymbol{x}_0 , the corresponding image cannot be a minimum of the time delay surface since minima require $\kappa < 1$, as evident from $\text{tr}\mathcal{A} = 2(1 - \kappa)$. Therefore, at least one additional image must exist at a minimum point, though this condition is not necessary for multiple imaging.

Lenses with $\kappa > 1$ are termed ‘strong’ lenses, though this condition isn’t strictly required for multiple image formation. The critical surface mass density Σ_{cr} serves as the fundamental scale that determines when strong lensing effects, such as arcs and image multiplication, emerge. The source’s redshift plays a crucial role: as it increases, Σ_{cr} decreases, effectively strengthening the lens for a fixed physical surface mass density Σ . This relationship manifests clearly in galaxy clusters, where strong lensing features appear at varying distances from the cluster’s center, depending on the source redshifts.

2.6 Lensing degeneracies

Most of the observables in lensing are dimensionless, leading to important degeneracies in the interpretation of observations. Here we will discuss very briefly about these

degeneracies through the time delay expression. This part is mostly adapted from [68]:

$$t(\mathbf{x}) = \frac{1+z_\ell}{c} \frac{D_S \xi_0^2}{D_L D_{LS}} \left[\frac{1}{2} (\mathbf{x} - \mathbf{y})^2 - \Psi(\mathbf{x}) \right]. \quad (2.75)$$

Now choosing a the length scale $\xi_0 = D_L$ we can write time delay in terms of angular positions:

$$t(\boldsymbol{\theta}) = \frac{1+z_\ell}{c} \frac{D_S D_L}{D_{LS}} \frac{1}{2} (\boldsymbol{\theta} - \boldsymbol{\beta})^2 - (1+z_\ell) \frac{8\pi G}{c^3} \nabla^{-2} \Sigma(\boldsymbol{\theta}). \quad (2.76)$$

Here, $\boldsymbol{\theta}$ and $\boldsymbol{\beta}$ represent angular positions in the image and source planes respectively, with ∇^{-2} being the inverse 2D Laplacian operator. Other symbols have usual meaning

2.6.1 Similarity transformations

Distance degeneracy This arises from uncertainty in distance measurements (uncertainty in one or more of D_S , D_L and cosmology). This is characterized by the transformation:

$$\frac{D_S D_L}{D_{LS}} \rightarrow s \frac{D_S D_L}{D_{LS}}, \quad \Sigma(\boldsymbol{\theta}) \rightarrow s \Sigma(\boldsymbol{\theta}). \quad (2.77)$$

This degeneracy only affects time delays by factor s (Equation 2.76), preserving image positions and magnifications.

Angular degeneracy This can be applied when images are unresolved. This is described by:

$$\boldsymbol{\theta} \rightarrow \sqrt{s} \boldsymbol{\theta}, \quad \boldsymbol{\beta} \rightarrow \sqrt{s} \boldsymbol{\beta}, \quad \Sigma \boldsymbol{\theta} \rightarrow s \Sigma(\boldsymbol{\theta}). \quad (2.78)$$

Here also magnification remains unchanged as the source and image positions are scaled by same factor, \sqrt{s} . It only scales the time delay by a factor s .

These two degeneracies operate independently, meaning that breaking one does not necessarily break the other. Through their combination, one can derive additional pairs of independent similarity transformations.

Consider the parallax effect induced by observer motion. When an observer moves transversely to the optical axis by r_{obs} , this generates apparent displacements of $-\frac{r_{\text{obs}}}{D_L}$ for the lens and $-\frac{r_{\text{obs}}}{D_S}$ for the source. This is same as keeping $\boldsymbol{\theta}$ fixed while shifting $\boldsymbol{\beta}$ by $r_{\text{obs}} \frac{D_{LS}}{D_L D_S}$. Applying these transformations to 2.76 and discarding $\boldsymbol{\theta}$ -independent terms we can write the modified equation for the arrival time:

$$t(\boldsymbol{\theta}) = (1+z_\ell) \left[\frac{D_S D_L}{c D_{LS}} \left(\frac{1}{2} \boldsymbol{\theta}^2 - \boldsymbol{\theta} \cdot \boldsymbol{\beta} \right) - \frac{1}{c} r_{\text{obs}} \cdot \boldsymbol{\theta} - \frac{8\pi G}{c^3} \nabla^{-2} \Sigma(\boldsymbol{\theta}) \right]. \quad (2.79)$$

Perspective Degeneracy When r_{obs} is known and non-zero., transformations 2.77 and 2.78 are not allowed individually but a combination of them is allowed.

$$\boldsymbol{\theta} \rightarrow s \boldsymbol{\theta}, \quad \boldsymbol{\beta} \rightarrow s \boldsymbol{\beta}, \quad \frac{D_S D_L}{D_{LS}} \rightarrow s^{-1} \frac{D_S D_L}{D_{LS}}, \quad \Sigma(\boldsymbol{\theta}) \rightarrow s \Sigma(\boldsymbol{\theta}). \quad (2.80)$$

This degeneracy maintains magnification invariance by equally rescaling θ and β (here magnification depends on r_{obs}). This degeneracy is known as *perspective* degeneracy because this preserves the product of distance and angular scales.

Parallax degeneracy

$$\theta \rightarrow s\theta, \quad \beta \rightarrow s\beta, \quad \frac{D_S D_L}{D_{LS}} \rightarrow s \frac{D_S D_L}{D_{LS}}, \quad \Sigma(\theta) \rightarrow s^3 \Sigma(\theta). \quad (2.81)$$

This degeneracy is broken by a parallax observation.

2.6.2 Mass-sheet degeneracy

The arrival time from Equation 2.76 can be expressed in a scaled form:

$$\tau(\theta) = \frac{1}{2}(\theta - \beta)^2 - 2\nabla_{\theta}^{-2}\kappa(\theta), \quad (2.82)$$

where $\kappa(\theta)$ and ∇_{θ}^{-2} are dimensionless quantities. This leads to:

$$t(\theta) = \frac{(1 + z_{\ell})}{c} \frac{D_L D_S}{D_{LS}} \tau(\theta), \quad \Sigma(\theta) = \frac{c^2}{4\pi G} \frac{D_S}{D_{LS} D_L} \kappa(\theta). \quad (2.83)$$

Under the transformation:

$$1 - \kappa \rightarrow s(1 - \kappa), \quad \beta \rightarrow s\beta, \quad (2.84)$$

time delays are rescaled while preserving image structure. But, since the source plane is rescaled by s , all magnifications are scaled by $\frac{1}{s^2}$, leaving relative magnifications unchanged. The effect on the lens is to rescale the lensing mass and then add or subtract a constant mass sheet. This degeneracy is known as the mass-sheet degeneracy, it is also known as magnification transformation [69]. This degeneracy can be broken through:

1. Time delay measurements combined with independent measurements of the Hubble constant, H_0 (assuming the redshifts are known).
2. Multiple lensed sources at different redshifts, as κ varies with source distance through the Σ_{cr} dependence, preventing factorization of the source redshift dependent term in Equation 2.76.

However, physical constraints restrict viable values of s , as the resulting mass distribution must remain non-negative, depending on κ .

2.6.3 Other degeneracies

Additional transformations exist that preserve $t(\theta)$ and its derivatives at image positions while modifying other regions, without affecting observables or introducing negative κ .

The *monopole* transformation exemplifies this: circularly symmetric mass redistributions inside or outside all observed images leave observables unchanged. Another example is the *prismatic* transformation, which adds an identical constant to the source position and bending angle, equivalent to introducing a massive lens at a large transverse distance while displacing the source oppositely. For more details of additional degeneracies, see [68, 69].

2.7 Simple lens models

A central objective in gravitational lensing theory is identifying lens-source configurations that generate observed image patterns. Analytic lens models serve as valuable tools in this endeavor, offering computational simplicity and easily derivable lensing properties. These models span various scales of astronomical objects: point-mass approximations effectively describe compact objects (planets, stars, black holes, and Massive Astrophysical Compact Halo Objects known as MACHOs), while extended mass distributions require more sophisticated approaches. Although axially symmetric models provide a fundamental starting point, elliptical models more accurately represent typical astrophysical systems, better capturing the complexity of observed lensing phenomena.

2.7.1 Point mass lens

When a light ray passes by a point mass lens of mass M with impact parameter b , the deflection angle is given by:

$$\hat{\alpha} = -\frac{4GM}{c^2 b} \mathbf{e}_r. \quad (2.85)$$

Here, \mathbf{e}_r represents the unit vector in the radial direction. In this axisymmetric system, we can align \mathbf{e}_r along a coordinate axis, reducing our analysis to one dimension. The scalar deflection angle becomes:

$$\hat{\alpha} = \frac{4GM}{c^2 b} = \frac{4GM}{c^2 D_L \theta}. \quad (2.86)$$

The gravitational lensing potential for a point mass lens takes the form:

$$\hat{\Psi} = \frac{4GM}{c^2} \frac{D_{LS}}{D_L D_S} \ln |\boldsymbol{\theta}|. \quad (2.87)$$

Now we can write the lens equation

$$\boldsymbol{\beta} = \boldsymbol{\theta} - \frac{4GM}{c^2 D_L \theta} \frac{D_{LS}}{D_S}. \quad (2.88)$$

Now defining the Einstein radius,

$$\theta_E \equiv \sqrt{\frac{4GM}{c^2} \frac{D_{LS}}{D_L D_S}} \quad (2.89)$$

the lens equation simplifies to

$$\beta = \theta - \frac{\theta_E^2}{\theta}. \quad (2.90)$$

Now we can use the dimensionless coordinates $x = \frac{\theta}{\theta_E}$ and $y = \frac{\beta}{\theta_E}$ on the lens and source plane respectively. With a length scale $\xi_0 = \theta_E$ we can write the lens Equation 2.44 as

$$y = x - \frac{1}{x}. \quad (2.91)$$

This equation admits two solutions:

$$x_{\pm} = \frac{1}{2} \left[y \pm \sqrt{y^2 - 4} \right], \quad (2.92)$$

representing the positions of the two images formed by the point mass lens.

For a source that is perfectly aligned with the lens (i.e., $y = 0$), we find that $x_{\pm} = \pm 1$. This special configuration results in the formation of an Einstein ring - a circular image with angular radius θ_E . The Einstein radius can be estimated in terms of typical astronomical scales:

$$\begin{aligned} \theta_E &\approx (10^{-3})'' \left(\frac{M}{M_{\odot}} \right)^{\frac{1}{2}} \left(\frac{D}{\text{Gpc}} \right)^{-\frac{1}{2}}, \\ &\approx 1'' \left(\frac{M}{10^{12} M_{\odot}} \right)^{\frac{1}{2}} \left(\frac{D}{\text{Gpc}} \right)^{-\frac{1}{2}}. \end{aligned} \quad (2.93)$$

In these expressions, D represents the effective lensing distance, defined as $D \equiv \frac{D_L D_S}{D_{LS}}$, which combines the various distance measures in the lensing system.

For very large angular separations between the source and lens (as $\beta \rightarrow \infty$), the two image positions show distinct behaviors: $\theta_+ \rightarrow \beta$ indicates that one image appears at approximately the true source position, while $\theta_- \rightarrow 0$ shows that a second image forms at the lens center. For such large source-lens separations, the lensing effect becomes negligible for the primary image, though mathematically a second image still exists at $\theta_- = 0$.

For an axially-symmetric lens, the magnification can be derived from the determinant of the Jacobian matrix:

$$\begin{aligned} \det \mathcal{A} &= \frac{y}{x} \frac{\partial y}{\partial x} = \left(1 - \frac{\alpha}{x} \right) \left(1 - \frac{\partial \alpha}{\partial x} \right) \\ &= \left(1 - \frac{1}{x^2} \right) \left(1 + \frac{1}{x^2} \right) \\ &= 1 - \left(\frac{1}{x} \right)^4. \end{aligned} \quad (2.94)$$

The magnification is therefore:

$$\mu = \left[1 - \left(\frac{1}{x} \right)^4 \right]^{-1}. \quad (2.95)$$

Expressing the magnification in terms of the source position for both images:

$$\begin{aligned} \mu_{\pm} &= \left[1 - \left(\frac{1}{x_{\pm}} \right)^4 \right]^{-1} \\ &= \frac{x_{\pm}^4}{x_{\pm}^4 - 1} \\ &= \frac{1}{2} \pm \frac{y^2 + 2}{2y\sqrt{y^2 + 4}}. \end{aligned} \quad (2.96)$$

In the limit where $y \rightarrow \infty$, we find that $\mu_- \rightarrow 0$ while $\mu_+ \rightarrow 1$. This indicates that although the lens equation always yields two solutions, at large angular separations between the source and lens, the image near the lens center becomes undetectable as it is highly demagnified. The other image becomes indistinguishable from the unlensed source, having both its position and flux same as source. For such large source-lens separations, the lensing effect becomes negligible.

In the context of lensing of GW, only very massive objects with $M > 10^8 M_{\odot}$ can effectively act as strong lenses. These primarily consist of galaxies, clusters, SMBHs, and MACHOs. For compact lenses such as SMBHs and MACHOs, the point mass lens model provides an accurate approximation. However, when considering less compact massive objects like galaxies and galaxy clusters, the point mass approximation fails, necessitating extended mass distribution models to accurately characterize the lensing phenomena.

2.7.2 Axially symmetric lenses

We consider a class of matter distributions characterized by a circularly-symmetric surface mass density, $\Sigma(\xi) = \Sigma(|\xi|)$. This symmetry allows the lens equation to be reduced to a one-dimensional form. For axially symmetric lenses, the deflection angle is given by [65]

$$\hat{\alpha}(\xi) = \frac{4GM(\xi)}{c^2\xi}. \quad (2.97)$$

This expression reveals an important property: mass within a disc of radius ξ around the mass center affects the deflection at point ξ as if concentrated at the center, while mass outside this radius has no contribution. This behavior mirrors the gravitational effects of spherically symmetric mass distributions in three dimensions.

Now we can write the scaled deflection angle

$$\begin{aligned}\alpha(x) &= \frac{D_L D_{LS}}{\xi_0 D_S} \hat{a}(\xi_0 x) \\ &= \frac{M(\xi_0 x)}{\pi \xi_0^2 \Sigma_{\text{cr}}} \frac{1}{x} \\ &\equiv \frac{m(x)}{x},\end{aligned}\tag{2.98}$$

where $m(x)$ represents the dimensionless mass contained within radius x . Using Equation 2.60, we can express the scaled deflection angle $\alpha(x)$ as

$$\alpha(x) = \frac{2}{x} \int_0^x x' \kappa(x') dx'.\tag{2.99}$$

The dimensionless mass $m(x)$ can then be written in terms of the dimensionless surface mass density, κ , as

$$m(x) = 2 \int_0^x x' \kappa(x') dx'.\tag{2.100}$$

Then lens equation 2.44 now becomes

$$y = x - \frac{m(x)}{x}.\tag{2.101}$$

Lets write the deflection angle at a point $\mathbf{x} = (x_1, x_2)$ as a vector

$$\boldsymbol{\alpha}(\mathbf{x}) = \frac{m(x)}{x^2} \mathbf{x},\tag{2.102}$$

where $x = |\mathbf{x}|$. We can obtain the Jacobian matrix for the lens mapping by differentiation of lens equation, which leads to

$$\mathcal{A} = \mathcal{I} - \frac{m(x)}{x^4} \begin{pmatrix} x_2^2 - x_1^2 & -2x_1 x_2 \\ -2x_1 x_2 & x_1^2 - x_2^2 \end{pmatrix} - \frac{dm(x)}{dx} \frac{1}{x^3} \begin{pmatrix} x_1^2 & x_1 x_2 \\ x_1 x_2 & x_2^2 \end{pmatrix},\tag{2.103}$$

where \mathcal{I} is the two dimensional identity matrix. From which we obtain the convergence and shear components:

$$\kappa(x) = \frac{1}{2x} \frac{dm(x)}{dx},\tag{2.104}$$

$$\gamma_1(x) = \frac{1}{2} (x_2^2 - x_1^2) \left(\frac{2m(x)}{x^4} - \frac{dm(x)}{dx} \frac{1}{x^3} \right),\tag{2.105}$$

$$\gamma_2(x) = x_1 x_2 \left(\frac{dm(x)}{dx} \frac{1}{x^3} - \frac{2m(x)}{x^4} \right),\tag{2.106}$$

and $\gamma = \sqrt{\gamma_1^2 + \gamma_2^2}$ is

$$\gamma(x) = \frac{m(x)}{x^2} - \kappa(x). \quad (2.107)$$

Now from Equation 2.100,

$$\frac{m(x)}{x^2} = 2\pi \frac{\int_0^x x' \kappa(x') dx'}{\pi x^2} = \bar{\kappa}(x), \quad (2.108)$$

where $\bar{\kappa}$ is the mean surface mass density within radius x . Then from Equation 2.107 we can write

$$\gamma(x) = \bar{\kappa}(x) - \kappa(x). \quad (2.109)$$

Now the determinant of the Jacobian matrix \mathcal{A} is

$$\begin{aligned} \det \mathcal{A} &= \frac{y}{x} \frac{dy}{dx} = \left(1 - \frac{m(x)}{x^2}\right) \left[1 - \frac{d}{dx} \left(\frac{m(x)}{x}\right)\right] \\ &= \frac{y}{x} \frac{dy}{dx} = \left(1 - \frac{m(x)}{x^2}\right) \left(1 + \frac{m(x)}{x^2} - 2\kappa(x)\right) \\ &= \left(1 - \frac{\alpha(x)}{x}\right) \left(1 - \frac{d\alpha(x)}{dx}\right). \end{aligned} \quad (2.110)$$

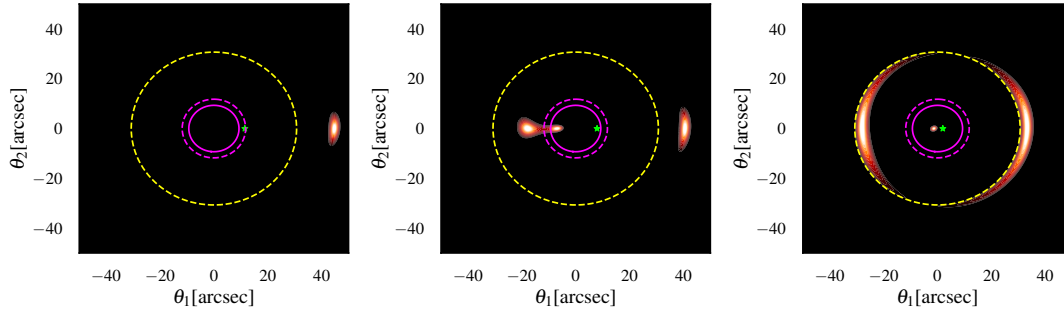


Figure 2.7: Critical curves and caustics of a core SIS lens ($M \sim 10^{15} M_{\odot}$) at $z_{\ell} = 0.5$, with source at $z_s = 2$. Dashed and solid curves represent critical curves and caustics respectively, with yellow indicating tangential and magenta indicating radial features. Green star denotes the source position. Panels show image configurations for different source positions: (*Upper*) Single image for source outside radial caustic; (*Middle*) Three images formed when source crosses radial caustic, with two new radially stretched images on opposite sides of the radial critical curve; (*Lower*) when source approaches center, two images with strong tangential stretching near tangential critical curve and one highly demagnified near the center. Central point caustic is not shown. Plots are made using [lenstronomy](#) package [70, 71]

For axially symmetric lenses with monotonically increasing $m(x)$, critical lines occur where $\det \mathcal{A} = 0$. According to Equation 2.110, this produces two specific critical lines defined by:

1. The tangential critical line condition: $\frac{m(x)}{x^2} = 1$.
2. The radial critical line condition: $\frac{d}{dx} \left(\frac{m(x)}{x} \right) = \frac{dy}{dx} = 1$.

Both conditions defines circles on the lens plane. Which are tangential and radial critical curves, which are shown in dashed yellow and magenta circles in Figure 2.7. .

For the *tangential critical line* [where $\frac{m(x)}{x^2} = 1$]:

- Any vector tangential to this line becomes an eigenvector with zero eigenvalue of the Jacobian matrix \mathcal{A} .
- From the lens mapping we can see that all points along this critical line map to a single point ($y = 0$) on the source plane.
- This results in point tangential caustics in axially symmetric models.

For the radial critical line [where $\frac{d}{dx} \left(\frac{m(x)}{x} \right) = 1$]:

- Any vector perpendicular to this line becomes an eigenvector with zero eigenvalue.
- Points along this critical line map to a circular caustic on the source plane (solid magenta line in Figure 2.7).

Strong lensing and image properties: Strong lensing of a source produce multiple images. The position of the source relative to the caustics determines how many images will appear. When a source is positioned inside the radial caustic (solid magenta in Figure 2.7), it generates three distinct images. Conversely, only a single image forms when the source lies outside the radial caustic, as illustrated in Figure 2.7. The tangential critical curve has no effect on image multiplicity since it creates a point caustic at $y = 0$ rather than a caustic curve. Consequently, the creation or destruction of image pairs is solely dependent on the existence of a radial critical curve.

A fundamental property of gravitational lensing is that images always appear in odd numbers, with one important exception. This exception occurs in singular lenses-those with infinite central density-where only two images form when the source lies within the radial caustic. The presence of a singularity suppresses the central maximum of the time delay surface, effectively eliminating one potential image that would typically exist in non-singular lenses.

Images experience different stretching in two directions: a tangential stretching by $\left[1 - \frac{m(x)}{x^2}\right]^{-1}$ and a radial stretching by $\left[1 + \frac{m(x)}{x^2} - 2\kappa(x)\right]^{-1}$. These distortion effects become particularly pronounced for extended sources, as illustrated in Figure 2.7. The figure demonstrates two distinct cases for multiple images:

1. When a source lies near the central point-like caustic (right panel of Figure 2.7), it produces:

- Two highly elongated tangential arcs near the outer critical curve
 - One faint central image
2. When a source is positioned on the outer caustic (middle panel of Figure 2.7), it creates:
- A radially stretched image formed by two merging images
 - A third image with tangential orientation beyond the outer critical line

2.7.3 Singular isothermal sphere

The Singular Isothermal Sphere (SIS) represents a fundamental axially symmetric lens model. Its derivation assumes matter behaves as an ideal gas in both thermal and hydrostatic equilibrium, confined by a spherical gravitational potential. Under these conditions, the three-dimensional density profile takes the form:

$$\rho(r) = \frac{\sigma_v^2}{2\pi G r^2}, \quad (2.111)$$

where σ_v denotes the velocity dispersion of the particles and r is the radial distance from the center. The corresponding two-dimensional surface density, obtained by projecting on the lens plane:

$$\Sigma(\xi) = \frac{\sigma_v^2}{2G\xi}. \quad (2.112)$$

Despite exhibiting a central singularity at $\xi = 0$ where density becomes infinite, the SIS profile serves as an effective model for galactic mass distributions. Its significance lies primarily in its ability to reproduce the flat rotation curves of spiral galaxies.

Now choosing the length scale

$$\xi_0 = 4\pi \left(\frac{\sigma_v}{c}\right)^2 \frac{D_L D_{LS}}{D_S}, \quad (2.113)$$

we obtain

$$\kappa(x) = \frac{1}{2x} ; \quad \Psi(x) = |x| ; \quad \alpha(x) = \frac{x}{|x|}, \quad (2.114)$$

and the lens equation becomes

$$y = x - \frac{x}{|x|}. \quad (2.115)$$

When $0 < y < 1$, two images form: one at $x = y + 1$ and another at $x = y - 1$, positioned on opposite sides of the lens center. When $y > 1$, only a single image forms at $x = y + 1$. Images that form at $x > 0$ are classified as Type I (minima), while those at $x < 0$ are Type II (saddle). The circle defined by $|x| = 1$ represents the tangential critical curve. The shear can be calculated as $\gamma(x) = \frac{1}{2x}$. If the central singularity were removed, an additional third image would appear in the core region (as shown in Figure 2.7). The studies presented in Chapters 4 and 5 primarily use this lens model.

The magnification of an image at x is given by:

$$\mu = \frac{|x|}{|x| - 1}. \quad (2.116)$$

The radial eigenvalue of the Jacobian matrix is unity throughout the domain, meaning magnification occurs only in the tangential direction.

For $y < 1$, two images are produced with magnifications given by:

$$\mu_+ = \frac{y+1}{y} = 1 + \frac{1}{y}; \quad \mu_- = 1 - \frac{1}{y}. \quad (2.117)$$

As $y \rightarrow 1$, the magnification μ_- of the second image progressively decreases until the image vanishes at $y = 1$. In the limit where $y \rightarrow \infty$, the total magnification approaches unity, demonstrating that sources far from the lens experience minimal gravitational lensing effects (as depicted in the Figure 2.8).

The time delay between the two images is given by

$$\Delta t = \frac{(1+z_\ell)}{c} \left[4\pi \left(\frac{\sigma_v}{c} \right)^2 \right]^2 \frac{D_L D_{LS}}{D_S} 2y. \quad (2.118)$$

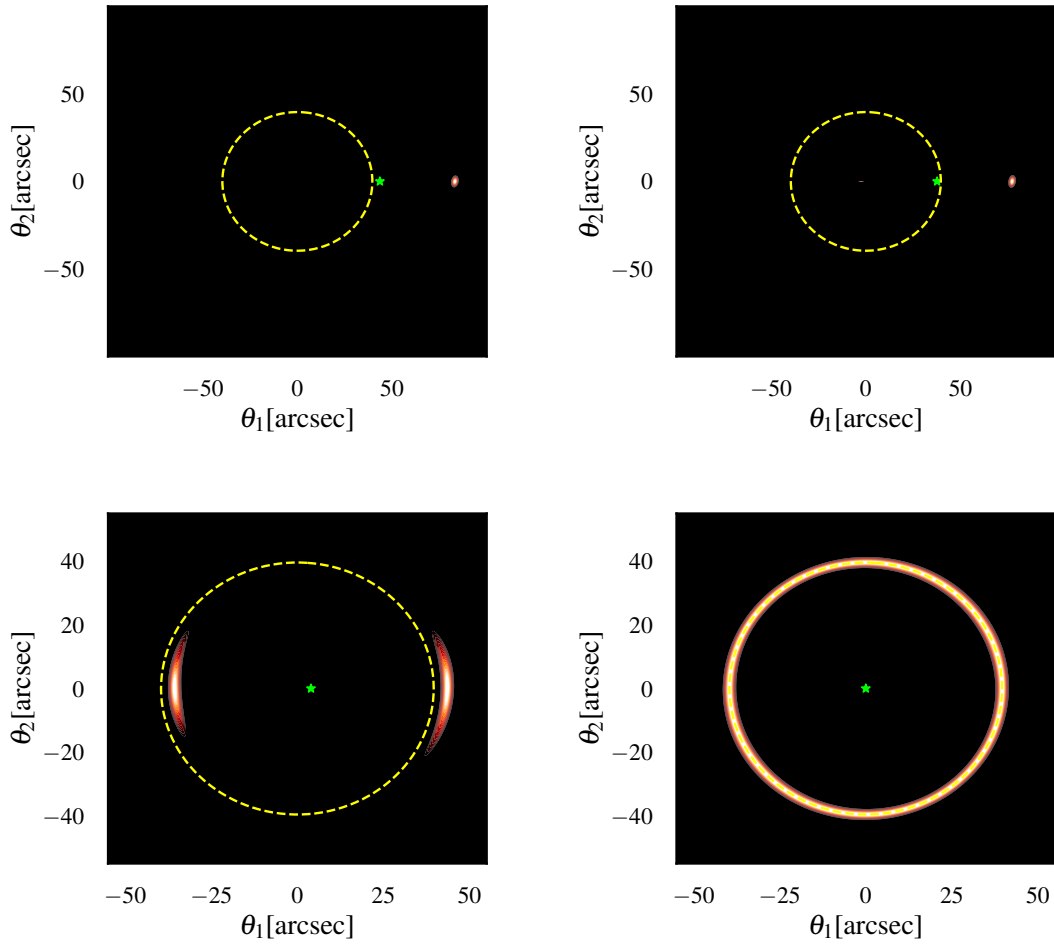


Figure 2.8: An SIS lens of mass $\sim 10^{15} M_{\odot}$ at $z = 0.5$ lensing a source at $z_s = 2$. Panels show image evolution as source position varies. Green star indicates the source position. (Upper left) Single image for source outside the Einstein radius; (Upper right and Lower left) Source crosses the Einstein radius, a new image with very low magnification is born near the center and then both images move towards the Einstein radius while getting stretched tangentially. (Lower right) Einstein ring forms when source aligns with lens center. Created using [lenstronomy](#) [70, 71].

3 | Cosmology and Structure Formation

3.1 Cosmological Framework

This chapter aims to present a concise pedagogical introduction to the concepts and tools in modern cosmology that will be used in Chapters 4 and 5. Modern cosmology rests upon the foundation of an expanding universe that emerged from a dense, hot initial state. As the universe expanded and cooled, matter began to form increasingly complex structures, eventually leading to the formation of galaxies like our own.

The mathematical framework describing this evolution is governed by Einstein's field equations:

$$G_{\mu\nu} = 8\pi G T_{\mu\nu} + g_{\mu\nu}\Lambda, \quad G_{\mu\nu} = R_{\mu\nu} - \frac{1}{2}g_{\mu\nu}R. \quad (3.1)$$

Here, the geometric properties of spacetime, encoded in the metric tensor $g_{\mu\nu}$, Ricci tensor $R_{\mu\nu}$, and Ricci scalar R , are directly linked to the matter-energy content represented by the stress-energy tensor $T_{\mu\nu}$ and cosmological constant Λ .

The early universe exhibits remarkable uniformity on large scales, displaying both homogeneity and isotropy. These symmetries lead to the Friedmann-Lemaître-Robertson-Walker metric:

$$ds^2 = -dt^2 + a(t) \left[\frac{dr^2}{1 - kr^2} + r^2(d\theta^2 + \sin^2\theta d\phi^2) \right]. \quad (3.2)$$

In this expression, $a(t)$ represents the cosmic scale factor describing the universe's expansion, while k characterizes spatial curvature. Above, r, θ, ϕ are the usual spherical polar coordinates. The temporal evolution of $a(t)$ emerges from the application of this metric to Einstein's field equations, yielding the fundamental Friedmann equations that describe cosmic expansion.

$$\left(\frac{\dot{a}}{a}\right)^2 + \frac{k}{a^2} = \frac{8\pi G}{3}\rho + \frac{\Lambda}{3}, \quad (3.3)$$

$$\frac{\ddot{a}}{a} + \left(\frac{\dot{a}}{a}\right)^2 + \frac{k}{a^2} = -8\pi G\rho + \Lambda. \quad (3.4)$$

These equations emerge from considering a stress-energy tensor with the specific form (perfect fluid):

$$T_{\mu\nu} = (\rho + p)u_\mu u_\nu + p g_{\mu\nu}. \quad (3.5)$$

The equations involve several key parameters: the scale factor $a(t)$ along with its time derivatives \dot{a} and \ddot{a} , the spatial curvature parameter k , energy density ρ , pressure p , the four-velocity vector u_μ , the cosmological constant Λ , and Newton's gravitational constant G . The relationship between matter density and pressure follows a simple equation of state $p = w\rho$, where w is the equation of state parameter. Contemporary observational evidence strongly supports a spatially flat universe [72], corresponding to $k = 0$. This simplification of vanishing spatial curvature will be adopted in subsequent analyses.

The Friedmann equations lead to a fundamental relation describing energy conservation in the expanding universe:

$$\dot{\rho} = -3\frac{\dot{a}}{a}(\rho + p). \quad (3.6)$$

For a constant equation-of-state parameter w , where $p = w\rho$, the solution takes the form:

$$\rho = \rho_0 a^{-3(1+w)}. \quad (3.7)$$

This equation governs the behavior of different components in the universe: For radiation and highly relativistic matter, $w = 1/3$, leading to:

$$\rho_r \propto a^{-4}. \quad (3.8)$$

Non-relativistic matter has negligible pressure ($w = 0$), resulting in:

$$\rho_{\text{nr}} \propto a^{-3}. \quad (3.9)$$

For dark energy $w = -1$ leads to:

$$\rho_\Lambda = \text{const.} \quad (3.10)$$

3.1.1 The Hubble parameter and cosmic density parameters

The Hubble parameter, which characterizes the expansion rate of the universe, is defined as:

$$H(t) = \frac{\dot{a}}{a}. \quad (3.11)$$

Combining the Friedmann equations with the evolution of matter and radiation densities, we can express the Hubble parameter in terms of the scale factor and various density parameters:

$$\left(\frac{H(t)}{H_0}\right)^2 = \Omega_R a^{-4} + \Omega_M a^{-3} + \Omega_K a^{-2} + \Omega_\Lambda \quad (3.12)$$

Here, we define the dimensionless density parameters:

$$\Omega_M = \frac{\rho_M}{\rho_{\text{cr}}} \quad (\text{matter density parameter}), \quad (3.13)$$

$$\Omega_R = \frac{\rho_R}{\rho_{\text{cr}}} \quad (\text{radiation density parameter}), \quad (3.14)$$

$$\Omega_\Lambda = \frac{\Lambda}{3H_0^2} \quad (\text{dark energy density parameter}), \quad (3.15)$$

$$\Omega_K = -\frac{k}{H_0^2} \quad (\text{curvature density parameter}). \quad (3.16)$$

The critical density of the universe, which serves as a reference scale, is given by:

$$\rho_{\text{cr}} = \frac{3H_0^2}{8\pi G}, \quad (3.17)$$

where H_0 is the Hubble constant, representing the current value of the Hubble parameter.

3.1.2 Cosmic history and evolution

The universe undergoes three main epochs:

1. Radiation Domination:

$$a(t) \propto t^{1/2}. \quad (3.18)$$

2. Matter Domination:

$$a(t) \propto t^{2/3}. \quad (3.19)$$

3. Dark Energy Domination:

$$a(t) \propto \exp\left(\sqrt{\frac{\Lambda}{3}}t\right). \quad (3.20)$$

The expansion of the universe decelerates during both radiation and matter domination. However, as the matter density approaches zero and dark energy (characterized by the cosmological constant Λ) becomes dominant, the universe transitions into an accelerating phase. This transition from matter to dark energy domination marks a fundamental change in the universe's expansion history.

The radiation-dominated early universe began as a hot, dense particle soup in thermal equilibrium. As space expanded and cooled, several key phase transitions occurred sequentially: quarks confined into baryons, electrons and positrons annihilated, neutrinos decoupled, first atomic nuclei formed through nucleosynthesis, and finally recombination occurred as electrons combined with nuclei to form neutral atoms. This last transition allowed photons to travel freely, creating the cosmic microwave background (CMB) - our farthest observable window into the universe's history. The universe then entered matter domination around recombination, beginning the "dark ages." During this period, primordial density fluctuations grew linearly before undergoing nonlinear collapse to form the cosmic web and first virialized objects. The formation of the first stars ended the dark ages and began the reionization of intergalactic hydrogen. Structure formation proceeded hierarchically, with small DM halos merging into larger structures. Baryonic matter, through EM interactions and radiative cooling, concentrated at the bottom of gravitational potentials. This process enabled significant star formation, leading to galaxies of various sizes that traced the underlying DM density field. Currently, the universe has entered the dark energy era, dominated by the cosmological constant's contribution and characterized by accelerated expansion. The future holds the progressive isolation of gravitationally unbound systems, ultimately leading to isolated "island universes" separated by empty space [73].

3.2 Structure formation in linear regime

The early universe exhibits an almost uniform matter distribution with small density perturbations. These perturbations originate from quantum fluctuations that were amplified to macroscopic scales during the inflationary period. The density perturbations, or overdensities, are parametrized by the dimensionless quantity:

$$\delta(x, t) = \frac{\rho(x, t) - \rho_b(t)}{\rho_b(t)}, \quad (3.21)$$

where $\rho(x, t)$ represents the density at comoving coordinate x and $\rho_b(t)$ denotes the background density.

For small perturbations where $\delta \ll 1$, the evolution can be treated analytically using perturbation theory. The analysis focuses on the linear order evolution of δ within the Newtonian approximation when the perturbation wavelength is significantly smaller than the horizon scale $d_H(t) = H^{-1}(t)$. This approach provides a framework for understanding the initial stages of structure formation in the universe.

3.2.1 Particle motion in expanding universe

We begin by considering the motion of a non-relativistic particle of mass m under a smooth gravitational potential in an expanding universe¹. The proper position and velocity in physical space are given by:

$$\mathbf{r} = a\mathbf{x}, \quad (3.22)$$

$$\mathbf{u} = a\dot{\mathbf{x}} + \dot{a}\mathbf{x} = \mathbf{v}_p + \mathbf{v}_h, \quad (3.23)$$

where a is the scale factor, \mathbf{u} is the proper velocity, \mathbf{v}_p is the peculiar velocity, and \mathbf{v}_h is the Hubble flow. Under the influence of a gravitational potential $\Phi(\mathbf{x}, t)$, the Lagrangian is:

$$L = \frac{1}{2}m\mathbf{u}^2 - m\Phi. \quad (3.24)$$

A canonical transformation of the Lagrangian is performed:

$$L \rightarrow L - \frac{d\psi}{dt}. \quad (3.25)$$

where

$$\psi = \frac{1}{2}ma\dot{a}\mathbf{x}^2. \quad (3.26)$$

This transformation leads to the modified Lagrangian:

$$L = \frac{1}{2}ma^2\dot{\mathbf{x}}^2 - m\phi(\mathbf{x}, t), \quad (3.27)$$

with the potential term:

$$\phi = \Phi + \frac{1}{2}\ddot{a}a\mathbf{x}^2. \quad (3.28)$$

The modified potential ϕ is governed by a modified Poisson equation, this can be obtained from Einstein field equations[74]:

$$\frac{1}{a^2}\nabla_{\mathbf{x}}^2\phi(\mathbf{x}, t) = 4\pi G\rho_b(t)\delta(\mathbf{x}, t). \quad (3.29)$$

This equation connects the potential to the density fluctuations $\delta(\mathbf{x}, t)$ in an expanding universe, where $\rho_b(t)$ is the background density.

3.2.2 Vlasov equation

The previous section described the motion of a single particle in expanding space under the influence of an external potential $\phi(\mathbf{x}, t)$, which is coupled to the overdensity field $\delta(\mathbf{x}, t)$ through the modified Poisson equation. The evolution of the entire fluid can be characterized using the phase-space density $f(\mathbf{x}, \mathbf{p}, t)$, which is defined through the

¹For more details, see [74].

relation:

$$dN = f(\mathbf{x}, \mathbf{p}, t) d^3\mathbf{x} d^3\mathbf{p}, \quad (3.30)$$

where dN represents the number of particles within a finite phase space volume V .

The real space proper density $\rho(\mathbf{x}, t)$ is obtained through integration of the phase space density over velocity space:

$$\rho(\mathbf{x}, t) = mn(\mathbf{x}, t) = \frac{m}{a^3} \int d^3\mathbf{p} f(\mathbf{x}, \mathbf{p}, t) = \frac{\rho_{b0}}{a^3} [1 + \delta(\mathbf{x}, t)]. \quad (3.31)$$

The expression assumes a non-relativistic fluid where the background density $\rho_b(t)$ follows the relation:

$$\rho_b(t) = \rho_{b0} a^{-3}, \quad (3.32)$$

where ρ_{b0} denotes the background density at redshift zero, and $n(\mathbf{x}, t)$ represents the proper number density of the non-relativistic fluid.

Liouville's theorem states that the phase space density of a collisionless fluid remains conserved over time. DM, characterized by negligible cross section and smoothly varying potential, represents a nearly perfect collisionless system. In the Newtonian limit, the phase space conservation can be expressed as:

$$\frac{df}{dt} = \frac{\partial f}{\partial t} + \{f, H\} = 0, \quad (3.33)$$

where the Poisson bracket $\{f, H\}$ is defined as:

$$\{f, H\} = \frac{\partial f}{\partial \mathbf{x}} \cdot \frac{\partial H}{\partial \mathbf{p}} - \frac{\partial f}{\partial \mathbf{p}} \cdot \frac{\partial H}{\partial \mathbf{x}}. \quad (3.34)$$

The application of the Hamiltonian derived earlier leads to the collisionless Boltzmann equation (also known as the Vlasov equation):

$$\frac{\partial f}{\partial t} + \frac{\mathbf{p}}{ma^2} \cdot \nabla_{\mathbf{x}} f - m \nabla_{\mathbf{x}} \phi \cdot \frac{\partial f}{\partial \mathbf{p}} = 0. \quad (3.35)$$

This equation describes the evolution of the phase space distribution function for a collisionless system under the influence of gravitational forces in an expanding universe. Due to the nonlinearity of the Boltzmann equation, general solutions cannot be obtained. A standard way to deal with Equation 3.35 is to take velocity moments.

For the zeroth moment, integrating Equation 3.35 over \mathbf{p} and dropping the surface term and we then get the continuity equation:

$$\frac{\partial \delta}{\partial t} + \frac{1}{a} \nabla_{\mathbf{x}} \cdot [\langle v \rangle (1 + \delta)] = 0, \quad (3.36)$$

where $\langle v \rangle$ is the local or mean streaming velocity, defined as:

$$\langle v \rangle = \frac{1}{na^3} \int d^3 \mathbf{p} f. \quad (3.37)$$

The momentum equations are expressed through the first moment of Equation 3.35, i.e. the multiplication of the Boltzmann equation by p_i and subsequent integration over momentum space:

$$\frac{\partial}{\partial t} [a \langle v_i \rangle (1 + \delta)] + \frac{\partial \phi}{\partial x_i} (1 + \delta) + \frac{\partial}{\partial x_j} [\langle v_i v_j \rangle (1 + \delta)] = 0, \quad (3.38)$$

where $\langle v_i v_j \rangle$ is the velocity stress tensor, defined as:

$$\langle v_i v_j \rangle = \frac{1}{na^3} \int d^3 \mathbf{p} \frac{p_i p_j}{(ma)^2} f. \quad (3.39)$$

Now from the continuity and momentum equation we can obtain

$$\frac{\partial^2 \delta}{\partial t^2} + 2 \frac{\dot{a}}{a} \frac{\partial \delta}{\partial t} = \frac{1}{a^2} \partial_i (1 + \delta) \partial^i \phi + \frac{1}{a^2} \partial^i \partial^j [\langle v_i v_j \rangle (1 + \delta)]. \quad (3.40)$$

For the regime where $\delta \ll 1$, approximate solutions can be found through linearization of equations 3.29 and 3.40. In this regime, the velocity shear becomes so the stress tensor becomes diagonal and the diagonal terms are given by $\sigma/\sqrt{3}$, where σ is the initial three dimensional fluid velocity dispersion. The linearization yields:

$$\frac{\partial^2 \delta}{\partial t^2} + 2 \frac{\dot{a}}{a} \frac{\partial \delta}{\partial t} = \frac{\sigma^2}{a^2} \nabla_x^2 \delta + 4\pi G \rho_b \delta. \quad (3.41)$$

The solution can be expressed through a Fourier transform:

$$\delta(x, t) = \int d^3 k \delta_k(t) e^{ik \cdot x}. \quad (3.42)$$

This transformation leads to the ordinary linear differential equation:

$$\frac{d^2 \delta_k}{dt^2} + 2 \frac{\dot{a}}{a} \frac{d \delta_k}{dt} = \left[4\pi G \rho_b(t) - \frac{\sigma^2(t) k^2}{a^2} \right] \delta_k. \quad (3.43)$$

3.2.3 Multi-fluid extension

This single-fluid description can be extended to a more realistic scenario involving multiple cosmic fluids (non-relativistic DM, baryons, radiation, etc.). The resulting set of equations takes the form:

$$\frac{d^2\delta_A}{dt^2} + 2\frac{\dot{a}}{a}\frac{d\delta_A}{dt} = \left[4\pi G\rho_A(t) - \frac{\sigma_A^2(t)k^2}{a^2} \right] \delta_A + 4\pi G \sum_B \rho_B(t)\delta_B, \quad (3.44)$$

where the subscript A and B denotes the fluid of interest and all other cosmic components respectively. δ_A represents perturbations in fluid A and δ_B represents perturbations in other components. $\rho_A(t)$ and $\rho_B(t)$ are the respective density functions of A and B . $\sigma_A(t)$ is the velocity dispersion of fluid A . The equation demonstrates the coupling between perturbations in different cosmic components.

3.2.4 Evolution of dark matter perturbations

At early times and scales well below the Hubble radius, DM perturbations exhibit distinct behavior in different cosmological epochs. The analysis begins by simplifying Equations 3.43 and 3.44, where we initially neglect the second term in the square brackets, as it becomes significant only at small scales (large k). A detailed analysis of this small-scale regime follows in the next section.

During the early universe, when considering scales well below the Hubble radius, perturbation in the dominant radiation component does not grow[75], eliminating the coupling term in Equation 3.44. In this regime, DM perturbations behave as a single non-relativistic fluid in a radiation-dominated universe, effectively reducing to Equation 3.43 with $\rho_b = \rho_m$.

Following [76], we introduce the parameter $\zeta = \rho_m/\rho_r = a/a_{eq}$, where a_{eq} represents the scale factor at matter-radiation equality. By applying the Friedmann equations and neglecting the subdominant cosmological constant, Equation 3.43 transforms into:

$$\frac{d^2\delta_k}{d\zeta^2} + \frac{2+3\zeta}{2\zeta(1+\zeta)} \frac{d\delta_k}{d\zeta} = \frac{3}{2} \frac{\delta_k}{\zeta(1+\zeta)}. \quad (3.45)$$

The growing solution to this equation takes the form:

$$\delta_+ \equiv D(a) \propto 1 + \frac{3}{2} \frac{a}{a_{eq}}. \quad (3.46)$$

Radiation Domination When $\zeta < 1$, perturbations maintain approximately constant amplitude. This could be understood physically as the rapid expansion of the universe during this era makes it difficult for matter to clump together. This is known as the Mészáros effect.

Matter Domination When $\zeta > 1$, perturbations exhibit linear growth with respect to the scale factor. Physically this could be understood as gravitational forces from matter can now overcome the universe's expansion has slowed enough to allow matter to cluster.

Λ domination As the cosmological constant becomes dominant, it significantly impacts

structure formation. In this regime, the growing solution to the perturbation equations must be determined through numerical calculations.

The emergence of cosmic structures marks a distinct transition in universe evolution. While perturbations do not grow during radiation domination, the onset of matter-radiation equality triggers the active phase of structure formation. This growth mechanism persists into the present epoch, although the increasing influence of the cosmological constant introduces a progressive dampening effect on structure formation rates. Here we discussed only the Newtonian treatment of perturbation theory; for relativistic or full general relativistic treatment see [74, 75].

3.3 Simpler way to understand the growth of dark matter perturbations

Let's consider a perturbation with mode or wavelength λ . For any given mode, we can determine when it enters the horizon (Hubble radius, $d_H \sim \frac{1}{H_0}$) at time t_{enter} . This leads to two possible scenarios:

1. When $t < t_{\text{enter}}$, the mode is outside the Hubble radius, meaning $\lambda > d_H$
2. When $t > t_{\text{enter}}$, the mode is inside the Hubble radius, meaning $\lambda < d_H$

For the condition $\lambda < d_H$, the general relativistic effects due to spacetime curvature become negligible, as these are small scales compared to the background curvature scale. In this case, a Newtonian approach is sufficient. However, when $\lambda > d_H$, the curvature of spacetime significantly affects the growth of the perturbation, requiring a full general relativistic treatment. Nevertheless, this can be understood in a simpler way, which is discussed next.

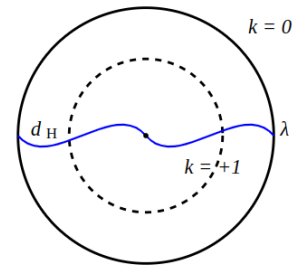
3.3.1 Mode outside the horizon: $\lambda > d_H$

Let us consider a spherical region (with $k = +1$) of matter with radius $\lambda > d_H$ with mean density ρ_1 , which is embedded inside a Friedmann universe with $k = 0$ having density ρ_0 such that $\rho_1 = \rho_0 + \delta\rho$. The inner region is not affected by the outside region.

Now for this two region we can write,

$$H_1^2 + \frac{1}{a_1^2} = \frac{8\pi G}{3}\rho_1; \quad H_0^2 = \frac{8\pi G}{3}\rho_0. \quad (3.47)$$

We will compare the perturbed universe with the background universe when their expansion rates are equal; i.e., we compare their densities at a time t when $H_1 = H_0$. We then get:



$$\frac{\rho_1 - \rho_0}{\rho_0} = \frac{\delta\rho}{\rho_0} = \frac{3}{8\pi G(\rho_0 a_1^2)}. \quad (3.48)$$

In general, if $H_0 = H_1$ at some time, then $a_0 \neq a_1$ at that time. However, if $(\delta\rho/\rho_0)$ is small, then a_1 and a_0 will differ by only a small quantity and we can set $a_1^2 \approx a_0^2$ in the right hand side. This allows us to find how $(\delta\rho/\rho_0)$ scales with a . Since $\rho_0 \propto a^{-4}$ in the radiation dominated phase ($t < t_{\text{eq}}$) and $\rho_0 \propto a^{-3}$ in the matter dominated phase ($t > t_{\text{eq}}$), we get:

$$\left(\frac{\delta\rho}{\rho}\right) \propto \begin{cases} a^2 & (\text{for } t < t_{\text{eq}}) \\ a & (\text{for } t > t_{\text{eq}}) \end{cases}, \quad (3.49)$$

t_{eq} is the time of matter-radiation equality. Thus, the amplitude of the mode with $\lambda > d_H$ always grows; as a^2 in the radiation dominated phase and as a in the matter dominated phase. The exact general relativistic approach gives the same scaling.

3.3.2 Mode inside the horizon; $\lambda < d_H$

When a mode enters the Hubble radius, two processes can inhibit its growth.

Jeans length The first is pressure support. If pressure builds up faster than gravitational collapse time scale, it prevents density contrast enhancement. This requires:

$$t_{\text{pressure}} \sim \frac{\lambda}{v} < t_{\text{grav}} \sim \frac{1}{\sqrt{G\rho}}, \quad (3.50)$$

where v is the velocity dispersion. This stability criterion implies that growth is suppressed for wavelengths below a critical value. The Jeans length is conventionally defined as ²:

$$\lambda_J = v \sqrt{\frac{\pi}{G\rho}}. \quad (3.51)$$

In multi-component systems, the pressure support and gravitational collapse may arise from different species. While baryonic pressure comes from collisions, DM's effective pressure stems from orbital readjustment. Nevertheless, in both cases, the pressure timescale is determined by the velocity dispersion v .

Rapid expansion The second inhibiting process occurs when the perturbed species is not the dominant one driving expansion, and the dominant species remains smoothly

²Another derivation of the Jeans length is when we analyze Equation 3.43 seeking growing density perturbations δ_k . The growth condition requires $\left[4\pi G\rho_b(t) - \frac{\sigma^2(t)k^2}{a^2}\right] \geq 0$. This mathematical approach yields an identical Jeans scale to that derived from timescale considerations.

distributed. Even if $\lambda > \lambda_J$ (meaning pressure cannot prevent collapse), rapid cosmic expansion can suppress growth. In radiation-dominated phases, this leads to:

$$t_{\text{exp}} \sim \frac{1}{\sqrt{G\rho_R}} < \frac{1}{\sqrt{G\rho_{\text{DM}}}} < t_{\text{pressure}}. \quad (3.52)$$

This expansion-driven suppression is the primary mechanism preventing growth during radiation domination. So perturbations evolve as follows:

- Radiation-dominated phase:
 - Only modes with $\lambda > d_H$ grow, scaling as a^2
 - For $\lambda < d_H$, rapid expansion prevents growth
- Matter-dominated phase:
 - Modes with $\lambda \gg \lambda_J$ grow as a
 - Modes with $\lambda \geq \lambda_J$ grow more slowly due to pressure effects

3.4 The free streaming length scale

Let us consider the evolution of DM perturbations. And lets focus on the scales close to the Jeans scale. For DM perturbations the Jeans length evolves as (from Equation 3.51):

$$\lambda_J \propto \frac{v}{\sqrt{\rho_{\text{dom}}}} \propto \begin{cases} a^2 & (a < a_{\text{nr}}) \\ a & (a_{\text{nr}} < a < a_{\text{eq}}) , \\ a^{1/2} & (a_{\text{eq}} < a) \end{cases} \quad (3.53)$$

where:

- ρ_{dom} is the density of the dominant background component which transitions from $\propto a^{-4}$ (radiation) to $\propto a^{-3}$ (matter) at a_{eq}
- $v \propto 1$ (relativistic) when $a < a_{\text{nr}}$, changes to $v \propto a^{-1}$ (non-relativistic) at a_{nr} and afterwards.
- a_{eq} is the time of matter radiation equality.
- $a_{\text{eq}}, a_{\text{nr}}$ is the time when DM becomes non relativistic. DM become non relativistic well before matter radiation equality.

As we know below this length scale perturbation can not grow due to the pressure support, so no structure can grow below the Jeans scale. A more intuitive scale can be Jeans mass, M_J , which is defined as

$$M_J \equiv \frac{4\pi}{3} \rho_{\text{DM}} \left(\frac{\lambda_J}{2} \right)^3. \quad (3.54)$$

Note that λ_J depends on ρ_{dom} (background dominant component), the conversion between Jeans length and Jeans mass requires the DM density, ρ_{DM} , which has the behaviour

$$\rho_{\text{DM}} \propto \begin{cases} a^{-4} & \text{for } a < a_{\text{nr}} \\ a^{-3} & \text{for } a > a_{\text{nr}} \end{cases}. \quad (3.55)$$

Now we can trace the evolution of the Jeans mass M_J .

$$M_J \propto \begin{cases} a^2 & (a < a_{\text{nr}}) \\ \text{constant} & (a_{\text{nr}} < a < a_{\text{eq}}) \\ a^{-3/2} & (a_{\text{eq}} < a) \end{cases}. \quad (3.56)$$

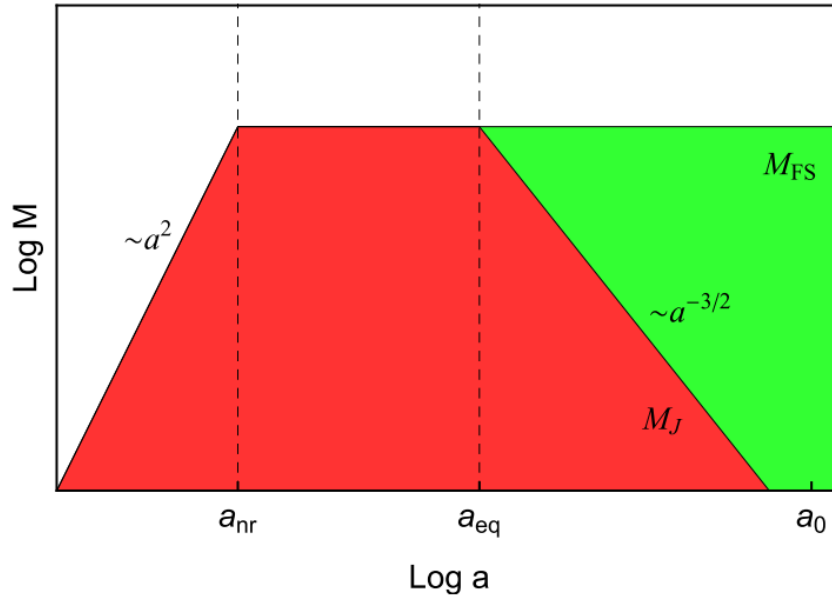


Figure 3.1: Evolution of cosmic structure formation barriers: M_J (Jeans mass) and M_{FS} (free streaming mass) across cosmic time. The highlighted red zone indicates suppressed growth of density fluctuations due to pressure support exceeding gravitational effects. In the green region, although gravity dominates pressure forces, particle velocities completely erased potential structures through free streaming. Figure from [77]

Figure 3.1 summarises the evolution of the Jeans mass through different cosmological epochs.

DM particles, unlike regular gas molecules, don't interact through collisions but follow geodesic paths in spacetime. While we can model their collective behavior using an effective pressure in fluid approximations, this only works at large scales. At smaller scales, particles freely move between overdense and underdense regions along their geodesics, naturally smoothing out density variations through a process called free streaming. A perturbation mode with proper wavelength $\lambda(t)$ experiences dissipation due to free streaming when the proper distance which a DM particle can travel in time t

in the background spacetime, ℓ_{FS} satisfy $\ell_{\text{FS}}(t) > \lambda(t)$. Now

$$\ell_{\text{FS}}(t) = a(t) \int_0^t \frac{v(t')}{a(t')} dt'. \quad (3.57)$$

Now considering the the evolution of scale factor, background density and the velocity dispersion across different epochs.

- $0 < t < t_{\text{nr}}$: DM particles are relativistic, $v \approx 1$ and $a(t) \propto t^{1/2}$.
- $t_{\text{nr}} < t < t_{\text{eq}}$: $v \propto a^{-1}$ and $a(t) \propto t^{1/2}$.
- $t \gg t_{\text{eq}}$: $v \propto a^{-1}$ and $a(t) \propto t^{2/3}$.

With these we can find [75],

$$\frac{\ell_{\text{FS}}(t)}{a(t)} = \begin{cases} (2t_{\text{nr}}/a_{\text{nr}}^2)a = (2t/a) & t < t_{\text{nr}} \\ (2t_{\text{nr}}/a_{\text{nr}})[1 + \ln(a/a_{\text{nr}})] & t_{\text{nr}} < t < t_{\text{eq}} \\ (2t_{\text{nr}}/a_{\text{nr}})[(5/2) + \ln(a_{\text{eq}}/a_{\text{nr}})] & t_{\text{eq}} \ll t \end{cases}. \quad (3.58)$$

We can see that $\frac{\ell_{\text{FS}}}{a}$ reaches to a maximum value at t_{eq} . Which is given by

$$\lambda_{\text{FS}} = \left(\frac{2t_{\text{nr}}}{a_{\text{nr}}} \right) \left(\frac{5}{2} + \ln \frac{a_{\text{eq}}}{a_{\text{nr}}} \right). \quad (3.59)$$

The comoving free streaming length λ_{FS} represents the maximum distance particles traverse before t_{eq} , when the Jeans length rapidly decreases and gravitational collapse becomes possible. While perturbations larger than λ_{FS} persist, smaller-scale fluctuations ($\lambda < \lambda_{\text{FS}}$) are erased by free streaming before Jeans instability can take effect, preventing structure formation at these scales.

3.5 The Halo Mass Function

The foundation of cosmic structure formation lies in the growth of initial density perturbations. While these perturbations evolve linearly when overdensities are small ($\delta \ll 1$), the physics becomes significantly more complex as they approach and exceed unity ($\delta \geq 1$). At this point, the coupled system of Poisson and Vlasov equations (Equations 3.29 and 3.38) requires direct numerical solutions to understand the full non-linear dynamics.

The advent of large-scale N-body simulations [78–81] revolutionized our understanding of structure formation within the Λ CDM framework. These simulations revealed how DM aggregates into gravitationally bound structures known as halos. However, they were limited by their focus on DM alone, unable to directly model the baryonic matter that dominates astronomical observations.

To address this limitation, the field evolved toward cosmological hydrodynamical simulations [82]. Modern implementations, including Horizon-AGN, MassiveBlack-II, Illustris, and EAGLE [83–86], now simultaneously model DM evolution alongside complex baryonic processes such as star formation, black hole growth, and chemical enrichment. These simulations span impressive scales, from scales exceeding 100 Mpc down to kiloparsec-scale galactic structures.

A key prediction emerging from both theoretical models and numerical simulations is the clustering of DM into massive, gravitationally bound structures called halos. The halo mass function (HMF) quantifies the abundance of DM halos as a function of their mass per unit comoving volume. The HMF is sensitive to cosmological parameters, particularly the mass-energy density of DM (Ω_c) and dark energy (Ω_Λ) [87]. Furthermore, it offers insights into the nature of DM. In the Cold Dark Matter (CDM) paradigm, the HMF exhibits an approximate power-law behavior, with halo numbers scaling as $M^{-1.8}$ [88, 89]. This relationship notably differs in alternative scenarios such as Warm Dark Matter (WDM) models, which predict a suppression of low-mass halos [90].

3.5.1 Approximative analytical approach

Nonlinear structure formation can be analytically approximated using the Press-Schechter (PS) model [78]. The model describes spherical collapse where a tophat spherical overdensity, initially following the Hubble flow, undergoes amplification, decouples, and eventually collapses and virializes. This collapse occurs when the linear overdensity reaches the critical threshold $\delta_c = 1.686$.

The cumulative probability of collapse for a region of size R is described by:

$$F(R) = \int_{\delta_c}^{\infty} P(\delta|R)d\delta = \frac{1}{2}\text{erfc} \left[\sqrt{\frac{\nu}{2}} \right], \quad (3.60)$$

where $\nu = [\delta_c/\sigma(R)]^2$ and $\sigma(R)$ is the rms variance of mass within a sphere of radius R that contains mass M . $P(\delta|R)$ follows a Gaussian distribution.

The probability distribution of overdensities can be visualized through Gaussian curves with varying σ values, corresponding to different smoothing scales R . Larger values of σ (flatter curves) represent smaller smoothing scales. The probability of collapse, represented by the area where $\delta > \delta_c$, increases as R decreases (see Figure 3.2), demonstrating that smaller structures are more likely to form. This mathematical behavior directly reflects the hierarchical nature of structure formation in Λ CDM cosmology.

Within the Λ CDM framework, the temporal evolution of $\sigma(R)$ is governed by $\sigma(R) = D(a)\sigma_0(R)$, with $D(a)$ representing the growth factor. This causes the Gaussian curves to flatten over time and increasing the collapse probability $F(R)$. Alternatively, keeping σ fixed while evolving the threshold as $\delta_c \propto 1/D(a)$ provides an equivalent description, visualized as the threshold (vertical dashed line in Figure 3.2) moving leftward in the probability distribution.

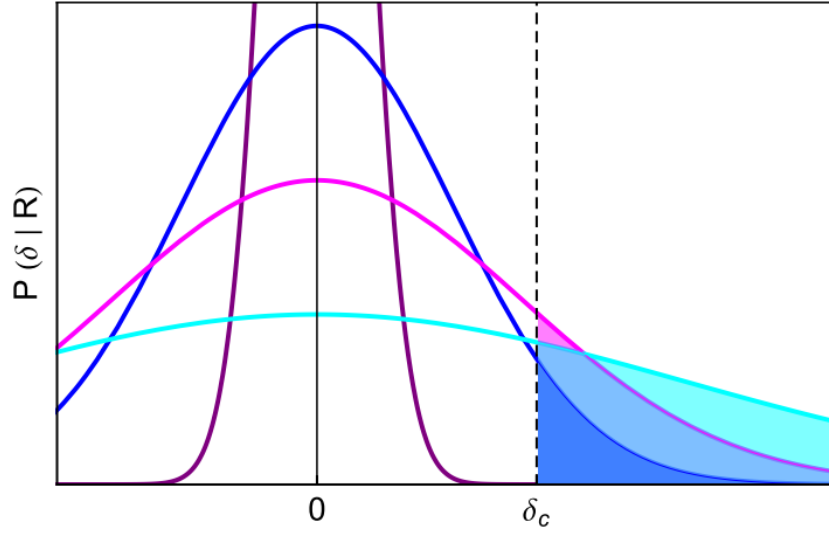


Figure 3.2: Gaussian probability distribution of density perturbations at different smoothing scales. Each curve represents a different variance $\sigma^2(R)$, where flatter distributions correspond to larger variances and smaller smoothing scales R . The shaded region above the critical density δ_c represents the cumulative collapse probability $F(R)$, which increases with decreasing smoothing scale. Figure from [77].

The HMF, expressing the differential number density of halos with mass $M = \frac{4}{3}\pi\rho_0 R^3$, takes the form:

$$\frac{dn}{d \log M} = \frac{\rho_0}{M} \left| \frac{dF(M)}{d \log M} \right| = -\frac{1}{2} \frac{\rho_0}{M} f_{\text{PS}}(\nu) \frac{d \log \sigma^2}{d \log M}, \quad (3.61)$$

where $f_{\text{PS}}(\nu) = \sqrt{\frac{2\nu}{\pi}} \exp[-\frac{\nu}{2}]$.

While this model employs simplified assumptions, it achieves reasonable concordance with Λ CDM simulations, though requiring a factor of 2 correction to properly account for the total mass fraction.

The Extended Press-Schechter (EPS) model improves upon the original PS model by solving the cloud-in-cloud problem - where underdense regions within larger overdense regions weren't properly counted as collapsed. EPS tracks overdensity patches across scales and counts them as virialized at their first threshold crossing, yielding the same mass function as PS but without needing a fudge factor of 2. This approach enables more sophisticated modeling, such as replacing spherical collapse with ellipsoidal collapse.

3.5.2 Fits from numerical simulations

While Press-Schechter formalism offered an analytical approach to derive the HMF, cosmological N-body simulations later revealed its limitations in predicting halo abundances across mass ranges [88, 91, 92]. In describing the DM halo distribution, we

express the comoving number density of haloes per unit logarithm of mass as:

$$\frac{dn}{d \ln M} = M \cdot \frac{\rho_0}{M^2} f(\sigma) \left| \frac{d \ln \sigma}{d \ln M} \right|. \quad (3.62)$$

In this formulation of the HMF, $f(\sigma)$ serves as the fitting function derived from N-body simulations, while ρ_0 represents the universe's mean density. The parameter σ characterizes the mass variance within a spherical volume of radius R , which contains a mass $M = \frac{4\pi\rho_0}{3} R^3$. This variance is quantified through the integral:

$$\sigma^2(R) = \frac{1}{2\pi^2} \int_0^\infty k^2 P(k) W^2(kR) dk. \quad (3.63)$$

The components of this integral include the wavenumber k , the linear power spectrum $P(k)$, and the Fourier transform of the top-hat window function $W(kR)$. Various forms of the fitting function $f(\sigma)$ have emerged in different literatures, two of such fits given by refs. [93, 94] are used in this thesis to probe cosmology and DM from strongly lensed gravitational waves. Table 1 of [95] provides a concise summary of the forms for $f(\sigma)$ that have appeared in different literatures and which are included in the package HMFcalc. These HMF fits are mostly validated within the mass range of $\sim 10^8 - 10^{15} M_\odot$.

3.5.3 Dependence on redshift and cosmology

The redshift evolution of the HMF enters through $\sigma(M, z)$, with $f(\sigma)$ remaining redshift-independent. This evolution is governed by the growth factor:

$$d(z) = \frac{D_+(z)}{D_+(z=0)}, \quad (3.64)$$

where $D_+(z)$ is given by:

$$D_+(z) = \frac{5\Omega_m}{2} \frac{H(z)}{H_0} \int_z^\infty \frac{(1+z') dz'}{[H(z')/H_0]^3}, \quad (3.65)$$

with the Hubble parameter:

$$H(z) = H_0 \sqrt{\Omega_m(1+z)^3 + (1-\Omega_m)}, \quad (3.66)$$

considering flat Λ CDM cosmology with $\Omega_r = 0$, where Ω_r is the radiation density at current epoch.

This formulation shows the connections between HMF, cosmic structure formation at different redshifts, and the underlying cosmological parameters.

Within the Press-Schechter formalism, the redshift evolution of the HMF reflects the increasing critical collapse threshold as we look further back in cosmic time. This

mathematical framework naturally explains hierarchical structure formation since density fluctuation variance $\sigma^2(M)$ inversely correlates with mass in CDM cosmologies. Consequently, smaller-scale regions with their larger fluctuation amplitudes exceed the collapse threshold earlier, forming low-mass halos first. Meanwhile, larger structures with smaller amplitude fluctuations require more time to reach the critical density. Cosmic evolution progressively lowers the effective critical threshold relative to the growing fluctuation amplitudes, enabling the formation of increasingly massive structures over time. The Press-Schechter mass function quantitatively captures this process, demonstrating an exponentially fewer massive halos at high redshifts and predicting their gradual buildup through mergers and accretion of smaller structures. This bottom-up formation sequence emerges naturally from the statistical nature of the initial density field as mathematically expressed in the Press-Schechter framework.

4 | Cosmography Using Strongly Lensed Gravitational Waves from Binary Black Holes

4.1 Introduction

The next (third) generation (XG) of gravitational-wave (GW) detectors will observe a large number of compact binary mergers out to large distances. The expected detection rates of binary-black-hole (BBH) and binary-neutron-star (BNS) mergers are $\sim 10^5 - 10^6$ per year [96, 97]. These detectors will observe BBH mergers out to redshifts as large as $z \sim 100$ [98], providing new avenues to probe cosmology that complement other observations. For example, any black holes (BHs) observed at very high redshifts ($z \gtrsim 10$) are unlikely to be of stellar origin as this is before the epoch of star formation. Hence any observation of BBHs at such redshifts will provide a strong hint on the existence of primordial BHs, which will also have implications on our understanding of DM.

GW observations of compact binary mergers will allow us to measure the luminosity distance d_L accurately without using any distance ladders, as these objects are absolutely calibrated *standard sirens* [99, 100]. An EM counterpart of the merger will enable us to measure their redshifts, thus allowing us to populate the Hubble diagram. Due to the limited horizon of EM telescopes such measurements are likely to be possible only at lower redshifts ($z \lesssim 0.5$). Thus, such measurements will primarily track the Hubble law $d_L(z) \simeq H_0^{-1}z$, thus providing precise measurement of the Hubble constant. Using GW standard sirens, XG detectors could not only enable a stringent constraint on H_0 , but also potentially provide precise measurements of other cosmological parameters, such as the matter density Ω_m and cosmological constant density Ω_Λ of the flat Λ CDM cosmological model [101–105]. While precise estimates of these parameters have been obtained from the study of the cosmic microwave background (CMB) [106], Type Ia supernovae [107] and others, there is considerable value in providing independent constraints using GWs. Currently, there appears to be an inconsistency between the high-redshift ($z \sim 1000$) CMB data and the low-redshift ($z \lesssim 2$) probes such as supernovae [107]. This could be a result of unknown systematic errors or point to the breakdown of the

Λ CDM model. The systematic errors of such GW-based measurements are much better understood than, say, that of Type 1a supernovae. Hence, such observations will greatly aid resolving the current Hubble tension [108, 109].

At high redshifts ($z \gtrsim 0.5$), it is difficult to observe EM counterparts of compact binary mergers [110]. Additionally, BBH mergers, which can be seen out to very high redshifts, are generally not expected to produce EM counterparts. However, even in the absence of EM counterparts, statistical correlation of the mergers with large scale structure will provide some way of inferring cosmological parameters [111–115]. Here the Hubble diagram will contain imprints of other cosmological parameters such as the DM energy density and the equation of state of the dark energy. Thus they will provide strong tests of cosmological models, such as the currently favoured Λ CDM model [72].

We are unable to measure cosmological redshifts from BBH observations because the masses are degenerate with redshift in the GW signal, thanks to the absence of a preferred mass scale in GR. However, non-gravity physics in compact objects and their progenitors could introduce particular mass scales in compact binaries. For example, neutron stars have a maximum mass that depends on the nuclear equation of state [116] and the BH mass distribution can have some features due to pair instability supernovae [117–120]. If such features are well understood (see e.g. [121, 122] for some caveats), they will enable redshifts measurements from compact binaries purely using GW observations [123–128]. Such *spectral sirens* will also enable GW cosmography.

GW standard sirens can also probe another signature of the dark energy sector that is not accessible to EM observations. A generic modified gravity theory induces modifications in the evolution of the cosmological background and perturbations, with respect to the standard model of cosmology. In some modified theories, GWs propagate at the speed of light but their amplitude will decrease differently from general relativity (GR). Consequently, the luminosity distance estimated from the GW standard sirens would differ from that estimated from their EM counterparts. The next generation detectors will be able search for this deviation, probing multiple classes of modified theories of gravity in the context of cosmology [129, 130].

GW observations will also probe the large scale structure of the universe. The inhomogeneities in the spatial distribution of the observed compact binary mergers will be another tracer of the large scale structure, which can be measured by the two-point (and higher order) correlation functions [131]. This will complement the large-scale galaxy and quasar surveys using EM telescopes: GW observations will probe much deeper in redshift, although their spatial resolution will be much poorer than the EM surveys. GW observations of BNSs will be able to accurately measure the scale of baryon acoustic oscillations [132], providing an independent probe of the cosmological model.

In this Chapter, we present a new cosmological probe that GW observations will enable, making use of strongly lensed GWs. As discussed in Chapter 2, GR predicts that intervening massive objects such as galaxies and clusters between the GW source and the observer will deflect the GWs through the phenomenon of gravitational lensing. If the lensing objects are sufficiently massive and compact, and lie sufficiently close to the line

of sight to the source, they can create multiple images of the source. This phenomenon, called strong gravitational lensing, is routinely observed in EM observations of galaxies, clusters, quasars, etc. The same objects should strongly lens GW signals as well. The precise fraction of strongly lensed GW sources will depend on the distribution of the GW sources, galaxies and clusters that act as lenses as well as the cosmological model and parameters. According to recent calculations, this fraction is $\sim 0.01 - 0.05\%$ for current generation detectors [133, 134] and $\sim 0.1 - 1\%$ for the XG detectors [48, 57, 135–141]. Since XG detectors are expected to detect millions of compact binary mergers during their operation, they will detect thousands or tens of thousands of strongly lensed GWs.

The most famous cosmological probe involving strong lensing is the use of measured time delays to infer H_0 : this method requires building detailed mass models for gravitational lenses that host multiple images of background sources. These models, along with measured time delays, enable system-by-system constraints, which can be combined to get a better measurement of H_0 , and even other cosmological parameters, from a catalog of such systems (see [142] for a recent review). The dependence of lensing time delay on cosmological parameters is degenerate with the lens parameters and the source location, which are usually difficult to precisely constrain in the absence of an EM counterpart. Hence previous work [143] in GW time-delay cosmography relied on the existence of an EM counterpart. This requires at least one of the compact objects in the binary to be a neutron star, and the mass ratio to be moderate, effectively restricting this method to low-mass binaries only. The horizon distance of 3G detectors to such low-mass binaries is modest ($z \lesssim 2$). Further, even with the best EM telescopes¹, the detectability of faint EM counterparts such as kilonovae is restricted to smaller redshifts ($z \lesssim 0.5$) [110]. These limitations would make this essentially a probe of cosmology at low redshifts.

In this work, we propose a *statistical* probe of cosmology that uses population-level properties of a catalog of lensed GW detections to constrain cosmology. This method is related to previous proposals to statistically infer cosmological parameters from distributions of image separations [152–155] and time delays [156–159] in lensed quasars. Although the theory of lensing of GWs is essentially similar to the lensing of EM waves, there are some important practical differences. Thanks to their short wavelengths, EM observations will allow us to spatially resolve the multiple images of strongly lensed objects. However, multiple images of strongly lensed GW sources cannot be spatially resolved due to their poor sky localisation. In contrast, compact binary mergers produce transient GW signals, which can be temporally localised to milliseconds. This means that the time delay between the lensed images of the same merger can be measured with exquisite precision using GW observations, which is hard to do in EM lensing (e.g. in quasar lensing, using the quasar light curves). Moreover, GWs are unaffected by issues such as extinction (which is a potential source of systematic error for quasar

¹Different optical surveys such as The Sloan Digital Sky Survey (SDSS; [144]), Dark Energy Survey (DES; [145]), Zwicky Transient Facility (ZTF; [146]), The Large Synoptic Survey Telescope (LSST; [147]), Wide-Field Infrared Survey Telescope (WFIRST; [148]), Swift-Burst Alert Telescope (Swift-BAT; [149]) and Fermi-Gamma-ray Burst Monitor (Fermi-GBM; [150]), Canadian Hydrogen Intensity Mapping Experiment (CHIME; [151]) and various others transient surveys [110]

cosmography [160]) and in general have a much simpler and well-modeled selection function. In principle this method would probe the cosmology using data from redshifts ($z \sim 2 - 15$) that are not probed by the CMB or other EM observations.

The idea of the new method is that the precise number of strongly lensed GW events and the distribution of their lensing time delay depends on the cosmological model and parameters, apart from the distribution of GW sources and lenses [57]. If the latter two are known, then this will provide a new means of probing the cosmological parameters. The distribution of GW sources can be accurately determined by the large number of un-lensed signals that will dominate the data (see, e.g., [161]). The knowledge of the distribution of large gravitational lenses should come from cosmological simulations and EM observations². However, we will also show that the cosmological parameters and the model of the distribution of the lenses have sufficiently different imprints on the number of strong lensed events and their time delays, so that it is possible to disentangle these effects to a very good extent.

Our statistical method, based on the observation of a large number of strongly lensed BBH events, does not require the presence of EM counterparts to the mergers. A complementary approach, presented in [143, 162, 163], makes use of a much smaller number of strongly lensed mergers having an EM counterpart. The concurrent observation of lensed EM and GW signals will allow us to measure cosmological parameters from even a single event. However, due to the limited observing horizon of EM telescopes, such observations will be able to probe only low-redshift ($z \lesssim 0.5$) cosmology³.

This chapter is organised as follows: In Section 4.2 we briefly review the Bayesian method that we use to constrain the cosmological parameters from the observation of a population of strongly lensed GW signals. Section 4.3 addresses the modeling of time delay distributions and expected lensed event counts across cosmological parameters. Section 5.5 presents forecasted constraints on cosmological parameters. Section 4.5.1 explores these constraints under various astrophysical models for the redshift distribution of BBH mergers. In the remaining sections we investigate the various sources of systematic errors in our analysis, and show that it is possible to bring them sufficiently small so that interesting measurements are possible in the future. In particular, in Section 4.5.2, we explore how the errors in the measurement of the luminosity distance of individual GW events will limit our ability to reconstruct the true redshift distribution of GW sources, hence biasing our cosmological inference. In Section 4.5.3, we investigate how our inaccurate understanding of the lens distributions will bias our cosmological inference. In Section 4.5.4 we will explore how we can deal with contaminated data – that is, we develop a formalism deal with the presence of a small number of unlensed GW signals in our lensing data, that are misidentified as lensed events due to our limited ability to distinguish between lensed and unlensed GW signals.

²See [135] for a complementary approach to constrain the distribution of the GW sources and lenses from the lensing rate and time delay distribution, assuming a cosmology.

³Combining GW lensing observations with lenses detected in EM surveys (e.g., Euclid, CSST and JWST) could probe cosmology at moderate redshifts ($z \lesssim 2$) [141, 164]. However, the exact method for this approach is yet to be developed.

4.2 Bayesian inference of cosmological parameters

We assume that N lensed BBH mergers have been detected within an observation period T_{obs} . In this work, we assume a SIS lens model. Thus, each will produce two lensed copies of the GW signal. We also assume that these two images are detected, from which the lensing time delays have been measured accurately. Since the time delays are measured with millisecond precisions we can take them as point estimates, which we denote as $\{\Delta t_i\}_{i=1}^N$. Given N and $\{\Delta t_i\}_{i=1}^N$, we wish to compute the posterior distribution of the cosmological parameters $\vec{\Omega} \equiv \{H_0, \Omega_m\}$ assuming a flat Λ CDM cosmological model. Using Bayes' theorem:

$$p(\vec{\Omega} | N, \{\Delta t_i\}, T_{\text{obs}}, \mathcal{M}) = \frac{p(\vec{\Omega} | \mathcal{M}) p(N, \{\Delta t_i\} | \vec{\Omega}, T_{\text{obs}}, \mathcal{M})}{p(N, \{\Delta t_i\} | T_{\text{obs}}, \mathcal{M})}, \quad (4.1)$$

where $p(\vec{\Omega} | \mathcal{M})$ is the prior distribution of $\vec{\Omega}$ given some model \mathcal{M} while $p(N, \{\Delta t_i\} | \vec{\Omega}, T_{\text{obs}}, \mathcal{M})$ is the likelihood of observing N lensed events with time delays $\{\Delta t_i\}_{i=1}^N$ given the set of cosmological parameters $\vec{\Omega}$ and model \mathcal{M} . The normalisation constant $p(N, \{\Delta t_i\} | \mathcal{M})$ is the evidence of the assumed model \mathcal{M} .

$$p(N, \{\Delta t_i\} | T_{\text{obs}}, \mathcal{M}) = \int p(\vec{\Omega} | \mathcal{M}) p(N, \{\Delta t_i\} | \vec{\Omega}, T_{\text{obs}}, \mathcal{M}) d\vec{\Omega}. \quad (4.2)$$

Above, \mathcal{M} denotes a variety of model assumptions that we employ, including the cosmological model, models of the mass distribution of DM halos that act as lenses, lens models, etc. From here onwards, we will drop \mathcal{M} from the expressions, for simplicity of notation.

Since N and $\{\Delta t_i\}$ are independent data, the likelihood can be written as a product of likelihoods of measuring N lensed events and the set of time delays $\{\Delta t_i\}_{i=1}^N$.

$$p(N, \{\Delta t_i\} | \vec{\Omega}, T_{\text{obs}}) = p(N | \vec{\Omega}, T_{\text{obs}}) p(\{\Delta t_i\}_{i=1}^N | \vec{\Omega}, T_{\text{obs}}). \quad (4.3)$$

Here, the likelihood of observing N lensed BBH mergers can be described by a Poisson distribution with mean $\Lambda(\vec{\Omega}, T_{\text{obs}})$.

$$p(N | \vec{\Omega}, T_{\text{obs}}) = \frac{\Lambda(\vec{\Omega}, T_{\text{obs}})^N e^{-\Lambda(\vec{\Omega}, T_{\text{obs}})}}{N!}. \quad (4.4)$$

Above, $\Lambda(\vec{\Omega}, T_{\text{obs}})$ is the expected total number of lensed events within the observation period as predicted by the cosmological model with parameters $\vec{\Omega}$. Assuming that BBH mergers are independent events, the likelihood for observing the set of time delays $\{\Delta t_i\}_{i=1}^N$ can be written as the product of individual likelihoods.

$$p(\{\Delta t_i\}_{i=1}^N | \vec{\Omega}, T_{\text{obs}}) = \prod_{i=1}^N p(\Delta t_i | \vec{\Omega}, T_{\text{obs}}). \quad (4.5)$$

Above, $p(\Delta t_i | \vec{\Omega}, T_{\text{obs}})$, can be thought of as a ‘‘model’’ time-delay distribution $p(\Delta t | \vec{\Omega}, T_{\text{obs}})$ evaluated at the measured Δt_i of a lensed merger. The shape of the model distribution is governed by the cosmological parameters $\vec{\Omega}$. The model distribution $p(\Delta t | \vec{\Omega}, T_{\text{obs}})$ is obtained from the expected (intrinsic) time delay distribution $p(\Delta t | \vec{\Omega})$, after applying the condition that we can not observe the time delays which are greater than the observation time T_{obs} :

$$p(\Delta t | \vec{\Omega}, T_{\text{obs}}) \propto p(\Delta t | \vec{\Omega}) (T_{\text{obs}} - \Delta t) \Theta(T_{\text{obs}} - \Delta t), \quad (4.6)$$

where Θ denotes the Heaviside step function.

4.3 Modelling the expected number of lensed events and lensing time delays

The Bayesian inference presented in Section 4.2 essentially involves comparing the observed number of lensed events N and the distribution of their time delays $\{\Delta t_i\}_{i=1}^N$ with the theoretical prediction of the expected number of lensed events $\Lambda(\vec{\Omega}, T_{\text{obs}})$ and their time delay distribution, $p(\Delta t | \vec{\Omega})$, as a function of the parameters $\vec{\Omega}$. Here we describe how these quantities can be modelled using a cosmological model. We assume the flat Λ CDM model. However, similar calculations can be performed using more general cosmological models as well.

4.3.1 Expected number of lensed events:

To compute the expected number of lensed binaries, we convolve the redshift distribution of merging binaries with the strong lensing probability at that source redshift.

$$\Lambda(\vec{\Omega}, T_{\text{obs}}) = \mathcal{S}(T_{\text{obs}}) \times R \int_0^{z_s^{\text{max}}(\vec{\Omega})} p_b(z_s | \vec{\Omega}) P_\ell(z_s | \vec{\Omega}) dz_s, \quad (4.7)$$

Above, R is the BBH detection rate, $p_b(z_s | \vec{\Omega})$ is the redshift distribution (probability density) of merging binaries and $P_\ell(z_s | \vec{\Omega})$ is the strong lensing probability for the source redshift z_s . Here we assume that the GW detectors are able to detect all the merging binaries out to z_{max} . For XG detectors, this is a good assumption for the z_{max} values that we use⁴. $\mathcal{S}(T_{\text{obs}})$ denotes the selection effects due to the finite observing time

$$\mathcal{S}(T_{\text{obs}}) = \int_{\Delta t=0}^{T_{\text{obs}}} p(\Delta t | \vec{\Omega}) (T_{\text{obs}} - \Delta t) d\Delta t. \quad (4.8)$$

This takes into account the fact that if the lensing time delay Δt is comparable to the observing time T_{obs} the second (first) image will be missed unless the first (second)

⁴The z_{max} predicted by a source population model (e.g., [165]) assumes the standard cosmology $\vec{\Omega}_{\text{true}}$. For the population models that we consider, $z_{\text{max}} \simeq 20$. When we consider other values of $\vec{\Omega}$, we rescale z_{max} appropriately.

image arrives at the beginning (end) of the observing run.

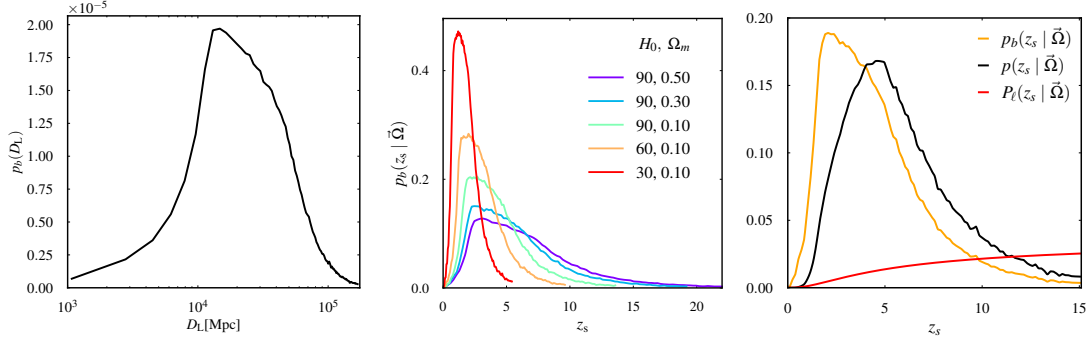


Figure 4.1: *Left Panel:* The redshift distribution of BBH mergers from [165] converted to a luminosity distance distribution, assuming standard cosmology [106]. *Middle Panel:* Source redshift distributions, converted from the aforementioned luminosity distance distribution, assuming different values of $\vec{\Omega}$. *Right Panel:* The source redshift distribution $p_b(z_s | \vec{\Omega})$ from [165], and the lensing probability $P_\ell(z_s | \vec{\Omega})$ assuming the halo mass-function described in [93]. The competing effects of a decreasing probability of sources and increasing probability of lensing at high redshifts is reflected in the shifted peak of the distribution of lensed sources $p(z_s | \vec{\Omega})$ to higher redshifts. Here $\vec{\Omega} = \{H_0 = 67.3 \text{ km s}^{-1}\text{Mpc}^{-1}, \Omega_m = 0.316\}$.

We expect that the rate R of the BBH mergers and their redshift distribution $p_b(z_s | \vec{\Omega})$ will be accurately measured from the large ($\sim 10^6$) number of unlensed events that will dominate the data. What we measure from GW observations is the distribution $p_b(d_L)$ of luminosity distance of the sources, which can then be converted into a redshift distribution $p_b(z_s | \vec{\Omega})$ assuming a set of cosmological parameters $\vec{\Omega}$. For the forecast analysis presented here, we create a luminosity distance distribution from a redshift distribution model, assuming standard cosmological parameters $\vec{\Omega}_{\text{true}}$. By varying $\vec{\Omega}$, we can then obtain different redshift distributions which we use to model the time delay distribution for that specific value of $\vec{\Omega}$. This is demonstrated in Figure 4.1. Since these quantities are currently poorly constrained, we rely on theoretical models of $p_b(z_s | \vec{\Omega})$ to forecast the expected precision in measuring cosmological parameters. We present results for several BBH detection rates, R . In Section 4.5, we extend this analysis by considering various theoretical models to predict the precision of cosmological parameter measurements.

To compute the expected number of lensed events using Equation 5.14, we also need to know the probability $P_\ell(z_s | \vec{\Omega})$ that a source at redshift z_s is strongly lensed. This will depend on the distribution of lenses as well as cosmological parameters. We assume that the lenses are modelled by the SIS model. Multiple images are produced when the projected location of the source in the lens plane is within the Einstein radius of the lens, given by

$$r_E(\sigma, z_\ell, z_s, \vec{\Omega}) = 4\pi \left(\frac{\sigma}{c}\right)^2 \frac{D_{\Delta t}}{1 + z_\ell} \left(\frac{D_{\ell s}}{D_s}\right)^2 \quad (4.9)$$

where σ is the line-of-sight velocity dispersion of the lens, $D_{\Delta t} \equiv (1 + z_\ell) \frac{D_s D_\ell}{D_{ls}}$ is called the time delay distance where D_ℓ, D_s and D_{ls} are the angular diameter distance to the lens, to the source, and between the lens and the source, respectively and σ is the velocity dispersion of the lens. The strong lensing probability is given by integrating the differential optical depth for strong lensing by different lenses

$$P_\ell(z_s, \vec{\Omega}) = \int_0^{z_s} \int_{\sigma_{\min}}^{\sigma_{\max}} \frac{d\tau}{dz_\ell d\sigma}(z_s, z_\ell, \sigma, \vec{\Omega}) dz_\ell d\sigma, \quad (4.10)$$

where the differential optical depth for strong lensing by a lens with velocity dispersion σ located at a redshift z_ℓ is given by the fraction of the full sky covered by lenses

$$\frac{d\tau}{dz_\ell d\sigma}(z_s, z_\ell, \sigma, \vec{\Omega}) = \frac{dV_c}{dz_\ell}(z_\ell, \vec{\Omega}) \times \frac{dN_\ell}{dV_c d\sigma}(z_\ell, \sigma, \vec{\Omega}) \times \frac{\pi r_E^2(\sigma, z_\ell, z_s, \vec{\Omega})}{4\pi D_\ell^2(z_\ell, \vec{\Omega})}, \quad (4.11)$$

where

$$\frac{dV_c}{dz_\ell}(z_\ell, \vec{\Omega}) = \frac{4\pi c}{H_0} \frac{(1 + z_\ell)^2 D_\ell^2(z_\ell, \vec{\Omega})}{E(z_\ell, \vec{\Omega})} \quad (4.12)$$

is the differential comoving volume and

$$\frac{dN_\ell}{dV_c d\sigma}(z_\ell, \sigma, \vec{\Omega}) = n_c(z_\ell, \vec{\Omega}) p_\sigma(\sigma, z_\ell) \quad (4.13)$$

is the comoving number density of lenses with velocity dispersion σ at redshift z_ℓ . Here, $p_\sigma(\sigma, z_\ell)$ is the probability density of the dispersion velocity of the lenses at a redshift z_ℓ and $n_c(z_\ell)$ is the comoving number density of lenses at z_ℓ . In Equation 4.12, $E(z_\ell, \vec{\Omega}) = \sqrt{\Omega_M[(1 + z_\ell)^3 - 1] + 1}$ assuming a flat Λ CDM cosmology with radiation density parameter, $\Omega_r = 0$.

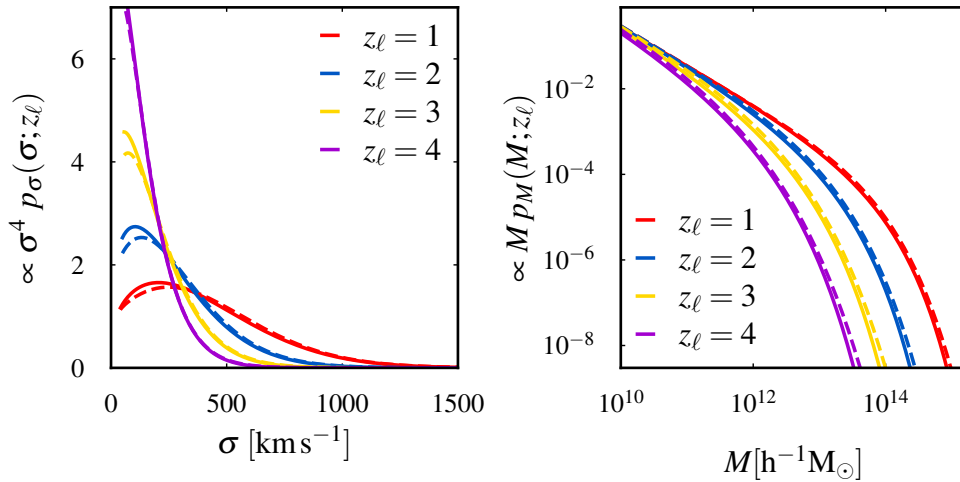


Figure 4.2: The left panel shows the distribution of lens velocity dispersions along the line of sight evaluated at different redshifts for two different halo mass models, “Behroozi” [93] (solid lines) and “Jenkins” [94] (dashed lines). The right panel shows the corresponding mass functions.

In order to compute the distribution of lenses at a given redshift, we need to use some models of structure formation.

$$\frac{dN_\ell}{dV_c d\sigma}(z_\ell, \sigma, \vec{\Omega}) = \frac{dN_\ell}{dV_c dM}(z_\ell, M, \vec{\Omega}) \times \frac{dM}{d\sigma}, \quad (4.14)$$

where the first term denotes the comoving number density of DM halos with mass M at redshift z_ℓ predicted by the cosmological model with parameters $\vec{\Omega}$. We consider several models of the HMF calibrated to cosmological simulations. The second term is a Jacobian to convert the distribution of the halo mass to that of the dispersion velocity. To compute the Jacobian, we assume that the halos are spherically symmetric and virialised, with uniform density ρ and radius R . Thus,

$$\sigma \simeq \sqrt{\frac{GM}{R}}, \quad M = \frac{4}{3}\pi R^3 \rho \quad \Rightarrow \quad \frac{dM}{d\sigma} = \frac{3M}{\sigma}. \quad (4.15)$$

We also need to use some minimum and maximum cutoff for σ to compute the total optical depth defined in Equation 4.10. The natural choices are $\sigma_{\min} = \sigma(M_{\min})$ and $\sigma_{\max} = \sigma(M_{\max})$. We assume $M_{\min} = 10^{10} M_\odot$ and $M_{\max} \simeq 10^{15} M_\odot$, since this the mass range of validity of most of the HMF models that we use. Figure 4.2 plots velocity-dispersion distributions for two different HMF models at different redshifts. Notice the non-trivial difference between the distributions pertaining to the different halo mass models. Such differences could potentially lead to biases in the estimation of $\vec{\Omega}$, if the true halo-mass model is not known. See the Section 4.5 for an illustration of such systematic errors.

Now combining all these pieces together we obtain (not showing the dependence on $\vec{\Omega}$ to simplify the notation)

$$\frac{d\tau}{dz_\ell d\sigma} = \frac{16\pi^3}{E(z_\ell)} \frac{c}{H_0} \left(\frac{\sigma}{c}\right)^4 [D_{\Delta t}(z_\ell, z_s)]^2 \left(\frac{D_{\ell s}}{D_s}\right)^4 p_\sigma(\sigma, z_\ell) n^c(z_\ell). \quad (4.16)$$

It is now easy to see from Equation 4.11 why the cosmological parameters affect the lensing optical depth and hence the number of detected lensed events. The first term describes a purely geometrical effect of how the comoving volume at a given redshift varies with a change in cosmological parameters. The second term describes the change in the distribution of lenses due to changes in the structure formation. Third shows how the fractional area covered by lenses at a given redshift varies due to the geometric effect.

4.3.2 Expected distribution of lensing time delays:

In the SIS lens model, the time delay between the two images is given by (see, e.g. [166]):

$$\Delta t(z_\ell, \sigma, z_s, y, \vec{\Omega}) = \frac{D_{\Delta t}}{c} 32\pi^2 \left(\frac{\sigma}{c}\right)^4 y \left(\frac{D_{\ell s}}{D_s}\right)^2. \quad (4.17)$$

where y is the projected location of the source on the lens plane (in units of r_E). We compute the expected time delay distribution $p(\Delta t | \vec{\Omega})$ for different values of the cosmological parameters $\vec{\Omega}$ by marginalising the distribution of time delay over all other parameters $\vec{\lambda} \equiv \{y, \sigma, z_\ell, z_s\}$ on which the time delay depends.

$$p(\Delta t | \vec{\Omega}) = \int p(\Delta t | \vec{\lambda}, \vec{\Omega}) p(\vec{\lambda} | \vec{\Omega}) d\vec{\lambda}, \quad (4.18)$$

where $p(\vec{\lambda} | \vec{\Omega})$ denotes the expected distribution of the source position y , lens velocity dispersion σ , lens redshift z_ℓ and source redshift z_s , given the set of cosmological parameters $\vec{\Omega}$. If we assume isotropy of space, the distribution of y is independent of the cosmological parameters. Hence

$$p(\vec{\lambda} | \vec{\Omega}) = p(y) p(\sigma, z_\ell, z_s | \vec{\Omega}). \quad (4.19)$$

Here, all distributions are conditioned on strong lensing, where $p(y) \propto y$ with $y = (0, 1]$. Above, $p(z_\ell, \sigma, z_s | \vec{\Omega})$ can be further split as

$$p(\sigma, z_\ell, z_s | \vec{\Omega}) = p(\sigma, z_\ell | z_s, \vec{\Omega}) p_b(z_s | \vec{\Omega}), \quad (4.20)$$

where $p_b(z_s | \vec{\Omega})$ is the expected/measured distribution of source redshifts, while $p(\sigma, z_\ell | z_s, \vec{\Omega})$ is computed from the differential optical depth (Equation 4.11)

$$p(\sigma, z_\ell | z_s, \vec{\Omega}) \propto \frac{d\tau}{dz_\ell d\sigma}(z_s, \vec{\Omega}). \quad (4.21)$$

Figure 4.3 illustrates the imprint of cosmology on the number of lensed events observable for a period of ten years as well as the distribution of time delays. The time delay distribution and the number of lensed events are governed by two primary factors. First, the geometry of the universe, which affects the relation between redshift and distance measures. Second, lens properties: their number density, velocity dispersion distribution, and redshift evolution. All these quantities depend on cosmological parameters, and their combined influence determines how both the time delay distribution and the total number of lensed events vary with different values of cosmological parameters. The number of lensed events increase with increasing H_0 and Ω_m . The peak of the distribution shifts towards smaller time-delay values with increasing H_0 , and towards larger values with increasing Ω_m . While these cosmological effects on the time delay distribution may appear subtle, the Bayesian approach effectively captures these imprints to achieve $\mathcal{O}(1\%)$ constraints. Here we assume a BBH merger rate of $R = 5 \times 10^5 \text{ yr}^{-1}$ with an observation period of $T_{\text{obs}} = 10 \text{ yrs}$. The redshift distribution of BBH mergers follows the population model from [165], while the lens distributions are derived using the HMF from [93].

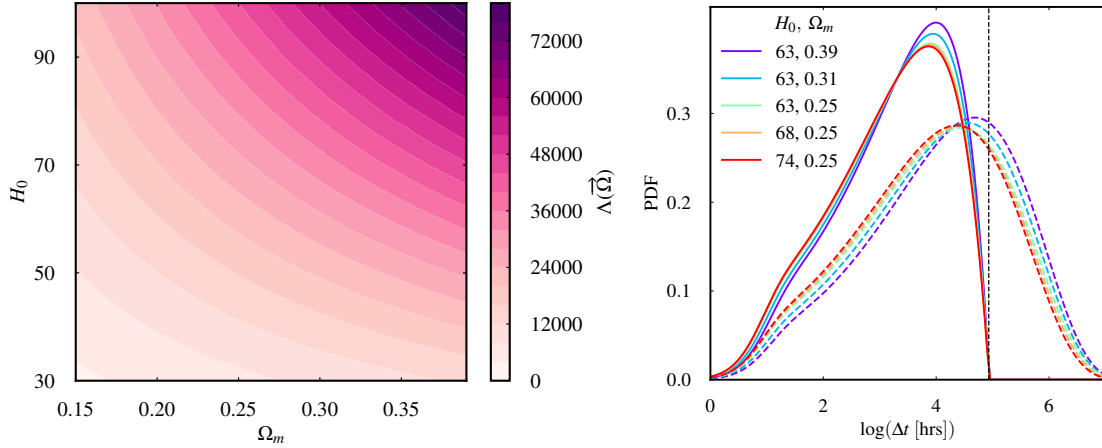


Figure 4.3: *Left*: Expected number of lens pairs for different values of $\vec{\Omega}$ in flat Λ CDM model, assuming a detection rate $R = 5 \times 10^5 \text{ yr}^{-1}$ and observation time period $T_{\text{obs}} = 10 \text{ yrs}$. *Right*: The strong-lensing time-delay distributions for different values of cosmological parameters: Increasing H_0 (Ω_m) shifts the peak of the distribution towards smaller (larger) time-delay values. Dashed lines show the actual distributions $p(\Delta t | \vec{\Omega})$ while the solid lines show the distribution of time delays observable in a period of 10 yrs.

4.4 Expected constraints on cosmological parameters

To assess the ability of our method to constrain cosmological parameters, we choose a “true” cosmology $\vec{\Omega}_{\text{true}} = \{H_0 = 67.3, \Omega_m = 0.316\}$. We further assume that the “true” halo mass model is described by [167], as implemented in the HMFALC package [95], and the “true” source distribution is given by [168]⁵. We assume a total observing period $T_{\text{obs}} = 10 \text{ yrs}$ and a BBH merger rate $R = 5 \times 10^5 \text{ yr}^{-1}$. We neglect the selection effects in the detection as 3G detectors are expected to detect all the BBHs out to large distances ($d_L \sim 1000 \text{ Gpc}$). We compute the expected number Λ of lensed events making use of Equation 5.14. To simulate one observational scenario where N events are detected, we draw one sample from a Poisson distribution with mean Λ . Further, we draw samples $\{\Delta t_i\}_{i=1}^N$ from $p(\Delta t | \vec{\Omega}_{\text{true}}, T_{\text{obs}})$ (see Equation 5.13).

Using N and $\{\Delta t_i\}_{i=1}^N$, we evaluate the posterior described in Equation 4.1 for different values of $\vec{\Omega}$. We assume uniform priors on H_0 and Ω_m , so that the final posterior is given by the product of the likelihoods $p(N | \vec{\Omega}, T_{\text{obs}})$ and $p(\Delta t_i | \vec{\Omega}, T_{\text{obs}})$. Figure 4.4 shows these two likelihoods as well as the posterior on H_0 and Ω_m obtained

⁵Dominik et al. (2013) predicts BBH merger rate densities by using the StarTrack population synthesis code [169, 170] to model the complete evolution of isolated binary stars from the Zero Age Main Sequence through mass transfer episodes to compact object formation and final merger. Their analysis incorporates an initial mass function adopted from Kroupa et. al. (1993 & 2003) [171, 172], assumes a flat logarithmic distribution for initial binary separations, and adopts the cosmic star formation rate history from Strolger et. al. (2004) [173]. The resulting merger rates as a function of redshift are strongly influenced by metallicity-dependent stellar evolution, common envelope efficiency parameters, and supernova kick physics, with these factors determining how the merger rate density evolves across cosmic time.

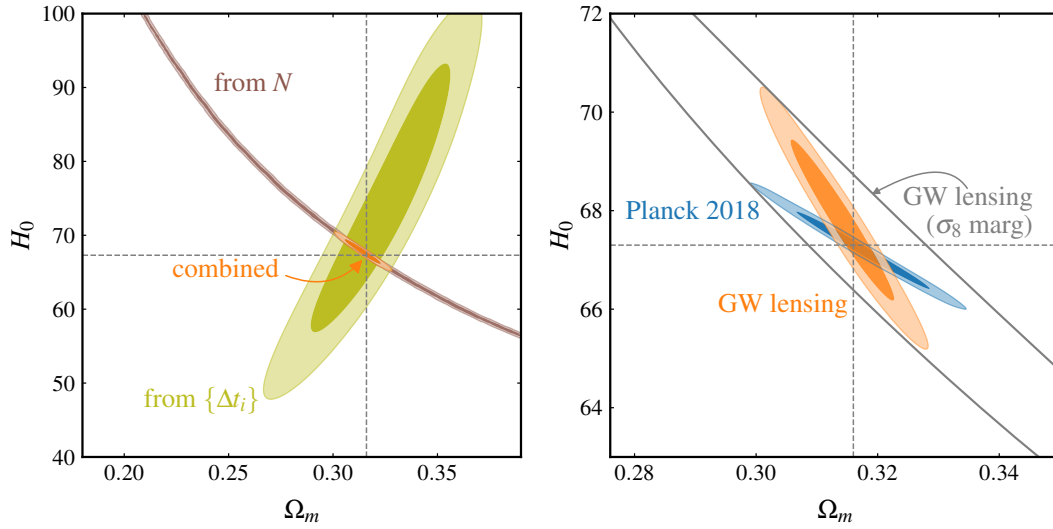


Figure 4.4: *Left panel*: Expected posterior distributions (68% and 95% credible regions) of H_0 and Ω_m computed from the time delay distribution and the number of lensed events separately, along with the combined posterior (shown in orange). We assume a BBH merger rate $R = 5 \times 10^5 \text{ yr}^{-1}$ and total observation time period $T_{\text{obs}} = 10 \text{ yrs}$. The “true” cosmology (dashed cross-hairs) is recovered within the 68% credible interval (orange shade), with $H_0 = 67.8 \pm 1.1 \text{ km s}^{-1} \text{ Mpc}^{-1}$ and $\Omega_m = 0.3142 \pm 0.0056$. *Right panel*: A comparison of the the combined posterior obtained from GW lensing with the same obtained from CMB observations by Planck. While the orange contours assume that the σ_8 parameter is well-measured from other observations, the grey contour corresponds to 95% credible region of the posterior marginalized over σ_8 parameter.

from combining these two likelihoods. We find that the posteriors are centred around the true values of cosmological parameters. Further, the constraints on $\vec{\Omega}$ are found to be $H_0 = 67.8 \pm 1.1$ and $\Omega_m = 0.314 \pm 0.006$ (68% credible intervals of marginalised posteriors). These constraints are comparable to those derived from the CMB [106]⁶. Additionally, they probe a very different redshift regime ($z \sim 10$ as compared to $z \sim 1000$ probed by the CMB) and have different systematics.

While we have assumed a BBH detection rate of $R = 5 \times 10^5 \text{ yr}^{-1}$, the actual detection rate is uncertain as of now. Hence we repeat these calculations assuming a more moderate detection rate of $R = 5 \times 10^4 \text{ yr}^{-1}$ and a pessimistic rate of $R = 2.5 \times 10^4 \text{ yr}^{-1}$. This will, in turn reduce the observed number of lensed events over the observational period of $T_{\text{obs}} = 10 \text{ yrs}$. The expected posteriors on cosmological parameters assuming the three different merger rates is shown in Figure 4.5. As expected, a smaller merger rate (resulting in a smaller number of lensed events) increases the width of the posteriors, although the true cosmology continues to be recovered within

⁶Note that we have set all other parameters of the Λ CDM model to the best fits values provided by [106]. In order to make a fair comparison, we do the same for the Planck posteriors as well. However, the uncertainty in some of the other parameters, in particular σ_8 , will have an imprint on the precision with which H_0 and Ω_m could be constrained. Therefore, in addition, we show the posteriors that are marginalized over σ_8 as well in Figure 4.4. The marginalized constraints are significantly worse, so we need a complimentary probe to achieve better constraining power.

the 68% credible interval.

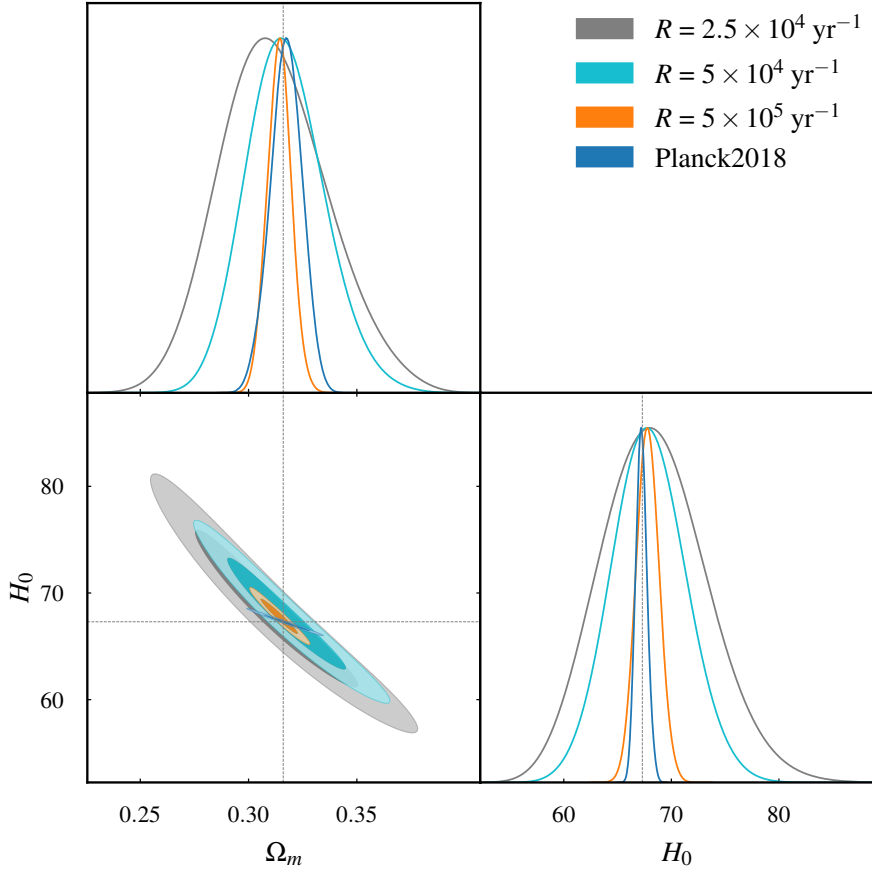


Figure 4.5: Expected posterior distributions of H_0 and Ω_m from a 10-year observation period, assuming different values for the merger rate R (shown in the legend). A lower merger rate (producing a smaller number of lensed events) will result in less precise estimates of the cosmological parameters.

We also illustrate the ability of this method to constrain parameters of some more general cosmological models. In particular, we consider w CDM model [106] with two parameters $\vec{\Omega} = \{\Omega_m, w_0\}$. In this part, we fix the Hubble constant H_0 to its “true” value, mimicking a situation where it will be well measured from low-redshift observations. As done earlier, we compute the expected number of lensed events and model time delay distributions using Equations 5.14 and 5.13. We choose a “true” cosmology $\vec{\Omega}_{\text{true}} = \{\Omega_m = 0.203, w_0 = -1.55\}$. We assume a halo mass model described in [167] and the source distribution given in [168]. Now considering a BBH merger rate $R = 5 \times 10^5 \text{ yr}^{-1}$ and total observing time period $T_{\text{obs}} = 10 \text{ yrs}$, we draw one value of N and one set of $\{\Delta t_i\}_{i=1}^N$ from $p(N | \vec{\Omega}_{\text{true}}, T_{\text{obs}})$ and $p(\Delta t | \vec{\Omega}_{\text{true}}, T_{\text{obs}})$. From these simulated observation data we evaluate the posteriors on these Ω_m and w_0 (see Figure 4.6). The expected constraints from GW lensing ($w_0 = -1.52^{+0.16}_{-0.12}$ and $\Omega_m = 0.203 \pm 0.001$) compare favorably to those obtained from Planck ($w_0 = -1.55^{+0.18}_{-0.33}$ and $\Omega_m = 0.203^{+0.018}_{-0.058}$), albeit with the caveat that we are exploring only a subset of parameters.

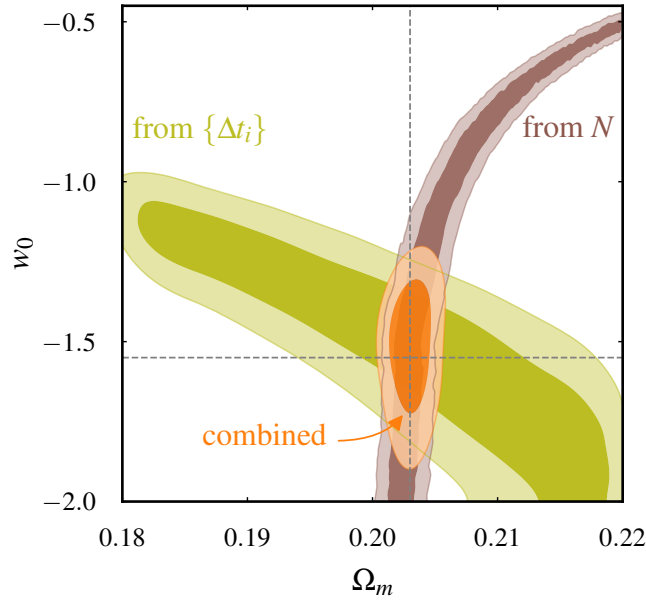


Figure 4.6: Expected posterior distributions (68% and 95% credible regions) of Ω_m and w_0 of the w CDM model computed from the time delay distribution and the number of lensed events (jointly). We assume a BBH merger rate $R = 5 \times 10^5 \text{ yr}^{-1}$ and total observation time period $T_{\text{obs}} = 10 \text{ yrs}$. The “true” cosmology (dashed cross-hairs) is recovered within the 68% credible interval (orange shade), with $w_0 = -1.52^{+0.16}_{-0.12}$ and $\Omega_m = 0.203 \pm 0.001$.

4.5 Cosmography systematics

In this section, we investigate various systematic effects that influence the precision of cosmological parameter measurements using the Bayesian framework delineated in Section 4.2. We have seen in Section 4.3 that, the essential ingredients for modelling the expected number of lensed events and their time delay distribution are:

- *The redshift distribution of GW sources:* We expect that this can be measured with sufficient precision from the large number $\sim 10^6$ of unlensed events that will dominate the data (see, e.g., [161]). In Section 4.5.1 we forecast the prospective constraints on cosmological parameters assuming various theoretical models of the source redshift distribution (Figure 4.7). In Section 4.5.2 we study how uncertainties and errors in inferring the source redshift distribution can affect the constraints on cosmological parameters (Figure 4.8).
- *A HMF model:* This will need input from cosmological simulations. We show in Section 4.5.3 that a wrong choice of the HMF model can bias our inference of cosmological parameters. However, if the right HMF model is one among the many models that we consider, Bayesian model selection can be used to identify the right model.

We maintain the same assumptions used in our previous analyses. The key assump-

tions are as follows: we adopt halo mass limits of $M_{\min} = 10^8 M_{\odot}$ and $M_{\max} \simeq 10^{15} M_{\odot}$, which are essential for evaluating Equation 4.10. To investigate systematic effects arising from the lens distribution, we employ several HMFs in addition to the Behroozi model [93], enabling us to assess potential biases in cosmological parameter estimation. For analyzing effects related to the source distribution, we consider multiple theoretical source redshift distributions beyond the model presented in the previous section.

Here we show that the precision of the estimation of the cosmological parameters does not have a strong dependence on the assumed BBH redshift distribution model. Using the large number of unlensed mergers, XG detectors are expected to measure the BBH redshift distribution with sufficient precision for the cosmological inference. However, a biased inference of the BBH redshift distribution will bias the estimation of cosmological parameters. An incorrect model for the distribution of lens properties can also lead to a biased cosmological inference. However, Bayesian model selection can assist in selecting the right model from a set of available parametric models for the lens distribution. We also present a way to incorporate the effect of contamination in the data due to the limited efficiency of lensing identification methods, so that it will not bias the cosmological inference.

4.5.1 Effect of source distribution models

The redshift distribution of sources is a significant input for our method. The precision of estimation of cosmological parameters depends on the redshift distribution of sources because lensing optical depth increases with redshift (Equation 4.10). To examine how the source population affects the precision in estimating the cosmological parameters, we conduct a recovery test similar to the one done in [57]. We examine various models for the redshift distribution of mergers, including those predicted by population synthesis models such as [118, 165, 174], as well as a model in which the merger rate is uniform in comoving volume. Additionally, we explore merger distribution models obtained from a star formation rate given in [175] using different delay time distributions as presented in [161]. We consider two different models for the distribution of time delays between the formation of the binary and its merger: an exponential distribution with a characteristic time scale $\tau = 0.1$ Gyr and a distribution uniform in logarithmic of time delay (see Equations 6 and 7 of [161]). Apart from these two models, we also consider the scenario where there is no time delay between formation and merger, which implies that black hole mergers follow the same redshift distribution as the star formation rate.

The left panel of Figure 4.7 displays the redshift distributions of BBH mergers which we consider. We consider a “true” cosmology $\vec{\Omega}_{\text{true}} = \{\Omega_m = 0.316, H_0 = 67.3\}$. The true distributions of lens redshift and parameters are calculated using a HMF model as described by [93], implemented in HMFALC package [176] as described in Section 4.3. We assume a merger rate of $R = 5 \times 10^5 \text{ yr}^{-1}$ for BBHs, with an observation time period $T_{\text{obs}} = 10$ yrs.

To simulate one observational scenario where N lensed events with time delays $\{\Delta t_i\}_{i=1}^{i=N}$ are detected, we draw one sample from a Poisson distribution with mean

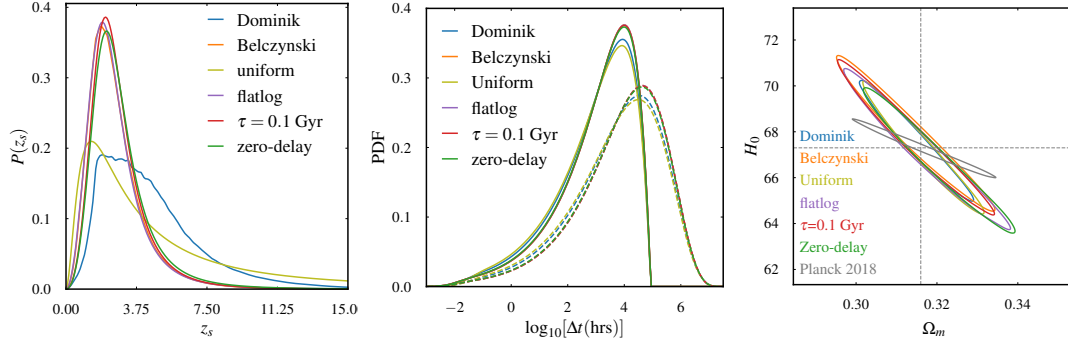


Figure 4.7: *Left*: Different models for the distributions of redshifts for BBH mergers. These include prediction from population synthesis studies by Dominik [165] and Belczynski [118, 174], as well as uniform in comoving volume. Other models are based on Madau-Dickinson star formation rate [175] and consider different distributions of the time delay between formation and merger. *Middle*: The distributions of time delay between two lensed images of a source for different models of redshift distribution of BBH mergers shown in the left panel. Dashed lines represent the actual time delay distributions $p(\Delta t | \vec{\Omega})$ while solid lines represent time delay distributions $p(\Delta t | \vec{\Omega}, T_{\text{obs}})$ that will be observable in 10 yrs. Time delay distributions are calculated for $\vec{\Omega} = \{\Omega_m = 0.316, H_0 = 67.3\}$. *Right*: Posteriors (95% credible region) on cosmological parameters (Ω_m, H_0) for different models of redshift distributions. This is done considering a BBH merger rate of $5 \times 10^5 \text{ yr}^{-1}$ with observation time period of 10 yrs. Dashed cross represents true cosmological parameters.

$\Lambda(\vec{\Omega}_{\text{true}}, T_{\text{obs}} = 10 \text{ yr})$ and then draw samples $\{\Delta t_i\}_{i=1}^{i=N}$ from $p(\Delta t | \vec{\Omega}_{\text{true}}, T_{\text{obs}} = 10 \text{ yrs})$. We neglect the selection effects of XG detectors, as XG detectors are expected to detect all the BBHs out to very high redshifts. Time delay distributions considering different models of redshift distribution for BBH mergers are shown in the middle panel of Figure 4.7 (for $\vec{\Omega} = \vec{\Omega}_{\text{true}}$).

	Dominik	Belczynski	Uniform	flatlog	$\tau = 0.1\text{Gyr}$	zero-delay
$\Lambda(\Omega_{\text{true}})$	37700	20594	36698	20448	22098	23433
$\Omega_m(68\%)$	$0.315^{+0.006}_{-0.006}$	$0.314^{+0.007}_{-0.008}$	$0.316^{+0.006}_{-0.006}$	$0.317^{+0.008}_{-0.009}$	$0.314^{+0.008}_{-0.008}$	$0.320^{+0.007}_{-0.008}$
$\Omega_m(95\%)$	$0.315^{+0.012}_{-0.011}$	$0.314^{+0.016}_{-0.015}$	$0.316^{+0.012}_{-0.012}$	$0.317^{+0.017}_{-0.016}$	$0.314^{+0.016}_{-0.015}$	$0.320^{+0.016}_{-0.014}$
$H_0(68\%)$	$67.6^{+1.1}_{-1.1}$	$67.9^{+1.4}_{-1.4}$	$67.2^{+1.2}_{-1.2}$	$67.2^{+1.4}_{-1.4}$	$67.7^{+1.4}_{-1.4}$	$66.7^{+1.3}_{-1.3}$
$H_0(95\%)$	$67.6^{+2.1}_{-2.0}$	$67.9^{+2.7}_{-2.7}$	$67.2^{+2.4}_{-2.3}$	$67.2^{+2.9}_{-2.7}$	$67.7^{+2.7}_{-2.6}$	$66.7^{+2.5}_{-2.5}$

Table 4.1: Expected number of lensed events Λ for $\vec{\Omega} = \vec{\Omega}_{\text{true}}$ and expected constraints (68% and 95% credible intervals) on Ω_m and H_0 for different models of redshift distribution of BBH mergers considering a merger rate of $5 \times 10^5 \text{ yr}^{-1}$ with an observation time of 10 yrs.

Using the method outlined in Section 4.2, we compute the posteriors on the cosmological parameters $\vec{\Omega}$ from the different observing scenarios corresponding to the different source redshift distributions. We also assume that the redshift distribution of the sources is measured with sufficient precision from the observation of unlensed

events. Posteriors for the cosmological parameters are shown in the right panel of Figure 4.7. When the source populations extend to high redshift (e.g., Dominik, Uniform), the precision is better in comparison to populations where the merger redshift does not have support at high redshift (e.g., Belczynski, flatlog, etc.). This is because the lensing optical depth increases with redshift, and therefore, populations that extend to high redshift are expected to have a larger number of lensed events than the populations that do not extend to high redshift. The expected 95% credible intervals in the posteriors of the cosmological parameters are summarised in Table 4.1, for different source redshift distribution models.

4.5.2 Effect of errors in measuring the source redshift distribution

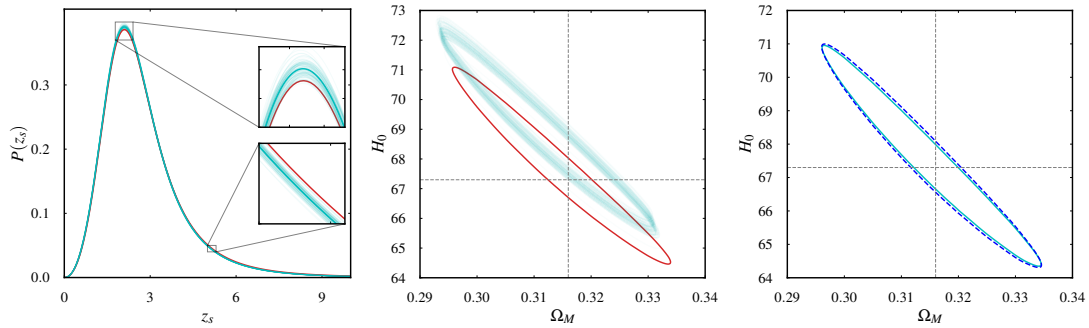


Figure 4.8: *Left panel:* The red curve shows the redshift distribution model based on the Madau-Dickinson star formation rate, with an exponential delay-time distribution with $\tau = 0.1$ Gyr. Light cyan curves show the reconstructed (posterior predictive) distributions as shown in Figure 5 of [161], while the solid cyan curve shows their average. *Middle Panel:* The 95% credible regions of the posteriors of Ω_m and H_0 . The lensed events are simulated using the red curve in the left panel. The cosmological inference is done with the ‘true’ redshift distribution (red contour), as well as with 100 reconstructed source redshift distributions (light cyan contours, corresponding to the light cyan curves in the left panel). The cyan posteriors are biased due to the biased reconstruction of the source redshift distribution. *Right Panel:* This panel shows the effect of the marginalisation over the source redshift distribution uncertainties. Here, the lensed events are simulated using the solid cyan curve in the left panel, so that there is no systematic bias. The solid cyan contour shows the posterior estimated using the same redshift distribution. The dashed blue contour shows the posterior that is marginalised over the source redshift distribution uncertainties. The broadening of the posterior due to this effect is minimal.

In Section 4.5.1, we assumed that the true redshift distribution of the sources is accurately known from the observation of unlensed events. However, this is not an entirely valid assumption as uncertainties and errors in the measurement of luminosity distance could bias our estimation of the redshift distribution, leading to systematic errors as well as additional statistical uncertainties in the estimation of cosmological parameters. Here we investigate the severeness of this effect.

Combining the inferred luminosity distance posteriors from a number of BBH events

and assuming a cosmology, we will be able to reconstruct the redshift distribution of BBH mergers in the universe. This can be done either using a parametric model of the population properties of BBHs (such as their mass and redshift distribution) or using non-parametric methods [177]. The errors in the reconstruction of the redshift distribution of BBH mergers using XG detectors were studied in [161], using a parametric model. We use the results of their study for characterising the corresponding errors in cosmological inference. As done in [161], we use a ‘true’ redshift distribution given by a model based on Madau-Dickinson star formation rate and exponential delay time distribution with a time scale, $\tau = 0.1$ Gyr (red curves in Figures 4.7 and 4.8).

We use the posterior predictive distributions of the merger rate density from [161], which was derived from the posteriors on the parameters of the redshift distribution model (Figures 4 and 5 of [161]). We take ~ 100 samples of the merger rate density distributions and convert them into source redshift distributions. In the left panel of Figure 4.8, the light cyan curves represent these posterior predictive distributions while the solid cyan curve shows their average. These reflect the uncertainties in the measurement of the redshift distribution, while the red curve shows the ‘true’ distribution.

Now we simulate lensed events using the ‘true’ redshift distribution and infer cosmological parameters using different posterior predictive redshift distributions (corresponding to different light cyan lines in the left panel of Figure 4.8). The middle panel of Figure 4.8 shows the posteriors of the cosmological parameters inferred using the ‘true’ redshift distribution (red line) and 100 sampled redshift distributions (thin cyan lines). It is evident that there is a systematic bias in the recovery, which is attributed to the biased reconstruction of the merger rate density as seen in the left panel of Figure 4.8.

We also explore a scenario in which the redshift distribution of BBHs is estimated without any systematic biases, but with some statistical uncertainty. In order to simulate such a scenario, we use the average of 100 sampled redshift distributions as the ‘true’ distribution (cyan curve in the left panel of figure 4.8). We then use this ‘true’ distribution to simulate lensed events and to infer cosmological parameters (right panel of figure 4.8). Here, the solid cyan contour represents the posterior (95% credible region) of cosmological parameters using the new ‘true’ redshift distribution, showing no systematic bias. When we factor in the uncertainties in the estimation of source redshift distribution making use of the posterior predictive distributions (light cyan curves in the left panel of 4.8), the posteriors of the cosmological parameters will have a scatter similar to the light cyan curves in the middle panel of Figure 4.8. The dashed dark blue contour shows the posterior that is marginalised over the uncertainties in the estimation of the source redshift distribution. We can see that the broadening of the posterior is minimal.

In summary, the expected statistical uncertainties in the estimation of the source redshift distribution have a negligible effect on cosmological inference. However, the redshift distribution needs to be estimated without any systematic bias. In this preliminary investigation, we have neglected the correlation of the parameters of the source

distribution model with the cosmological parameters. We anticipate that this oversight will not significantly broaden the posteriors on cosmological parameters, as the expected measurement error on the merger rate density is small [161]. Our future plans include conducting a comprehensive analysis that considers all the parameters of the source redshift distribution along with the cosmological parameters and marginalising over them.

4.5.3 Effect of lens distribution

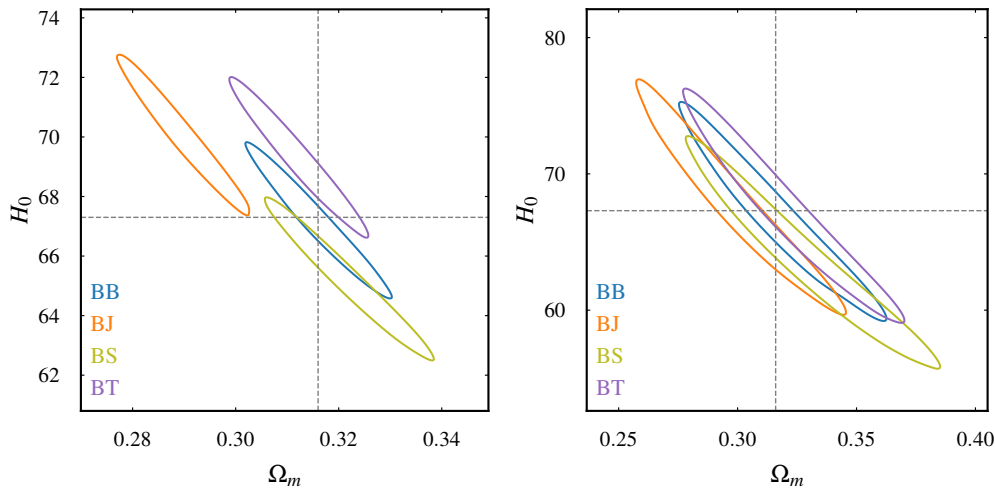


Figure 4.9: Posteriors (95% credible regions) of cosmological parameters that illustrate the bias in the inference due to the use of wrong models of the HMF. In the legends, BB, BJ, BS and BT denote different scenarios when our simulated observation of lensed signals is produced using Behroozi model, and then cosmological parameters are recovered using Behroozi, Jenkins, SMT and Tinker08 models, respectively. *Left panel:* Results corresponding to a merger rate $5 \times 10^5 \text{ yr}^{-1}$. We can see that true cosmology is not recovered within 95% credible region except for the case of BB. However, the precision for all cases remains almost the same. *Right panel:* Results corresponding to a merger rate $5 \times 10^4 \text{ yr}^{-1}$. Here, we can see that the amount of bias is relatively small due to the decreased precision of the cosmological parameters.

The distribution of the redshift and other parameters of the lenses are determined using the HMF models (see Section 4.3). Here we investigate how selecting the incorrect model for the lens distribution (both redshift and other parameters) can affect the inference of cosmological parameters. We broadly follow the same steps as outlined in Section 4.5.1. However, here we assume the redshift distribution given by Dominik [165] to be the one presented by nature, and we will vary the lens distribution while keeping the other parameters fixed. We consider four different models of HMF, namely Behroozi [93], Jenkins [94], SMT [178], and Tinker08 [179]. We simulate N lensed events with time delays $\{\Delta t_i\}_{i=1}^N$ using the Behroozi model. N is drawn from a Poisson distribution with mean $\Lambda(\bar{\Omega}_{\text{true}}, T_{\text{obs}})$, where $\bar{\Omega}_{\text{true}}$ is the assumed “true” value of cosmological parameters. This is our simulated observational data. We then estimate the cosmological

parameters using all of these HMF models.

We observe that there is a bias in the inference of cosmological parameters when we choose the wrong model of lens distribution. The bias appears in both the posterior distributions derived from number of lensed events and the time delay distribution. As a result, the combined inference becomes biased. Figure 4.9 shows an example set of posteriors (95% credible regions) on the cosmological parameters when different HMF models are used in the parameter estimation. The left (right) panel shows results corresponding to an assumed merger rate $R = 5 \times 10^5 \text{ yr}^{-1}$ ($5 \times 10^4 \text{ yr}^{-1}$) for an observation time of 10 yrs. In the left panel the true cosmology is not recovered within 95% credible region except when the true HMF is used in the parameter estimation, while the amount of bias is relatively small in the right panel due to the decreased precision.

The posteriors in Figure 4.9 show one realisation of the observation scenario. Each of the posterior could be randomly shifted due to the finite number of observed events (Poisson fluctuations). To get the statistical nature of the biases, we perform this analysis using $\sim 10^3$ catalogs of observations of same statistical nature. The so-called probability-probability (p-p) plots show in what fraction of the simulated observations, the true values are recovered within a given credible interval (Figure 4.10). If the theoretical models agree with the data, the p-p plot should show a diagonal line. We see that diagonal p-p plots are obtained only when the simulated HMF model is used in the parameter estimation.

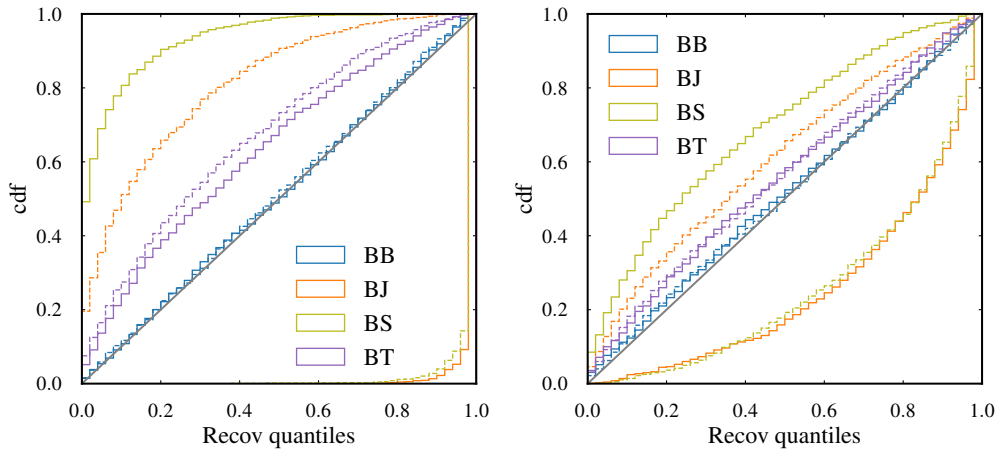


Figure 4.10: The cumulative distribution of the quantiles (p-p plots) in which the true cosmological parameters are recovered from $\sim 10^3$ recovery tests. The legend box shows the scenarios considered (same as Figure 4.9). Any deviation from the diagonal line suggest there is a bias in the recovery. The larger the deviation, the greater is the bias in the inference. Solid (dashed) lines show the recovery for Ω_m (H_0). In the left panel, the results corresponding to a merger rate of $5 \times 10^5 \text{ yr}^{-1}$ show that there are biases, except in the BB scenario. In the right panel, the results for a merger rate of $5 \times 10^4 \text{ yr}^{-1}$ indicate that there is relatively lower bias due to the decreased precision in the estimation of the cosmological parameters.

While this is a cause of concern, we show below that Bayesian model selection generally allows us to identify the correct model of the HMF. We compute the ratios of Bayesian evidences (Equation 4.2) of different HMF models and show that the right HMF model is almost always preferred. We simulate lensed events with time delays using model B (Behroozi) and then recover the cosmological parameters using all these models. We observe that for the model that consistently shows bias in its parameter estimates, the evidence is smaller than the “true” model. The ratio of the evidences (the Bayes factor) between the true and false models is greater than one for most of the simulations. For instance, in the parameter estimation using the J (Jenkins) model typically causes large bias in the estimated parameters (see Figure 4.9). However, the Bayes factor between B and J models is higher than one over $\sim 80\%$ of the time, indicating that the true model is generally preferred (Figure 4.11). In the parameter estimation using the T (Tinker) model, the true model is preferred only for $\sim 50\%$ of the time; however, the bias in the estimated parameters using the T model is generally smaller.

In order for this model selection to work, the space of models that we consider should include the true model also. A more powerful method would be to create parametrised models of the HMF that also incorporate modelling errors as extra parameters. These could be treated as nuisance parameters in the cosmological parameter estimation and marginalised over. A combination of EM observations and cosmological simulations can be used to further improve our models of the distribution of lens properties.

There are similarity transformation degeneracies that prevent us from reconstructing the lens mass and redshift simultaneously from a single event [68, 69, 180, 181]. This is why the GW observations of individual lensed events, in the absence of EM observations, will not enable any measurement of cosmological parameters [182]. However, this doesn’t affect our method in a serious way, since we assume the knowledge of the distribution of the lens properties in the form of a HMF. Even if we don’t know the “true” HMF, if the true HMF is in the list of models that we use, it will have the highest Bayes factor statistically. The reason is that the change in the time delay distribution due to a different HMF model cannot be exactly mimicked by a change in cosmology, i.e., the degeneracy between cosmology and HMF is not an exact one.

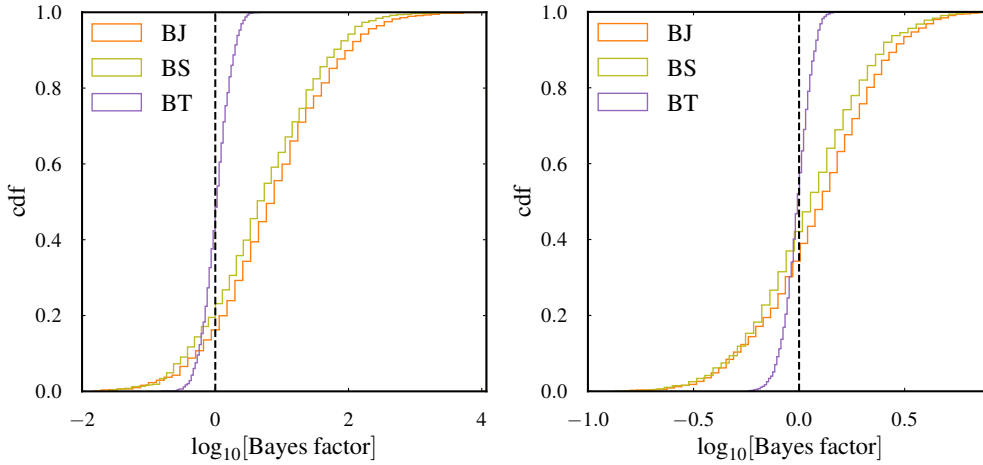


Figure 4.11: The cumulative distribution of \log_{10} (Bayes factor) between the “right” (B) and “wrong” (J, S or T) HMF models, computed from $\sim 10^3$ simulated catalogs. The results correspond to merger rates of $5 \times 10^5 \text{ yr}^{-1}$ (left) and $5 \times 10^4 \text{ yr}^{-1}$ (right). We can see that HMF models that cause significant bias in the parameter estimation have low Bayes factors most of the time.

4.5.4 Effect of contamination

Any data analysis method that is used to identify strongly lensed signals in GW data will have a true positive probability ϵ and a false positive probability α (see, e.g., [140, 183, 184]). This means that some unlensed GW signals will be incorrectly identified as lensed signals and some lensed signals will be missed, thus biasing the detected number of lensed events and their time delay distribution. In this section we develop a strategy that can incorporate this effect, thus evading systematic biases in the estimation of cosmological parameters.

We assume that the total number N_{tot} of detected BBH mergers observed follows a Poisson distribution of mean Λ_{tot} while the detected number of strongly lensed mergers N follows a Poisson distribution of mean Λ . We define the contamination fraction κ as the ratio between the expected number of falsely identified lensed pairs and the number of truly identified lensed pairs

$$\kappa \simeq \frac{\alpha \Lambda_{\text{tot}}^2}{2 \epsilon u \Lambda_{\text{tot}}} = \frac{\alpha \Lambda_{\text{tot}}}{\epsilon 2u}, \quad (4.22)$$

where $u \equiv \Lambda / \Lambda_{\text{tot}}$ is the expected lensing fraction. Note that κ is a function of cosmological parameters and the observing period T_{obs} as the lensing fraction depends on $\vec{\Omega}$ and the total number of observed events depends on T_{obs} . For simplicity of notation, we don’t explicitly write down its dependence on $\vec{\Omega}$ and T_{obs} . The contamination fraction also depends on $k_0 \equiv \alpha / \epsilon$, which depends on the receiver operating characteristic (ROC) of a given lensing identification method. This can be estimated by performing the same analysis on simulated lensed and unlensed GW events (see, e.g. [140]). To keep the contamination fraction low (about 10%), we would need $\alpha \sim 10^{-9}$ for $\epsilon \sim 0.5$, $\Lambda \sim 10^6$

and $u = 0.01$. This is likely to be achievable in future GW observations due to the increased precision of measurements.

It is easy to see that, with a contamination fraction κ , the expected number of lensed events will change to

$$\Lambda_c(\vec{\Omega}, T_{\text{obs}}) = \epsilon [1 + \kappa] \Lambda(\vec{\Omega}, T_{\text{obs}}). \quad (4.23)$$

Thus, once k_0 is known from simulations, it is possible to model the effect of contamination on the expected number of lensed events. Similarly, the time delay distribution of the detected events will be a mixture of the lensed and unlensed time delays. We model the effect of contamination on the time delay distribution as:

$$p_c(\Delta t | \vec{\Omega}, T_{\text{obs}}) = \frac{\kappa}{1 + \kappa} p_{\text{unlens}}(\Delta t | T_{\text{obs}}) + \frac{1}{1 + \kappa} p_{\text{lens}}(\Delta t | \vec{\Omega}, T_{\text{obs}}), \quad (4.24)$$

and use them for the cosmological parameter estimation. Above, $p_{\text{lens}}(\Delta t | \vec{\Omega}, T_{\text{obs}})$ is given by Equation 4.6, while

$$p_{\text{unlens}}(\Delta t | T_{\text{obs}}) \propto (T_{\text{obs}} - \Delta t) \Theta(T_{\text{obs}} - \Delta t). \quad (4.25)$$

To gauge the effect of contamination on the cosmological parameter inference, we simulate lensed events following the Dominick redshift distribution, assuming the true cosmology $\Omega_{\text{true}} = \{\Omega_m = 0.316, H_0 = 67.3\}$, with $R = 5 \times 10^5$ and $T_{\text{obs}} = 10$ yrs. This corresponds to a true expected detection of $\Lambda_{\text{tot}} = 5 \times 10^6$ binaries. We assume that the lensing identification method has a false positive probability of $\alpha = 10^{-9}$. We assume different true positive probabilities: $\epsilon = 0.4, 0.5, 0.6, 0.8$, corresponding to $k_0 \equiv \alpha/\epsilon = [2.5, 2, 1.67, 1.25] \times 10^{-9}$. Figure 4.12 shows the posteriors on the cosmological parameters from an analysis that takes into the effect of contamination. When there is no contamination $k_0 = 0$, we reproduce the results from Figure 4.7. Additionally, data contamination only worsens the precision of our measurement, without causing any systematic biases (see p-p plot in Figure 4.12). Table 4.2 tabulates the expected precision in the measurement of cosmological parameters with different levels of contamination.

	No contamination	$k_0 = 2.5$	$k_0 = 2$	$k_0 = 1.67$	$k_0 = 1.25$
$\Lambda_c(\Omega_{\text{true}})$	37700	27580	31350	35120	42660
$\Omega_m(68\%)$	$0.315^{+0.006}_{-0.006}$	$0.311^{+0.012}_{-0.012}$	$0.317^{+0.011}_{-0.011}$	$0.317^{+0.009}_{-0.009}$	$0.312^{+0.008}_{-0.008}$
$\Omega_m(95\%)$	$0.315^{+0.012}_{-0.011}$	$0.311^{+0.025}_{-0.023}$	$0.317^{+0.022}_{-0.020}$	$0.317^{+0.019}_{-0.018}$	$0.312^{+0.016}_{-0.015}$
$H_0(68\%)$	$67.6^{+1.1}_{-1.1}$	$68.3^{+2.2}_{-2.2}$	$67.3^{+1.8}_{-1.8}$	$67.6^{+1.6}_{-1.6}$	$67.9^{+1.4}_{-1.4}$
$H_0(95\%)$	$67.6^{+2.1}_{-2.0}$	$68.3^{+4.4}_{-4.3}$	$67.3^{+3.7}_{-3.5}$	$67.6^{+3.3}_{-3.1}$	$67.9^{+2.8}_{-2.8}$

Table 4.2: Expected number Λ_c of lensed events after considering contamination for $\vec{\Omega} = \vec{\Omega}_{\text{true}}$ and expected constraints (68% and 95% credible intervals) on Ω_m and H_0 for different values of the true positive probability ϵ for the data analysis method that is used to identify lensed events (assuming a false positive probability $\alpha = 10^{-9}$). We assume a merger rate of $5 \times 10^5 \text{ yr}^{-1}$ and an observation time of 10 yrs.

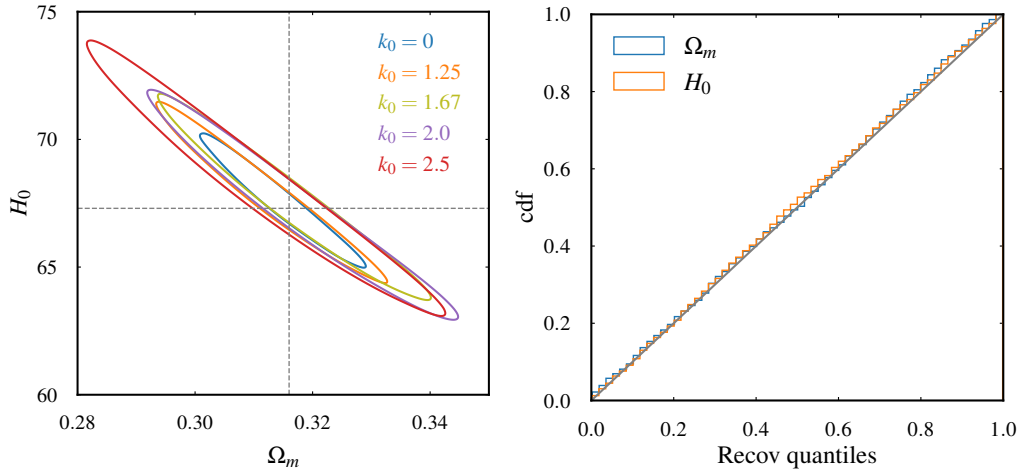


Figure 4.12: *Left panel:* Posteriors on the cosmological parameters (95% credible regions) when we assume different amounts of data contamination. The legends show $k_0 \equiv \alpha/\epsilon$ in units of 10^{-9} , where α (ϵ) is the false (true) positive probability of the lensing identification algorithm. Data contamination only worsens the precision of the posteriors, without causing any systematic biases. *Right panel:* p-p plot obtained from $\sim 10^3$ recovery tests for $\alpha = 10^{-9}$ and $\epsilon = 0.5$. This indicates no systematic bias in cosmological parameter recovery when we account for contamination.

4.6 Conclusions

We expect the lensing cosmography to provide a complementary measurement of cosmological parameters that are comparable to those derived from other cosmological probes, and at the same time using data from an intermediate regime in redshift ($z \sim 10$) that is rarely explored by other probes. The apparent tension that exists between the current low and high redshift measurements underlines the need of additional measurements – especially the ones probing an intermediate redshift regime.

The major sources of systematic errors that affect quasar cosmography [160] are unlikely to affect GW lensing cosmography: GWs are unaffected by extinction, and selection effects in GW searches are better modelled thanks to their intrinsic simplicity. Nevertheless, there are several challenges to overcome before this method can be used to provide reliable measurements of cosmological parameters. The number of lensed events as well as the distribution of their time delays depend on the properties of the astrophysical sources and lenses, apart from the cosmological parameters. Properties of the GW source distribution could be measured accurately from the large number ($\sim 10^6$) of unlensed GW signals that will dominate the data. Since the distribution of the GW source properties is currently largely unknown, we considered a few different astrophysical models for the same, and showed that the expected constraints don't vary significantly. We also showed that the statistical uncertainties in the reconstruction of source properties from GW observations will not significantly affect the inference of cosmological parameters, as long as the source redshift distribution can be reconstructed in an unbiased manner. We also showed that the limited ability of our data analysis

algorithms to distinguish between lensed and unlensed GW events, resulting in some amount of contamination in the sample of lensed GW events, will not bias our inference. This can be avoided by incorporating the effect of data contamination in our Bayesian likelihood models.

One of the major sources of error in our analysis is likely to come from the uncertainty in the distribution of gravitational lenses. In this work, we assumed that the properties of the lens distribution can be extracted from theoretical HMF models. We used several HMFs that model the expected mass distribution of DM halos at different redshifts. We then assumed that these halos are spherical symmetric and used a simple prescription to map the mass of the DM halo to the velocity dispersion of the lens in the SIS model. If the HMF model that we use is significantly different from the “true” model, that can bias the estimation of cosmological parameters. However, in such situations, Bayesian model selection involving several HMF models should enable us to identify the “true” model of the HMF. In the future, we could improve this method by employing parametric models of HMFs that include modelling errors, which can be marginalised over in the Bayesian inference. A combination of EM observations and cosmological simulations can be used to further improve our models of the distribution of lens properties. More complex and realistic lens models incorporate various parameters beyond mass, such as axis ratio and core radius. Modelling the distributions of these parameters and their redshift evolution introduces additional complexities. We plan to explore our analysis using these more sophisticated lens models in future studies. In our current analysis, we have utilized only the time delay and number count information of lensed events. We have not yet incorporated magnification ratio information, which could improve the constraints. While magnification ratio information is limited by luminosity distance measurement errors, it still contains valuable information for lens reconstruction. These additional constraints will be included in our upcoming series of analyses on strong lensing cosmography.

While we have focused on BBH mergers, strongly lensed BNS could be powerful for probing low-redshift cosmology, given their potential EM counterparts and better measured properties due to longer signal duration, despite their smaller lensing optical depth.

We have considered the flat Λ CDM cosmological model and demonstrated that our method can also constrain cosmological parameters within the w CDM framework. The time delay distribution and lensing optical depth are also sensitive to the spatial curvature of the universe. Hence, Strongly lensed GW events could provide a viable probe cosmic curvature. This is a potential extension of our current method, which we intend to pursue in future studies.

5 | Probing the nature of dark matter using strongly lensed gravitational waves from binary black holes

5.1 Introduction

A variety of astronomical observations have established that $\sim 25\%$ of the mass energy in the universe is in the form of some non-baryonic DM [185]. Particle physicists and cosmologists have come up with several candidates for DM, spanning a wide mass range. The list of candidates ranges from extremely light elementary particles [185, 186] to supermassive primordial black holes (BHs) [187].

DM candidates can be classified according to their velocity dispersion, which defines a free streaming length scale. Below this length scale all the cosmological density perturbations are wiped out, so no structure can form in the universe below this length scale. *Cold* DM (CDM), such as the weakly interacting massive particles [188], axions [189] and primordial BHs [190], has small free streaming length scales and does not affect the cosmological structure formation. On the other hand, *hot* DM such as neutrinos is highly relativistic. Free streaming of such relativistic particles would erase perturbations in the matter density even on the scale of galaxy clusters ($\sim 10^{15}M_{\odot}$). The very existence of such large scale structures has ruled out hot DM [191]. In between there exists another class, called *warm* DM (WDM), such as gravitino [192] and sterile neutrino [193]. They are non-relativistic but still have non-negligible velocity dispersion. They have shorter free streaming length than regular neutrinos, and can erase structure on galaxy scales. Thus the existence of galaxies can put some (rather weak) constraints on the mass of the WDM particle.

In the past decades, the cosmological constant dominated CDM model known as Λ CDM has emerged as the standard model of cosmology [194–196]. However, despite decades of effort, neither direct laboratory experiments nor indirect astronomical observations have been able to detect any CDM candidates so far. In addition, though Λ CDM predictions match with observed large scale structure, sub-galactic observations

might be in conflict with the CDM predictions. One is the apparent under-abundance of satellites in the Milky Way, as compared to the earlier CDM simulations, called the “missing satellite problem” [197–200]¹. The second, known as the “core-cusp problem,” is the observed discrepancy between the inferred DM density profiles of low-mass galaxies and that predicted by CDM simulations [202]. Simulations typically predict “cuspy” profiles (steep density profiles at the center) while observations suggest the existence of “cores” (softer density profiles at the center).

While some of these apparent discrepancies between CDM models and observations could be attributed to astrophysical reasons (such as the effect of baryons), several new DM candidates have also been proposed to address them. WDM is the simplest departure from CDM, endowing the DM with a small velocity dispersion. Thermal velocity dispersion enables DM particles to move freely across regions, creating a free streaming effect that smooths out density fluctuations. This process establishes a critical length threshold that inhibits the growth of DM perturbations below this critical scale, effectively preventing structure formation at these smaller scales. For more details on free streaming and the suppression of small-scale structures, see Section 3.4. WDM particle with a mass in keV range predicts the suppression of structures at small scales (~ 100 kpc) without affecting the large scales (\sim Mpc), thus explaining the missing satellites. Another model, called “self-interacting DM” [203], adds a self-interaction cross-section to the DM. The resulting elastic scattering between the DM particles in the inner galactic regions redistributes energy, producing the effect of a core. Fuzzy DM (FDM) particles are ultralight bosons (mass $\sim 10^{-22}$ eV), with de Broglie wavelength larger than the inter-particle separation. The resulting wave-like behaviour leads to formation of solitonic cores at the center of haloes and density granules on scales smaller than \sim kpc are erased, while large scale structure is indistinguishable from CDM [204].

The observation of Lyman- α forest — absorption lines in the distant quasar spectra induced by neutral hydrogen along the line of sight — provides the strongest lower limit ($m_{\text{WDM}} > 3 - 5$ keV) on the WDM mass [205–208]. Combining this with strong gravitational lensing [209] and the abundance of Milky Way satellites has resulted in a joint constraint $m_{\text{WDM}} > 6$ keV [210]. Recent JWST observations of lensed quasars suggest $m_{\text{WDM}} > 6.1$ keV [211]. Different cosmological datasets puts upper bound $m_{\psi} \geq 10^{-22}$ eV on the mass of FDM [212–215]. Stronger constraints are obtained from the survival of an old star cluster in an ultra-faint dwarf galaxy Eridaus II ($m_{\psi} \geq 10^{-19}$ eV) [216] and from the sizes and stellar kinematics of ultrafaint dwarf galaxies ($m_{\psi} \geq 3 \times 10^{-19}$ eV) [217].

Gravitational-wave (GW) observations offer new probes of DM (see, e.g., [218]). The presence of a DM overdensity surrounding a BH can have impact on the GWs emitted during the inspiral and merger with another compact object. The upcoming LISA observatory [219] will be able to detect the effect of the DM on the GW signal, offering a powerful probe of the nature of particle DM [218, 220, 221]. Ultralight bosons, such as axions, can affect the mass and spin of BHs by forming gravitationally bound

¹However, with better simulations and more careful characterisation of the observational selection effects, this discrepancy might be already resolved [201].

states around them [222]. GW emission from such objects could be detected by various GW detectors [223–226]. FDM can also be indirectly detected using pulsar timing arrays if the oscillation frequency falls within their detection band [227].

Gravitational lensing of GWs offer yet another avenue to probe the nature of DM (see, e.g. [228–235], for some recent work). The next-generation (XG) ground-based GW detectors will detect millions of binary BH mergers (BBH) out to high redshifts ($z \sim 10 - 100$) [236]. About 0.1 – 1% [48, 57, 135–139, 141, 237] of them will be strongly lensed by the galaxies and clusters hosted in these DM halos, producing multiple copies of the GW signals. The time delay between the lensed copies of these GW signals can be accurately measured. The exact fraction of lensed mergers and the distribution of lensing time delay will depend on the mass distribution of lenses at various redshifts [238] as well as cosmological parameters [57]. In this chapter, we propose a statistical probe to constrain the mass of the WDM particle using a catalogue of strongly lensed GW detections. If the DM is warm, this will hinder the formation of low-mass halos. This suppression in the the abundance of low-mass halos will result in a reduction in the number of lensed events with small time delays, as small time delays are mostly produced by low mass lenses.

Our proposal is to look for the imprints of WDM on the number of lensed signals, as well as on the distribution of their time delays. This approach is closely connected to the work presented in Chapter 4 on constraining the cosmological parameters from strongly lensed GW signals. Our method does not rely on the accurate knowledge of the source location of the individual signals or the properties of the corresponding lenses. Indeed, the number of lensed events as well as the time delay distribution will also depend on the distribution of source properties (e.g., mass and redshift distribution of BBHs [237, 239, 240]) as well as the lens properties (e.g., the mass function of the DM halos [241] and the lens model [242, 243]). If the distributions of the source and lens properties are known from other observations or theoretical models (e.g., from the observation of unlensed GW signals and cosmological simulations), then the mass of the WDM can be inferred from the observed number of lensed events and their time delay distribution.

We forecast that BBH observations during 10 yrs of operation of XG detectors [244, 245] will be to provide constraints ($m_{\text{WDM}}^{-1} < 0.035 - 0.056 \text{ keV}^{-1}$) that are significantly better than the current constraints ($m_{\text{WDM}} > 6 \text{ keV}$). We simply translate the constraints on m_{WDM} to mass of FDM particle (m_ψ). An optimistic assumption of merger rate will give us the constraint $m_\psi > 7 \times 10^{-19} \text{ eV}$, which is an improvement over existing bounds ($m_\psi > 3 \times 10^{-19} \text{ eV}$).

We also examine the effects of various systematic errors that can affect the inference of the nature of DM. We find that uncertainties in source redshift distributions do not significantly affect our conclusions about the nature of DM. Additionally, constraints do not drastically depend on the assumed models of the source populations. However, using an incorrect model for the distributions of lens parameters can introduce bias; hence, we recommend computing Bayesian evidence to accurately identify the true model. We observe no strong correlation between DM particle mass and cosmological parameters. Our analysis incorporates the effects of misidentified lensed events, allow-

ing us to recover the nature of DM without systematic biases, as long as the level of contamination is not excessive. Finally, we consider the existence of a core in the central region of the lenses, potentially due to the thermal nature of DM particles, and show that this aspect enhances the effectiveness of our method for inferring the nature of DM.

5.2 Warm dark matter

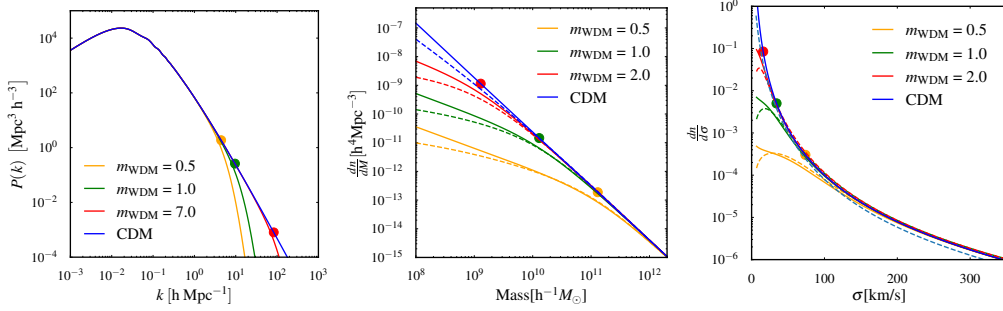


Figure 5.1: *Left*: The power spectrum of linear perturbations as predicted by the CDM model as well as the WDM model with different values of m_{WDM} (in keV). Half-mode scales for different m_{WDM} are shown by the filled circles. *Middle*: HMF for CDM and WDM at redshift $z = 0$. Solid and dashed lines represent the Behroozi [167] and Jenkins [246] HMF models, respectively. Note the suppression in the number density of lower mass halos in the WDM model. Filled circles with different colours denote the half mode mass scale for different m_{WDM} . *Right*: The distribution of the velocity dispersion of lenses produced by the CDM and WDM halos. Here also the solid and dashed lines represents the Behroozi and Jenkins HMF models. Reduction in number density is reflected as reduction of the low σ halos. Filled circles denote the velocity dispersion of the corresponding half mode mass.

Free streaming of WDM particles suppress primordial perturbations at scales smaller than the *free streaming scale*. Fitting functions for modelling the WDM transfer function have been proposed in different studies [200, 247, 248]. They give us a prescription to convert the power spectrum $P_{\text{CDM}}(k)$ of linear perturbations in the CDM model to the same in the WDM model [$P_{\text{WDM}}(k)$]. We use the transfer function given in [248],

$$T(k) = \left[\frac{P_{\text{CDM}}(k)}{P_{\text{WDM}}(k)} \right]^{1/2} = [1 + (\alpha k)^{2\mu}]^{-5/\mu}, \quad (5.1)$$

where $\mu = 1.12$ and

$$\alpha = 0.049 \left(\frac{m_{\text{WDM}}}{\text{keV}} \right)^{-1.11} \left(\frac{\Omega_{\text{WDM}}}{0.25} \right)^{0.11} \left(\frac{h}{0.7} \right)^{1.22} h^{-1} \text{Mpc} \quad (5.2)$$

is called the *effective free streaming scale*. Above, Ω_{WDM} is the energy density in the form of WDM and h is the Hubble constant in units of 100 km/s/Mpc. We can introduce another length scale, the *half mode length scale* λ_{hm} , where the WDM transfer function becomes half: $\lambda_{\text{hm}} = 2\pi\alpha (2^{\mu/5} - 1)^{-1/2\mu}$. This length scale introduces a *half mode mass*

scale $M_{\text{hm}} = \frac{4\pi}{3}\bar{\rho}(\lambda_{\text{hm}}/2)^3$, where $\bar{\rho}$ is the averaged density of the halo. Abundances of DM haloes with mass below the M_{hm} will be suppressed compared to CDM, while the masses above M_{hm} are unaffected.

We use different HMFs that model the comoving number density dn_{CDM}/dM of CDM halos in different mass ranges. Given a HMF in CDM, the same in WDM model for a particular m_{WDM} is obtained using the fitting formula given in [249]

$$\frac{dn_{\text{WDM}}/dM}{dn_{\text{CDM}}/dM} = \left(1 + \frac{M_{\text{hm}}(m_{\text{WDM}})}{M}\right)^{-\beta}, \quad (5.3)$$

where $\beta = 1.16$. The dependence on m_{WDM} comes through M_{hm} . To obtain HMF in WDM model, we use HMF_{CALC} package [95]. For our main analysis we consider the Behroozi [167] model of the CDM HMF. In order to estimate the effect of using an incorrect CDM HMF model, we also consider the Jenkins [246] model of the same implemented in the same package.

These DM halos host galaxies and clusters, which act as gravitational lenses that deflect light as well as GWs. In this chapter, we are concerned about the strong lensing of GWs that produces multiple copies of the GW signals. We approximate these lenses as SISs [59], parameterised by their dispersion velocity σ . We assume that the halos are spherically symmetric and virialised, with average density $\bar{\rho}$ and radius R . This allows us to compute the dispersion velocity of the SIS lens from the halo mass

$$\sigma \simeq \sqrt{\frac{GM}{R}}, \quad M = \frac{4}{3}\pi R^3 \bar{\rho}. \quad (5.4)$$

Figure 5.1 shows the the power spectrum, the HMF and the σ distribution of lenses derived from the HMF, as predicted by the CDM model as well as the WDM model corresponding to different WDM masses. These can be use to compute the expected number of strongly lensed GW signals and the distribution of the time delay between the lensed copies of GW signals.

5.3 Bayesian inference of m_{WDM}

We assume that we have confidently detected N strongly lensed BBH events within an observation period of T_{obs} , each producing two observable copies (lensed images). We aim to compute the posterior distribution of m_{WDM}^{-1} , using the time delays $\{\Delta t_i\}_{i=1}^N$ from the N detected lensed events.

We can write the likelihood $p(N, \{\Delta t_i\} \mid m_{\text{WDM}}^{-1}, T_{\text{obs}})$ as a product of two likelihoods as N and $\{\Delta t_i\}$ are uncorrelated. The likelihood of observing N events can be described as a Poisson distribution

$$p\left(N \mid m_{\text{WDM}}^{-1}, T_{\text{obs}}\right) = \frac{\Lambda\left(m_{\text{WDM}}^{-1}, T_{\text{obs}}\right)^N e^{-\Lambda\left(m_{\text{WDM}}^{-1}, T_{\text{obs}}\right)}}{N!}, \quad (5.5)$$

where $\Lambda(m_{\text{WDM}}^{-1}, T_{\text{obs}})$ is the expected number of lensed events for a given value of m_{WDM}^{-1} and observation time period T_{obs} (Section 5.4.1).

The likelihood of observing a set of time delays $\{\Delta t_i\}$ can be written as

$$p(\{\Delta t_i\} | m_{\text{WDM}}^{-1}, T_{\text{obs}}) = \prod_{i=1}^N p(\Delta t_i | m_{\text{WDM}}^{-1}, T_{\text{obs}}). \quad (5.6)$$

Here we assume each BBH merger to be an independent event and that the time delays are measured accurately and precisely. Above, $p(\Delta t_i | m_{\text{WDM}}^{-1}, T_{\text{obs}})$ is the ‘‘model’’ time delay distribution (Section 5.4.2), evaluated at the measured time delay Δt_i .

5.4 Modeling the expected number of lensed events and time delay distribution

Here we describe the modeling of the expected number of lensed events and the expected distribution of lensing time delay corresponding to different masses m_{WDM} for the WDM particle. This is mostly done in Section 4.3 in the context of cosmography where we modelled time delay distribution and number of lensed events as a function of cosmological parameters. Here we choose to parametrise these in terms of the inverse mass m_{WDM}^{-1} since it has a convenient lower bound of zero (the limit of CDM).

5.4.1 Expected number of lensed events

The expected number of lensed events, $\Lambda(m_{\text{WDM}}^{-1})$, is given by Equation (5.14). However, due to the finite observing time T_{obs} , the number of observed events will be reduced to

$$\Lambda(m_{\text{WDM}}^{-1}, T_{\text{obs}}) = \mathcal{S}(T_{\text{obs}}, m_{\text{WDM}}^{-1}) \Lambda(m_{\text{WDM}}^{-1}), \quad (5.7)$$

where $\mathcal{S}(T_{\text{obs}}, m_{\text{WDM}}^{-1})$ is the effective observation time that takes into accounts the selection effects introduced by the finite observation time:

$$\mathcal{S}(T_{\text{obs}}, m_{\text{WDM}}^{-1}) = \int_{\Delta t=0}^{T_{\text{obs}}} p(\Delta t | m_{\text{WDM}}^{-1}) (T_{\text{obs}} - \Delta t) d\Delta t. \quad (5.8)$$

This selection function ensures that, for a time delay Δt , the first image must arrive at the detector within $T_{\text{obs}} - \Delta t$ from the start of observation. Otherwise, the second image will arrive outside the observation window, rendering it undetectable.

5.4.2 Expected distribution of lensing time delays

We compute the expected time delay distribution $p(\Delta t | m_{\text{WDM}}^{-1})$ by marginalising the distribution of time delay over all other parameters $\vec{\lambda} \equiv \{y, \sigma, z_\ell, z_s\}$ that influence the time delay (see Equation 5.16). We discuss here the choice of $p(\vec{\lambda} | m_{\text{WDM}})$.

Assuming isotropy of space, the distribution of y becomes independent of both cosmological parameters and m_{WDM}^{-1} , leading to:

$$p(\vec{\lambda} | m_{\text{WDM}}^{-1}) = p(y) p(\sigma, z_\ell, z_s | m_{\text{WDM}}^{-1}), \quad (5.9)$$

where $p(y) \propto y$ with $y = (0, 1]$. The term, $p(z_\ell, \sigma, z_s | m_{\text{WDM}}^{-1})$ can be further split as

$$p(\sigma, z_\ell, z_s | m_{\text{WDM}}^{-1}) = p(\sigma, z_\ell | z_s, m_{\text{WDM}}^{-1}) p_b(z_s), \quad (5.10)$$

where $p_b(z_s)$ is the expected/measured distribution of source redshifts, while $p(\sigma, z_\ell | z_s, m_{\text{WDM}}^{-1})$ is computed from the differential optical depth (Equation 11 in [250])

$$p(\sigma, z_\ell | z_s, m_{\text{WDM}}^{-1}) \propto \frac{d\tau}{dz_\ell d\sigma}(z_s, m_{\text{WDM}}^{-1}). \quad (5.11)$$

Given the differential optical depth, we can obtain the strong lensing optical depth by integrating over velocity dispersion and lens redshift

$$P_\ell(z_s, m_{\text{WDM}}^{-1}) = \int_0^{z_s} \int_{\sigma_{\min}}^{\sigma_{\max}} \frac{d\tau}{dz_\ell d\sigma}(z_s, z_\ell, \sigma, m_{\text{WDM}}^{-1}) dz_\ell d\sigma, \quad (5.12)$$

where $\sigma_{\min} = \sigma(M_{\min})$ and $\sigma_{\max} = \sigma(M_{\max})$. M_{\min} and M_{\max} are the minimum and maximum mass of the halo mass range we consider.

This differential optical depth is derived from a HMF that depends on the nature of DM, making the time delay distribution sensitive to the value of m_{WDM}^{-1} . We obtain the model time delay distribution $p(\Delta t_i | m_{\text{WDM}}^{-1}, T_{\text{obs}})$ from intrinsic time delay distribution $p(\Delta t_i | m_{\text{WDM}}^{-1})$ after applying a selection condition that excludes time delays longer than the observation period T_{obs} :

$$p(\Delta t | m_{\text{WDM}}^{-1}, T_{\text{obs}}) \propto p(\Delta t | m_{\text{WDM}}^{-1}) (T_{\text{obs}} - \Delta t) \Theta(T_{\text{obs}} - \Delta t), \quad (5.13)$$

5.5 Expected constraints on warm dark matter

We first ask the question: if the DM is actually cold, how well can we constrain m_{WDM} using future observations of lensed GWs. In order to answer this, we simulate a population of BBH mergers with redshift distribution given by [168]. We assume a BBH detection rate $R = 5 \times 10^5 \text{ yr}^{-1}$ and an observation period $T_{\text{obs}} = 10 \text{ yrs}$. We neglect the selection effects in detection, as XG detectors are anticipated to detect all the BBH mergers out to large red shifts ($z_s \sim 10 - 100$). The mass distribution of the lenses at various redshifts are described by the CDM HMF model of [167], converted to the WDM HMF using Equation (5.3). We consider DM halos in the mass range $10^8 - 10^{15} M_\odot$ (These halos can potentially host galaxies). Lenses are modelled using the SIS model, using Equation 5.4 for converting the halo mass M to the velocity dispersion σ of the lens. This allows us to compute the strong lensing optical depth $P_\ell(z_s | m_{\text{WDM}})$ for sources located at different redshifts z_s (See Subsection 5.4.1 for details). This is convolved with the

redshift distribution $p_b(z_s)$ of the BBH mergers to compute the expected number Λ of lensed events.

$$\Lambda(m_{\text{WDM}}) = R \int_0^{z_s^{\text{max}}} p_b(z_s) P_\ell(z_s | m_{\text{WDM}}) dz_s. \quad (5.14)$$

Above, $z_s^{\text{max}} \simeq 15$ is the redshift horizon of the detector.

In the SIS lens model, the time delay between the two images is (see, e.g. [59]):

$$\Delta t = \frac{32 \pi^2 y}{c} \left(\frac{\sigma}{c} \right)^4 (1 + z_\ell) \frac{D_\ell D_{\ell s}}{D_s}, \quad (5.15)$$

where z_ℓ is the lens redshift, y is the projected location of the source on the lens plane (in units of Einstein radius), while D_ℓ , D_s , and $D_{\ell s}$ are the angular diameter distances to the lens, to the source, and between the lens to the source, respectively. The mass of the WDM particle will also have an imprint on the lensing time delay distribution, since the distribution of σ is a function of m_{WDM} (see Eqs. 5.3, 5.4). We compute the expected time delay distribution $p(\Delta t | m_{\text{WDM}})$ by marginalising the distribution of time delay over all other parameters $\vec{\lambda} \equiv \{y, \sigma, z_\ell, z_s\}$ that influence the time delay (See Subsection 5.4.2 for details).

$$p(\Delta t | m_{\text{WDM}}) = \int p(\Delta t | \vec{\lambda}, m_{\text{WDM}}) p(\vec{\lambda} | m_{\text{WDM}}) d\vec{\lambda}, \quad (5.16)$$

where $p(\vec{\lambda} | m_{\text{WDM}})$ is the expected distribution of $\vec{\lambda}$, given m_{WDM} and the cosmological parameters. We assume the following values of cosmological parameters: $\Omega_m = 0.316, H_0 = 67.3, \sigma_8 = 0.816$ [106].

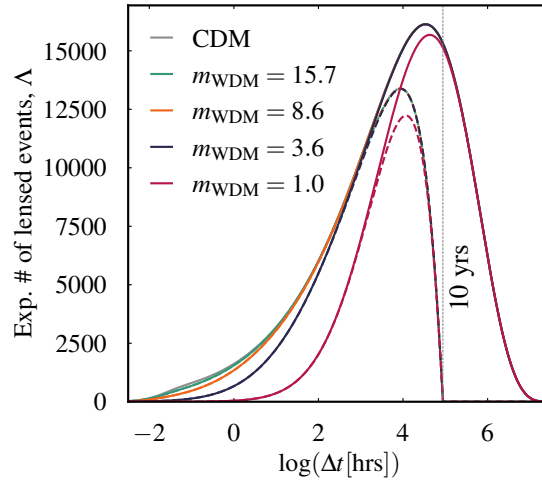


Figure 5.2: Expected distributions of time delay between strongly lensed GW signals, corresponding to different values of m_{WDM} . Note the suppression in number of lensed events compared to CDM, especially for lower time delays, which is the reflection of absence of the lower mass halos for smaller m_{WDM} . Here, we assume an observation period of 10 yrs and BBH detection rate of $5 \times 10^5 \text{ yr}^{-1}$. The time delay distributions measurable from an observation period of 10 yrs are shown by dashed curves.

Figure 5.2 shows the expected number of lensed events $\Lambda(m_{\text{WDM}})$ and the time delay distribution $p(\Delta t | m_{\text{WDM}})$ as a function of m_{WDM} . We see that Λ decreases with decreasing

m_{WDM} , due to the fact that there will be a smaller number of low-mass halos for smaller m_{WDM} . The absence of lower mass halos is reflected in the time delay distribution as the reduction in the of lower time delays. Using these differences in the time delay distribution and total number of lensed events, we will be able to either measure the mass of the WDM particle, or put a lower bound on m_{WDM} . In practice, we put an upper bound on m_{WDM}^{-1} since it has a convenient lower bound of zero (in the limit of CDM, $m_{\text{WDM}} \gg \text{keV}$). Note that, both $\Lambda(m_{\text{WDM}})$ and $p(\Delta t | m_{\text{WDM}})$ are altered by the finite observing time T_{obs} . The calculation of these quantities, $\Lambda(m_{\text{WDM}}^{-1}, T_{\text{obs}})$ and $p(\Delta t | m_{\text{WDM}}^{-1}, T_{\text{obs}})$ are detailed in Section 5.4.

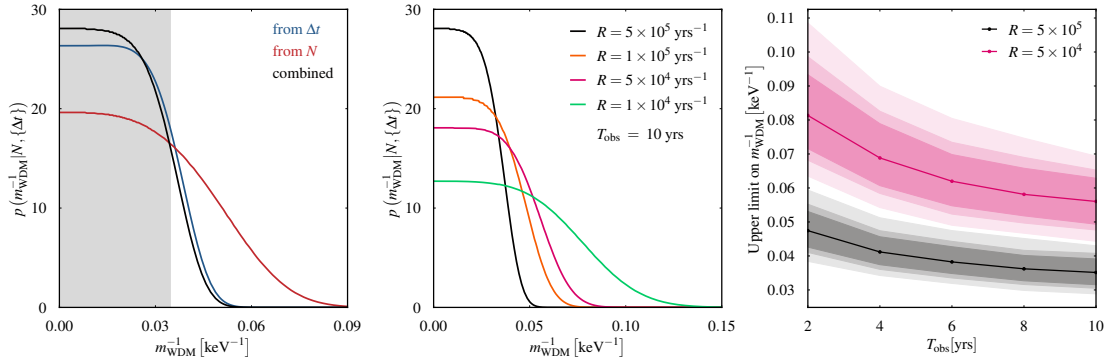


Figure 5.3: *Left*: Posterior distribution of m_{WDM}^{-1} computed from the number of lensed events and time delay distribution separately, along with the combined posterior. The simulated observations assume a BBH detection rate of $R = 5 \times 10^5 \text{ yr}^{-1}$ and $T_{\text{obs}} = 10 \text{ yrs}$. Gray shaded region represents the 90% quantile of the combined posterior, yielding an upper limit of $m_{\text{WDM}}^{-1} \leq 0.035$. *Middle*: Combined constraints from GW lensing on m_{WDM}^{-1} assuming different detection rates, but with $T_{\text{obs}} = 10 \text{ yrs}$. *Right*: 38%, 50% and 68% credible intervals (denoted by different shades) of the distributions of 90% upper limit of m_{WDM}^{-1} obtained from ~ 1000 simulated observations each for different values of R and T_{obs} .

To simulate an observing scenario with N detections of lensed events, we draw one sample of N from a Poisson distribution with mean $\Lambda(m_{\text{WDM}}^{-1}, T_{\text{obs}})$. Further, we draw N samples of lensing time delay, $\{\Delta t_i\}_{i=1}^N$, from $p(\Delta t | m_{\text{WDM}}^{-1} \simeq 0, T_{\text{obs}})$. Using N and $\{\Delta t_i\}_{i=1}^N$ we evaluate the likelihoods $p(N | m_{\text{WDM}}^{-1}, T_{\text{obs}})$ and $p(\{\Delta t_i\} | m_{\text{WDM}}^{-1}, T_{\text{obs}})$. We assume uniform priors on m_{WDM}^{-1} , so final posterior is given by the product of two likelihoods. Details of these calculations are presented in Section 5.3.

Figure 5.3 (left panel) shows the two likelihoods and the posterior obtained from combining these two likelihoods. The 90% quantile of combined posterior is shown in the shaded region, yielding an upper limit $m_{\text{WDM}}^{-1} < 0.035 \text{ keV}^{-1}$, for $R = 5 \times 10^5 \text{ yr}^{-1}$ and $T_{\text{obs}} = 10 \text{ yrs}$. The middle panel shows the combined posteriors, assuming different values of the BBH detection rates. The right panel shows the upper limit of m_{WDM}^{-1} for different observation time periods and merger rates, including the Poisson uncertainties in the estimation.

The FDM also predicts a cut-off in the HMF at small scales, through a mechanism

that is dependent on the de Broglie wavelength rather than a free-streaming length. We translate the constraints on the m_{WDM} to the mass of the FDM particle m_ψ (Figure 5.4). For this, we simply equate the half mode length scale of both. We use the expression of half mode length scale of FDM as given in [213] which considers a transfer function given in [204]. We calculate half mode length scale for WDM using the HMF_{CALC} package [95] which uses the formula given in [249] and a transfer function given in [248]. This is just a simple translation, in order to be more rigorous, one needs to use the HMF in FDM. Even though approximate, this gives us an idea of the prospective constraints on FDM using future observations of GW strong lensing.

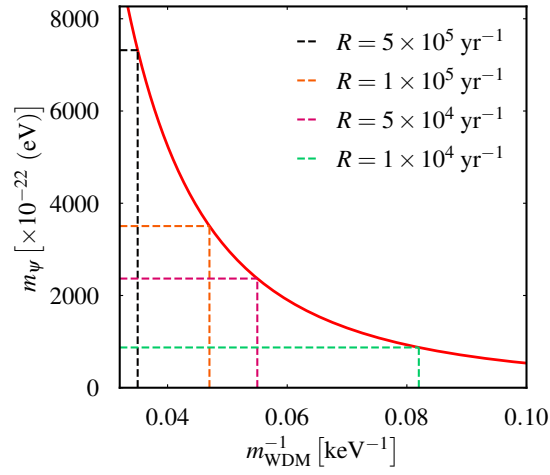


Figure 5.4: The relation between m_ψ and m_{wdm}^{-1} obtained by equating the half mode length scale of FDM and WDM. Dashed vertical line shows the constraints on m_{wdm}^{-1} and corresponding dashed horizontal lines show the translated constraints on m_ψ . Different dashed lines are for different detection rates R , assuming $T_{\text{obs}} = 10$ yrs.

We also check whether we will be able to measure the mass of the DM particle when it is actually warm. To check this, we simulate an observing scenario using the HMF of the WDM model with mass $m_{\text{WDM}} = 9$ keV. Other details of the analysis are kept the same. As seen in Figure 5.5, the true value of m_{WDM} is recovered within 68% credible interval.

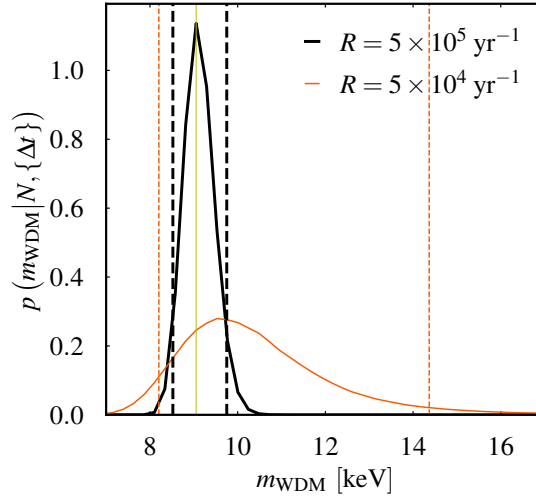


Figure 5.5: Posterior distribution of m_{WDM} assuming that the true nature of the DM is described by the WDM model with $m_{\text{WDM}} = 9$ keV (the yellow solid line in the middle). The plot shows the expected posteriors for $T_{\text{obs}} = 10$ yrs assuming optimistic ($R = 5 \times 10^5 \text{ yr}^{-1}$) and pessimistic ($R = 5 \times 10^4 \text{ yr}^{-1}$) detection rates. Vertical dashed lines represent the 90% credible region of the posteriors.

5.6 Systematic errors

Here we examine the systematic errors that can affect measurements of the DM particle mass. These systematic errors are largely similar to those encountered in measurements of cosmological parameters that we discussed in Chapter 4. Apart from cosmological parameters two essential key ingredients for the computation of lensing optical depth and time delay distribution are:

Redshift distribution of sources This can be obtained with exquisite precision through observations of numerous ($\sim 10^6$) unlensed events in XG detectors[161]. To assess the sensitivity of DM constraints to source population choices, we consider the population synthesis models of isolated binaries presented in [118, 165, 174], as well as models assuming that the BBH merger distribution follows the Madau-Dickinson star formation rate [175], supplemented by a few different delay time distributions (that model the delay time between the star formation and BBH merger). We also explore how uncertainties in source redshift distribution measurements affect the DM particle mass constraints. Based on the analysis in [161], which demonstrates the precision of source redshift distribution measurements using ~ 50000 BBHs in the era of XG detectors, we find that these measurement errors, as reported in [161], do not significantly affect the DM mass limits derived using our method. Our analysis results are presented in Subsections 5.6.1 and 5.6.2.

lens distribution The distribution of lenses is a key component in calculating the time delay distribution and number of lensed events. Computing the differential optical depth requires lens mass and redshift distributions, obtained from the HMF. Since the HMF depends on DM properties, it influences both the time delay distribution and lensed event counts. We demonstrate in [58] that the inference becomes biased when using incorrect HMF models for the inference. Through analysis of various HMF models, we find that the correct models exhibit substantially higher Bayes factors than the incorrect ones. This suggests that pairwise Bayes factor computation can mitigate this systematic error and help to select the appropriate HMF model from available choices. These findings are presented in Subsection 5.6.3.

5.6.1 Effect of source distribution models

The DM mass constraint, derived from lensed event abundances and time delay distribution, depends on source population assumptions. Lensing probability varies with source redshift, with high-redshift sources more likely to be lensed compared to low-redshift sources. Source populations with higher redshift support will generate more lensed events than those without high-redshift extension, consequently yielding tighter DM particle mass limits. We investigate the sensitivity of WDM mass constraints to underlying source population assumption. LIGO-Vigo-KAGRA observations have revealed the universe up to redshift ~ 1 through GWs [251, 252]. While we understand BBH source distribution across this range, the information cannot be extrapolated to very high redshifts. The limited number (~ 100) of detections also limits the precision. Planned upgrades of LIGO (A#, Voyager) and XG detectors will enable precise source distribution mapping across higher redshifts [161, 253]. Given our current lack of knowledge about source distribution at very high redshift (~ 15), we consider various redshift distribution models. These include predictions from population synthesis [118, 165, 174], uniform merger rate in comoving volume and Madau-Dickinson star formation [175] with different delay time distributions [161], such as flat in log and exponential time delay distribution with a timescale $\tau = 0.1$ Gyr. All models are consistent with current low redshift GW observations. Figure 5.6 displays the considered source redshift distributions and their corresponding time delay distributions.

In our analysis we assume that we know the true source redshift distribution and use it to model template time delay distributions. We address the effect of measurement uncertainties in source redshift distribution reconstruction in Section 5.6.2. Here, we focus specially on how source population variations impact limit on m_{WDM}^{-1} . Given the uncertainty in merger rates, we consider both optimistic ($R = 5 \times 10^5 \text{ yr}^{-1}$) and pessimistic ($R = 5 \times 10^4 \text{ yr}^{-1}$) scenarios. Assuming CDM as the true model, we simulate lensed events in a CDM universe and perform parameter inference with WDM templates to determine an upper bound on m_{WDM}^{-1} . Figure 5.7 presents the constraints derived for various source populations at different merger rates. Source populations extending to high redshifts (Dominik and Uniform) yield tighter m_{WDM}^{-1} bounds due to their higher number of lensed events as compared to populations with limited high-redshift extent.

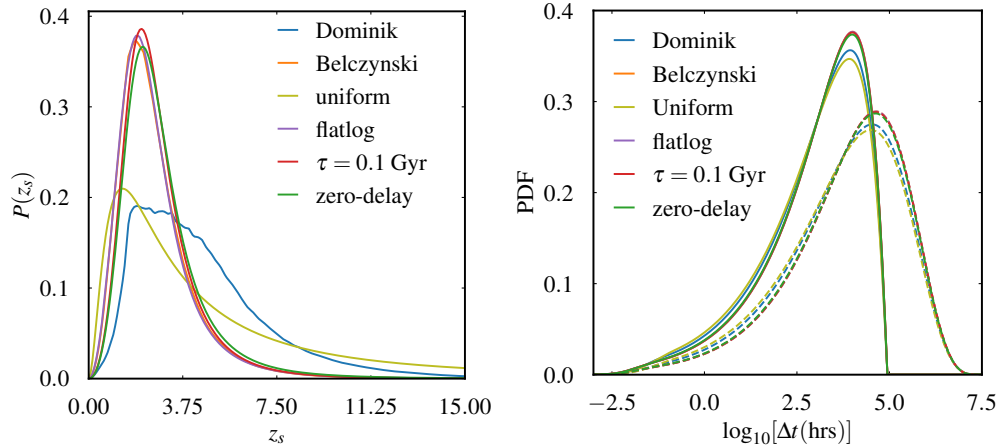


Figure 5.6: *Left*: Source populations models: Population synthesis models from ‘Dominik’ [165] and ‘Belczynski’ [118, 174]. Uniform comoving volume distribution (‘uniform’). Madau-Dickinson star formation rate [175], with three delay time distributions: flat in log (‘flatlog’), exponential with characteristic time scale, $\tau = 0.1$ Gyr, and immediate merger (‘zero-delay’). *Right*: Corresponding strong lensing time delay distributions.

Table 5.1 summarizes the results of our analysis: m_{WDM}^{-1} upper bounds and expected lensed events (Λ) for different source populations.

Detection rate (R in yr^{-1})	Dominik $\Lambda=37372$	Belczynski $\Lambda=20553$	Uniform $\Lambda=36626$	Flatlog $\Lambda=20407$	$\tau = 0.1$ Gyr $\Lambda=22054$	zero-delay $\Lambda=23386$
5×10^5	0.039	0.058	0.033	0.058	0.056	0.053
1×10^5	0.053	0.081	0.045	0.079	0.078	0.075
5×10^4	0.062	0.095	0.053	0.094	0.093	0.087

Table 5.1: Upper bounds (95% limit) on m_{WDM}^{-1} across various redshift distribution models, analyzed for three BBH detection rates ranging from optimistic to pessimistic scenarios. Dominik and Uniform source distributions yield stronger constraints due to their extended high-redshift support, resulting in more lensed events. Expected lensed events (Λ) shown for $R = 5 \times 10^5 \text{ yr}^{-1}$; values for other rates can be obtained through linear scaling.

The results of our analysis demonstrates that while the upper bound on m_{WDM}^{-1} exhibits sensitivity to source population variations, this dependence remains relatively moderate. Even source populations with limited high-redshift support achieve bounds comparable to those from distributions extending to high redshifts. Specifically, the m_{WDM}^{-1} constraints differ by less than a factor of two between these populations. This indicates that our approach maintains its effectiveness in constraining m_{WDM}^{-1} regardless of the source population’s high-redshift support, thus validating its broader applicability across various source redshift distributions.

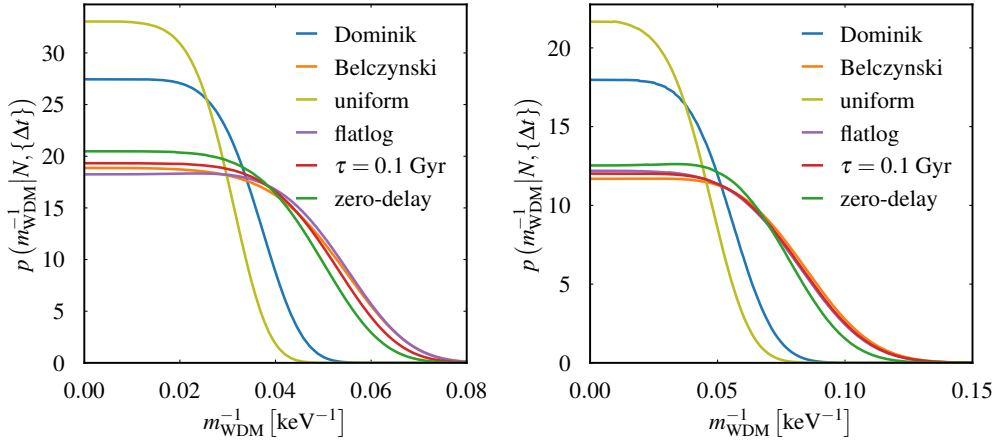


Figure 5.7: Posterior distributions of m_{WDM}^{-1} , for different source distribution models shown in figure 5.6, considering merger rates $R = 5 \times 10^5 \text{ yr}^{-1}$ (left) and $R = 5 \times 10^4 \text{ yr}^{-1}$ (right).

5.6.2 Effect of measurement errors in reconstructing the source redshift distribution

In the preceding section, we explored the sensitivity of m_{WDM}^{-1} constraints to source population variations using a known true redshift distribution. Here, we investigate how measurement errors in source redshift distribution reconstruction propagate to m_{WDM}^{-1} limits. The population analysis method presented in [161] demonstrates constraining merger rate density using approximately 50,000 BBH merger events. Their approach employs a parametric model with free parameters, based on the Madau-Dickinson star formation rate and a delay time distribution. The free parameters are estimated from simulated BBH events detected using XG detectors. Their study [161] presents posteriors of those parameters in Figure 5 and predicted merger rate density in Figure 4.

The most rigorous approach to incorporate measurement errors in our analysis would involve jointly inferring all source redshift distribution model parameters with m_{WDM}^{-1} , then marginalizing over these parameters. This method is computationally intensive and time consuming. Here, we adopt a simplified estimation strategy. We construct a true redshift distribution using the Madau-Dickinson star formation rate combined with an exponential delay time distribution with $\tau = 0.1 \text{ Gyr}$, selecting parameter values from the true values corresponding to the posteriors in Figure 5 of [161]. We sample merger rate density using these posterior samples, convert them to source redshift distributions, and infer the m_{WDM}^{-1} posteriors for each scenario. The average of these posteriors represents the m_{WDM}^{-1} posterior that is marginalised over the astrophysical parameters describing the source redshift distribution model. .

In the left panel of Figure 5.8, the red line represents the true source redshift distribution used to simulate lensed events, assuming CDM as the underlying DM model. The light cyan curves depict the reconstructed distributions obtained through population analysis conducted in [161]. The deep cyan curve illustrates the average of these reconstructed distributions. The right panel presents the strong lensing time delay

distributions corresponding to these source redshift distributions.

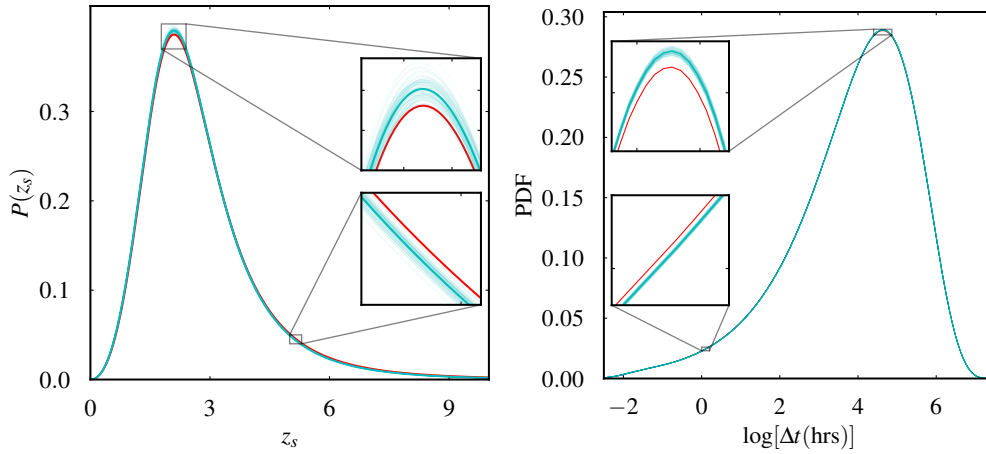


Figure 5.8: *Left*: Source redshift distributions. Red curve denotes the ‘true’ redshift distribution. Cyan curves show reconstructed redshift distributions through population analysis in XG as performed in [161], with the thick bright cyan line representing their average. *Right*: Strong lensing time delay distributions corresponding to these redshift distributions.

Inference of m_{WDM}^{-1} performed with the true (red) and reconstructed (cyan) source redshift distributions yields posteriors shown in the left panel of Figure 5.9. The posterior on m_{WDM}^{-1} inferred using the reconstructed source distributions exhibits a slight shift relative to posteriors from the true distribution. This deviation stems from the marginally biased reconstruction of source redshift distributions (refer to Figure 4 in [161] and Figure 5.8), independent of our WDM mass inference. Upon correcting this reconstruction bias by treating the average source redshift distribution (bright cyan) as the ‘true’ distribution, WDM mass inference with both true (bright cyan) and reconstructed (light cyan) distributions shows aligned posteriors (right panel of Figure 5.9).

Our results demonstrates that statistical errors in source redshift distribution reconstruction do not significantly modify the m_{WDM}^{-1} constraint as the reconstruction error on source redshift distribution is very small in XG detectors [161]. However, the results emphasize the necessity of unbiased reconstruction of source redshift distribution for accurate m_{WDM}^{-1} posterior determination (Figure 5.9).

5.6.3 Lens distribution

The distribution of strong lensing time delays is governed by lens redshift and mass distributions. Our analysis requires statistical distributions of lens parameters extending to high redshifts ($z \sim 15$). Current and forthcoming EM surveys including SDSS, Euclid, LSST, DES, and JWST will characterize lens populations (galaxies and clusters) at low redshifts ($z \sim 2$) [254], informing our analysis within these redshift ranges. While low-mass lenses ($\sim 10^8 M_{\odot}$) remain difficult to detect electromagnetically due to limited angular resolution of EM telescopes, GW detectors can precisely measure

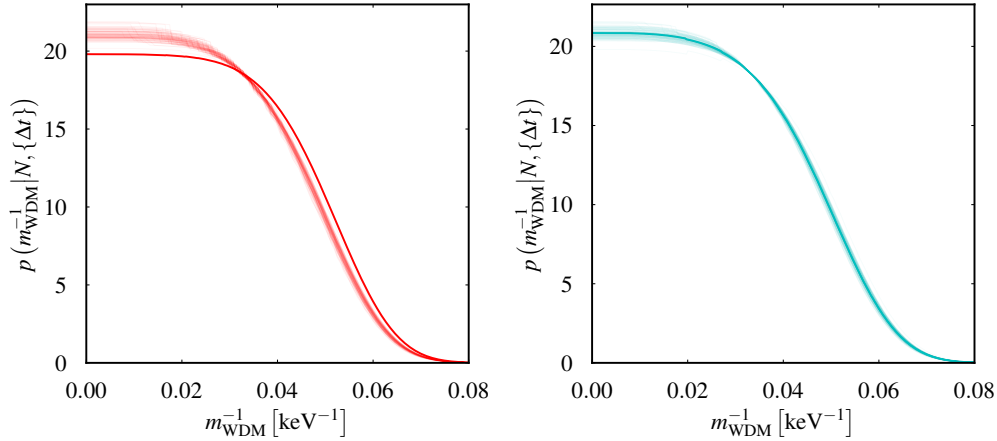


Figure 5.9: *Left*: Lensed events simulated with CDM using the source redshift distribution (given in Figure 5.8 (left)). Bright and light red curves show posteriors using true and reconstructed distributions respectively (red and cyan plots in Figure 5.8, respectively). The systematic shift in posteriors is due to systematic bias in redshift distribution reconstruction. *Right*: Events simulated using bright cyan distribution, with light cyan curves showing unbiased reconstructions (Figure 5.8). Posteriors from both distributions shown in corresponding colors, demonstrating that unbiased source redshift reconstruction preserves the measurement accuracy of DM mass, despite of the measurement uncertainties expected in XG detectors.

their time delays, enabling exploration of these populations. In this initial investigation, we employ the HMF to derive lens distributions and their redshift evolution. HMF, computed from DM-only cosmological simulations, characterizes the mass distribution of DM halos spanning $10^8 - 10^{15} M_{\odot}$, which host the lensing structures. Given multiple HMF models fitted to different simulations, we examine how an incorrect choice of HMF model affects the derived constraints on DM particle mass.

We analyze three HMF models: Behroozi [93], Tinker08 [179], and Jenkins [94]. Assuming CDM as the DM model, we simulate lensed events using one HMF model as the ‘true’ distribution. We then infer the posterior of m_{WDM}^{-1} using both the ‘true’ and alternative HMF models, with results presented in Figure 5.10. The inference of m_{WDM}^{-1} with the ‘true’ model (solid line) yields accurate results, whereas the Jenkins model shows biased inference of the DM mass due to its significant deviation from the ‘true’ model. The analysis is performed for two merger rates: $R = 5 \times 10^5$ and $1 \times 10^5 \text{ yr}^{-1}$.

WDM mass inference using an incorrect HMF model that significantly differs from the ‘true’ model used in event simulation can lead to biased inference, as demonstrated in Figure 5.10. This bias becomes less prominent at lower merger rates due to reduced precision. We quantify this effect through pairwise Bayes factors (ratio of Bayesian evidences between true and wrong HMF models). We compute Bayes factors from ~ 1200 independent simulated catalogs. The true model consistently shows higher Bayesian evidence (Bayes factor > 1), as shown in Figure 5.11. At $R = 5 \times 10^5 \text{ yr}^{-1}$, Bayes factor consistently exceeds 1, favoring the true model. The Tinker08 model shows smaller Bayes factor values than Jenkins, consistent with its unbiased inference and

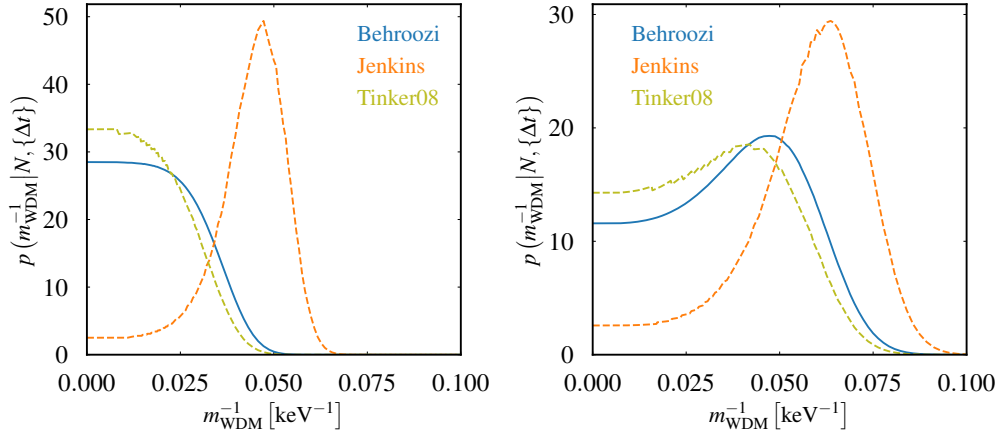


Figure 5.10: *Left*: Posteriors of m_{WDM}^{-1} inferred using different HMF models. Lensed events are simulated using the Behroozi model as ‘true’. Solid lines show inference of m_{WDM}^{-1} using the ‘true’ model, while dashed lines represent inference using alternative models. *Left* and *right* panels show results for merger rates $R = 5 \times 10^5 \text{ yr}^{-1}$ and $R = 1 \times 10^5 \text{ yr}^{-1}$ respectively. Note the biased inference of m_{WDM}^{-1} when the Jenkins model is used in the WDM inference.

closer agreement with Behroozi (‘true’). At a lower merger rate ($1 \times 10^5 \text{ yr}^{-1}$), reduced bias is reflected in smaller Bayes factor values and the true model remains preferred. These results indicate that Bayesian model selection can effectively identify the correct HMF from a given set of available HMFs, helping to mitigate the systematic error due to our lack of knowledge of the true HMF model.

5.6.4 Correlation with cosmological parameters

Apart from the nature of DM, time delay distributions are also sensitive to cosmological parameters (See Chapter 4). We investigate the potential parameter degeneracy in time delay distributions by systematically varying m_{WDM} and cosmological parameters. We conduct two independent analyses with free parameter sets: One set by varying $m_{\text{WDM}}^{-1}, \Omega_M, H_0$ and another set by varying $m_{\text{WDM}}^{-1}, \Omega_M, \sigma_8$. We simulate lensed events considering CDM as ‘true’ model of DM and infer the parameters using WDM templates. Our results demonstrate recovery of injected (‘true’) parameters within 95% credible intervals and reveal no substantive correlation between m_{WDM} and cosmological parameters (Figure 5.12).

This shows that the distinctive signature of WDM in time delay distributions cannot be simply replicated by changing cosmological parameters. This is due to different imprints of these parameters on the time delay distribution: cosmological variations modulate time delay distributions across all temporal scales, whereas the warm nature of DM primarily influences small time delay regimes. Figure 5.12 and 5.13 shows the capability to simultaneously constrain both m_{WDM}^{-1} and cosmological parameters without significant precision loss, due to absence of strong correlations between the parameters.

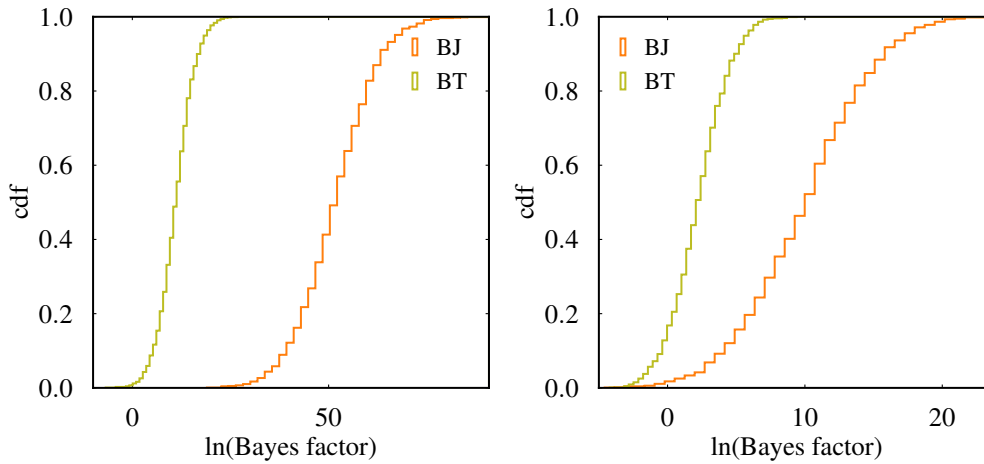


Figure 5.11: Cumulative distribution of logarithmic Bayes factors comparing different HMF models. Results shown for detection rates of $5 \times 10^5 \text{ yr}^{-1}$ (left) and $1 \times 10^5 \text{ yr}^{-1}$ (right). Legend entries (e.g., 'BJ') indicate data simulated using the first model (B: Behroozi) and recovered using the second model (J: Jenkins). Positive values of $\ln(\text{Bayes factor})$ favor the Behroozi model, which was used to generate the true underlying distribution. The analysis consistently identifies the true model for both optimistic and pessimistic merger rates.

A comprehensive analysis requires us to analyze how all cosmological parameters work together. However, due to computational constraints, we restrict our study to a three-parameter analysis. This limited exploration nevertheless demonstrates that the mass of DM is unlikely to exhibit strong correlations with cosmological parameters, given their distinct effects on time delay distributions. A complete analysis incorporating all parameters would require significant optimization of likelihood computations, which we defer to future work.

5.6.5 Effect of contaminations

Identification of strongly lensed GW events poses significant challenges. Several computationally efficient and accurate methods have been developed [140, 255–263]. However, no detection method achieves 100% accuracy, leading to both false positives (unlensed pairs misidentified as lensed) and false negatives (missed lensed pairs). Consequently, a catalog of lensed events contains a mixture of true lensed signals and misidentified unlensed pairs. Each identification method is characterized by its false alarm probability α (probability of misidentifying an unlensed pair as lensed) and detection efficiency ϵ (probability of correctly identifying a true lensed pair) [184].

The treatment is already presented in Subsection 4.5.4 in the context of lensing cosmography. We assume that the number of detected BBH mergers N_{tot} and strongly lensed mergers N follow Poisson distributions of mean Λ_{tot} and Λ , respectively. We

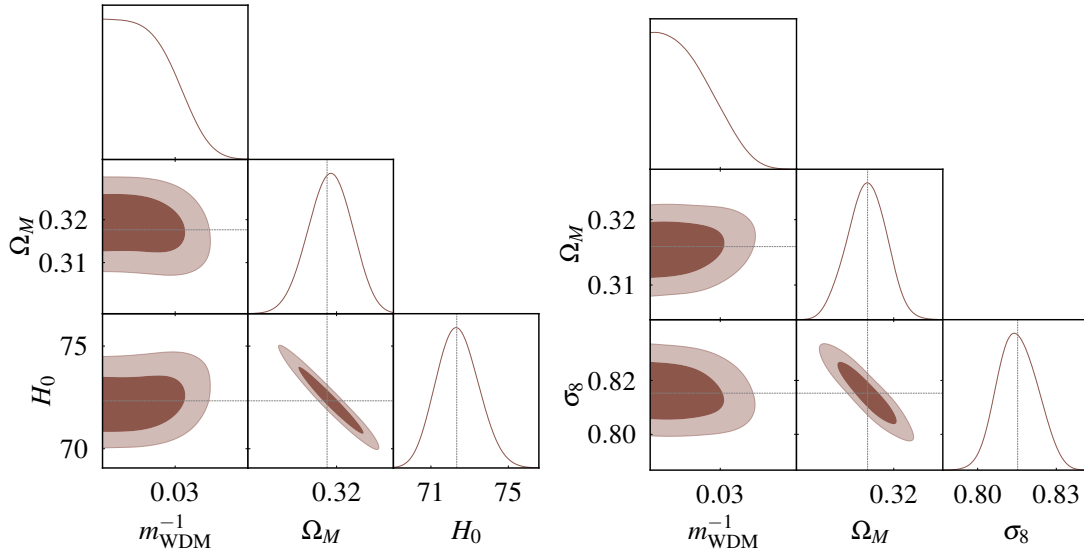


Figure 5.12: Simultaneous estimation of cosmological parameters and the WDM mass. We perform parameter inference assuming two scenarios: 1) treating m_{WDM}^{-1} , Ω_M and H_0 as free parameters (left plots) and 2) assuming m_{WDM}^{-1} , Ω_M and σ_8 as free parameters (right plots). The rest of the cosmological parameters are fixed to some fiducial true values (shown by gray lines). Lensed events are simulated assuming CDM as ‘true’ model of DM and injected (‘true’) cosmological parameters are different for *left* and *right* panel. Dashed cross indicates the ‘true’ values of parameters. Credible intervals at 68% (deep shade) and 95% (light shade). All parameters are recovered within 95% credible intervals. Note that the m_{WDM}^{-1} posteriors do not show any correlation with other cosmological parameters.

define the contamination fraction κ as:

$$\kappa \simeq \frac{\alpha \Lambda_{\text{tot}}^2}{2} \frac{1}{\epsilon u \Lambda_{\text{tot}}} = \frac{\alpha}{\epsilon} \frac{\Lambda_{\text{tot}}}{2u}, \quad (5.17)$$

where $u = \Lambda / \Lambda_{\text{tot}}$ is the expected lensing fraction. Note that κ depends on m_{WDM}^{-1} and the observing period T_{obs} through the lensing fraction and total event count respectively, we suppress this notation for clarity. The ratio $\kappa_0 = \alpha / \epsilon$ characterizes the receiver operating characteristic (ROC) of the lensing identification method (see, e.g., [140, 255, 262]). Current methods (e.g., [262]) achieve $\epsilon \sim 0.6$ at $\alpha \sim 10^{-6}$. To keep the contamination fraction low (about 10%), we would need $\alpha \sim 10^{-9}$ for $\epsilon \sim 0.5$, $\Lambda_{\text{tot}} \sim 10^6$ and $u = 0.01$. One hopes to achieve this in future GW observations due to the increased precision of measurements.

We incorporate the contamination fraction following the methodology outlined in [264]. The expected number of lensed events is modified by introducing a contamination fraction κ as follows:

$$\Lambda_{\text{c}}(m_{\text{WDM}}^{-1}, T_{\text{obs}}) = \epsilon [1 + \kappa] \Lambda(m_{\text{WDM}}^{-1}, T_{\text{obs}}). \quad (5.18)$$

This formulation allows us to model contamination effects on the expected number

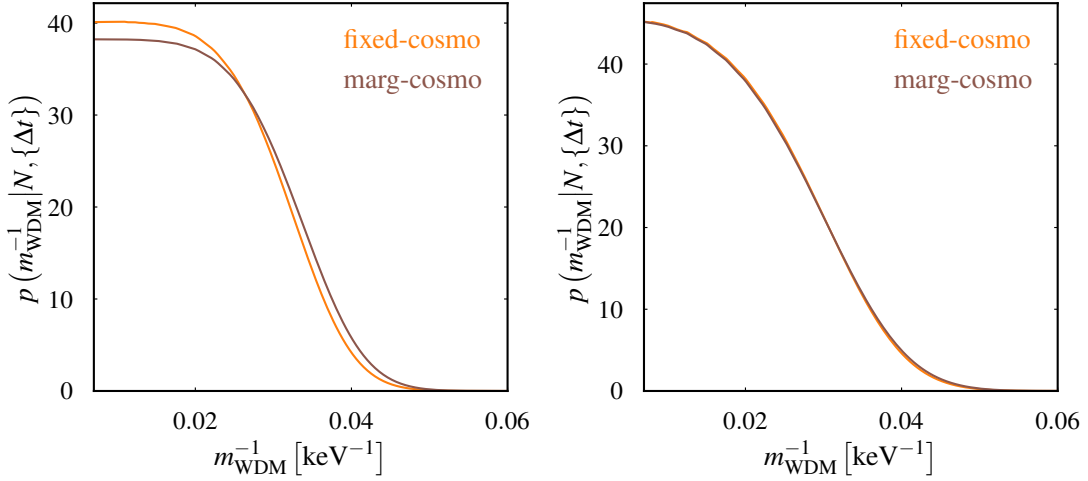


Figure 5.13: Posterior of m_{WDM}^{-1} when cosmological parameters are fixed (orange) and when marginalised over the cosmological parameters (brown). The *left* panel shows marginalisation over Ω_M and H_0 , while the *right* panel shows marginalisation over Ω_M and σ_8 . These marginalised m_{WDM}^{-1} posteriors correspond to the left and right corner plots in Figure 5.12, respectively

of lensed events once κ_0 is determined through simulations. The observed time delay distribution comprises a mixture of lensed and unlensed delays. The contaminated time delay distribution takes the form:

$$\begin{aligned}
 p_c(\Delta t \mid m_{\text{WDM}}^{-1}, T_{\text{obs}}) \\
 = \frac{\kappa}{1 + \kappa} p_{\text{unlens}}(\Delta t \mid T_{\text{obs}}) + \frac{1}{1 + \kappa} p_{\text{lens}}(\Delta t \mid m_{\text{WDM}}^{-1}, T_{\text{obs}}),
 \end{aligned} \tag{5.19}$$

which we use for the estimation of m_{WDM}^{-1} . Above, $p_{\text{lens}}(\Delta t \mid m_{\text{WDM}}^{-1}, T_{\text{obs}})$ is given by Equation 5.16, and the unlensed time delay distribution is given by:

$$p_{\text{unlens}}(\Delta t \mid T_{\text{obs}}) \propto (T_{\text{obs}} - \Delta t) \Theta(T_{\text{obs}} - \Delta t). \tag{5.20}$$

We investigate the impact of contamination on the inference of m_{WDM}^{-1} by simulating lensed events with CDM as the underlying DM model. Our analysis considers different BBH merger rates, from optimistic to pessimistic. We adopt Planck18 [72] cosmological parameters, the source redshift distribution from Dominik [165], and the ‘Behroozi’ [93] HMF for lens distribution. For the detection method, we set a false probability per pair of $\alpha = 10^{-9}$ and consider various detection efficiencies: $\epsilon = 0.4, 0.5, 0.6, 0.8$, corresponding to $\kappa_0 = [2.5, 2, 1.67, 1.25] \times 10^{-9}$. These parameters yield contamination fractions of approximately 84%, 67%, 56%, 42% respectively. Figure 5.14 illustrates the evolution of m_{WDM}^{-1} constraints as a function of κ_0 , and Table 5.2 presents the 95% confidence limits on m_{WDM}^{-1} for different κ_0 values across our considered merger rates.

Figure 5.14 presents the expected posteriors on m_{WDM}^{-1} assuming different amounts of

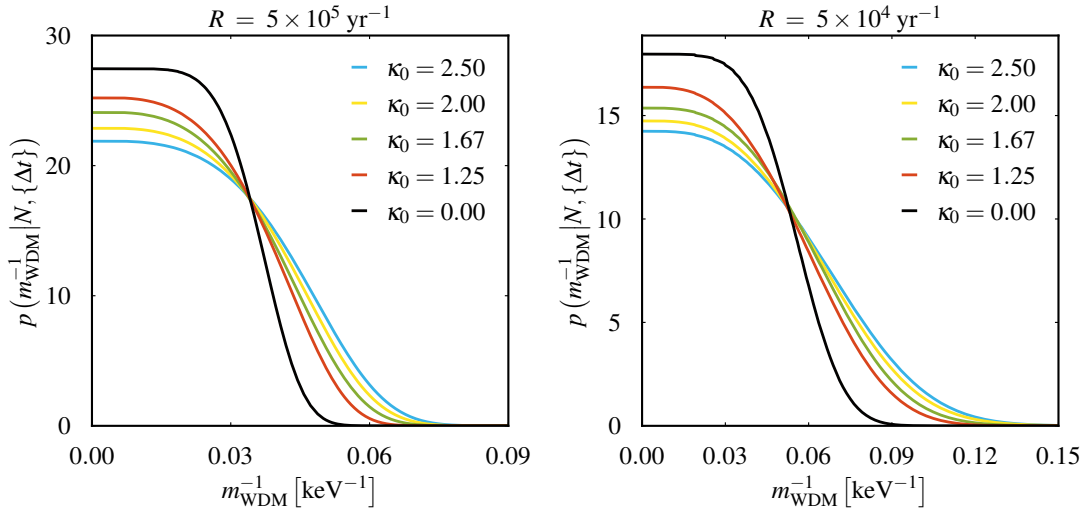


Figure 5.14: Posterior distributions of m_{WDM}^{-1} for different values of $\kappa_0 = \alpha/\epsilon$, where α is the false alarm probability and ϵ is the efficiency of the lensing identification method. Note that κ_0 is in units of 10^{-9} . The *left* and *right* panels correspond to merger rates of $5 \times 10^5 \text{ yr}^{-1}$ and $5 \times 10^4 \text{ yr}^{-1}$ respectively, with an observation time period of $T_{\text{obs}} = 10 \text{ yrs}$. Here, $\kappa_0 = 0$ represents the case without contamination, while increasing values of κ_0 indicate higher contamination fractions.

$R \text{ [yr}^{-1}\text{]}$	No cont.	$\kappa_0 = 1.25$	$\kappa_0 = 1.67$	$\kappa_0 = 2$	$\kappa_0 = 2.5$
5×10^5	0.039	0.040	0.042	0.044	0.047
1×10^5	0.053	0.055	0.06	0.062	0.066
5×10^4	0.062	0.065	0.070	0.073	0.077

Table 5.2: The 95% confidence limits on m_{WDM}^{-1} for different merger rates and different values of $\kappa_0 = \alpha/\epsilon$, where α is the false alarm probability and ϵ is the efficiency of the lensing identification method. Note that κ_0 is in units of 10^{-9} . These limits are derived from the posterior distributions shown in Figure 5.14.

contamination (the value of $\kappa_0 = \alpha/\epsilon$ is shown in the legend). Note that these posteriors are estimated from one realisation of the observing sample (N and $\{\Delta t\}$), and will suffer from Poisson fluctuations. To understand the spread in the m_{WDM}^{-1} upper limits due to Poisson fluctuations, we repeat the analysis from ~ 1200 different simulated catalogs of lensed events (i.e., ~ 1200 different realisations of N and $\{\Delta t\}$) and compute the distribution of the m_{WDM}^{-1} upper limits. These are shown in Figure 5.15. In each independent test, the total number of simulated lensed events and their corresponding time delays are subject to distinct realizations of Poisson fluctuations, leading to variations in the 95% limit of m_{WDM}^{-1} . We can see that increasing κ_0 (corresponding to higher contamination) systematically shifts the 95% limits of m_{WDM}^{-1} toward larger values, indicating a weakening of constraints due to contamination. However, note the degradation due to contamination is not significantly larger than the intrinsic Poisson fluctuations in the upper limits.

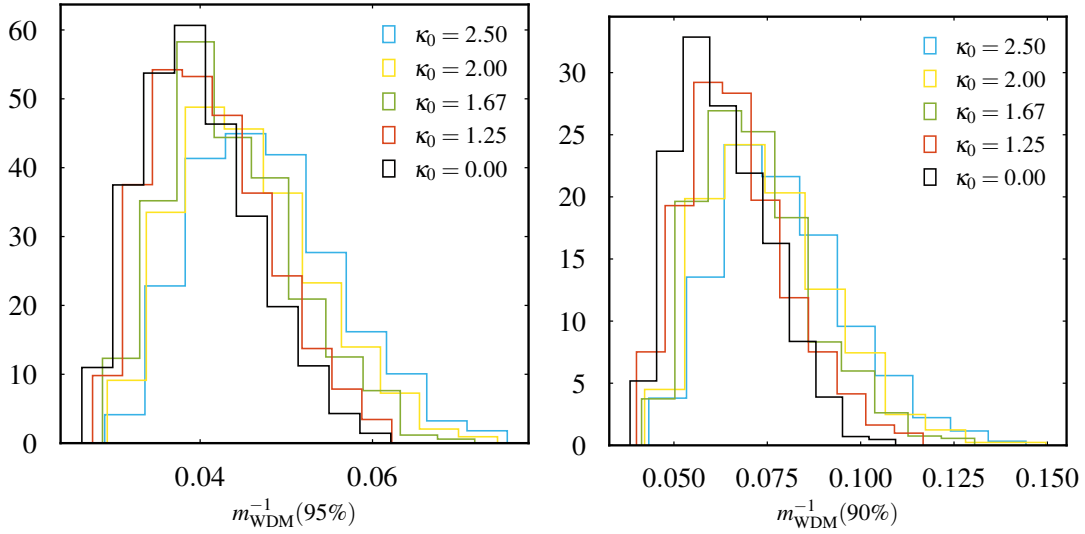


Figure 5.15: Distribution of 95% confidence limits on m_{WDM}^{-1} derived from 1200 independent catalogs of merger events, assuming merger rates $5 \times 10^5 \text{ yr}^{-1}$ (left) and $5 \times 10^4 \text{ yr}^{-1}$ (right) with observation time $T_{\text{obs}} = 10 \text{ yrs}$. The systematic shift toward higher values with increasing contamination illustrates the effect of contaminations on the inference of m_{WDM}^{-1} .

5.6.6 Effect of core

The impact of WDM extends beyond its well-known suppression of structure below the free-streaming length scale, which reduces low-mass halo abundances relative to CDM. WDM also fundamentally alters halo density profiles. While CDM halos exhibit cuspy central density profiles, WDM halos are characterized by central cores. This modification affects both time delay distributions and the number of lensed events.

Here we investigate the effect of presence of a central core in the lens on the time delay distribution and total number of lensed events. The existence of a core inside a halo formed in WDM scenario can be established through a phase space density argument, originally proposed by Tremaine and Gunn [265]. Liouville's theorem states that in a collisionless fluid, the fine-grained phase space density remains constant throughout cosmic history. In the WDM model, the fluid is described by a Fermi-Dirac distribution. The absolute value of the phase space density is fixed at the time of decoupling when the fluid becomes collisionless. By comparing the initial maximum phase space density with the phase space density after virialization, lower limits on the size of the core is obtained [200, 265–268]. [200] argued that a thermal candidate with a mass of 1 keV produces a typical core size of approximately 10 pc for a halo with velocity dispersion of 100 km.s^{-1} . Subsequent simulation results by [268] and [266] further support this, suggesting that thermal DM candidates with masses of 1 – 2 keV generate core sizes $\sim 10 - 50 \text{ pc}$.

Following [200], we consider the following scaling relationship for the core radius (r_c) as a function of m_{WDM} , local matter density parameter (Ω_{m0}), and velocity dispersion

of halo (σ_h):

$$r_{\text{core}} \simeq 10 \text{ pc} \left(\frac{\text{keV}}{m_{\text{WDM}}} \right)^2 \left(\frac{0.3}{\Omega_{m0}} \right)^{\frac{1}{2}} \left(\frac{100 \text{ km s}^{-1}}{\sigma_h} \right)^{\frac{1}{2}}. \quad (5.21)$$

For a given halo mass, σ_h is a redshift-dependent quantity, so the size of the core for a given halo mass depends on the formation redshift. The scaling of the ratio of r_c and virial radius of halo with redshift is given in [268]. The equation for core radius (Equation 5.21) which we consider has roughly the same scaling as presented in [268]. The prefactor can be larger than 10 [266, 267]. A larger core size would enhance the effect of WDM on the time delay distribution and total number of lensed events. Thus, the results obtained using Equation 5.21 can be considered a conservative limit.

We investigate the core-SIS model for gravitational lenses [269], where introducing a core in the halo's central region has two counteracting effects on the strong lensing time delay distribution. The first effect is the reduction in time delay compared to no-core case, which shifts the distribution towards smaller time delays, while the second effect involves the reduction in lensing probabilities of low-mass halos due to decreased Einstein radius, which shifts the distribution towards higher time delays. When the core radius to Einstein radius ratio exceeds 0.5, multiple image formation becomes impossible, significantly suppressing the lensing probability of low-mass halos at high redshifts. The lensing probability of high-mass halos ($> 10^{10} M_{\odot}$) remain largely unaffected due to minimal core radius (from Equation 5.21, where high σ_h values yield small r_{core}). As a result the core radius remains very small compared to the Einstein radius at all redshifts, so larger time delays are mostly not affected by the presence of the central core. Due to the dominance of the second effect, the overall time delay distribution effectively shifts towards higher time delays (Figure 5.16). This effect amplifies the distinctions observed in WDM scenarios when core density profile is not considered. Furthermore, introduction of core reduces the total number of lensed events (Figure 5.16), thereby enhancing the distinguishability between CDM and WDM.

Now We examine the impact of incorporating a core in the lens model on the inference of m_{WDM}^{-1} . Using lensed events simulated in CDM, we perform inference of m_{WDM}^{-1} with templates constructed using a core-SIS lens profile, results shown in Figure 5.17. The results demonstrate that m_{WDM}^{-1} is more tightly constrained compared to inference using templates with coreless (SIS) lenses, consistent with our earlier discussion that the presence of a core enhances the ability to distinguish WDM models from CDM. With core lenses, we obtain constraints of $m_{\text{WDM}}^{-1} \leq 0.011$ and $m_{\text{WDM}}^{-1} \leq 0.033$ for merger rates of $5 \times 10^5 \text{ yr}^{-1}$ and $5 \times 10^4 \text{ yr}^{-1}$ respectively. In contrast, inference with coreless lenses yields weaker constraints of $m_{\text{WDM}}^{-1} \leq 0.039$ and $m_{\text{WDM}}^{-1} \leq 0.062$ for the same respective merger rates. All cases assume an observation time period of 10 yrs.

Here we assume the central core in the lens arises solely from the thermal motion of DM particles. Simulation studies [266, 268] indicate that cores produced by the warm nature of DM are quite small (approximately 10^{-3} of the virial radius at formation). Their findings conclude that the core radii of halos observed at $z \simeq 0$ are expected to be significantly smaller than the observed cores ($\sim \text{kpc}$) in nearby low surface brightness

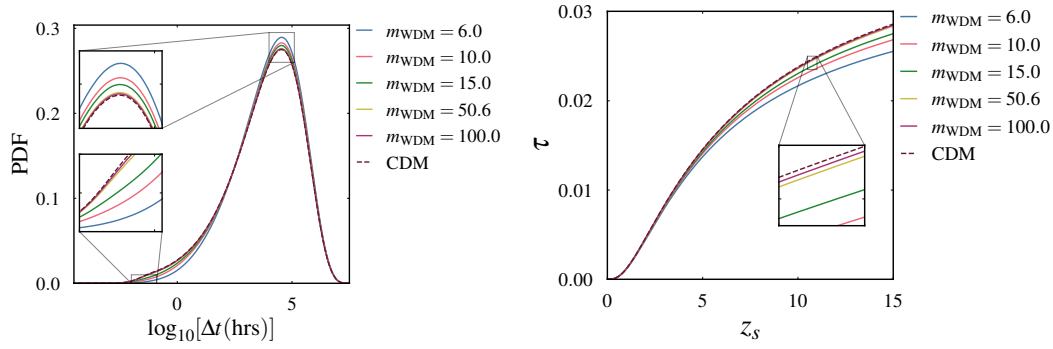


Figure 5.16: *Left*: Effect of a central core in the lens on time delay distributions. Using Equation 5.21, the results for different m_{WDM} are presented. Increasing the core radius shifts the time delay distribution towards higher time delays. The distinguishability power has increased, as evidenced by the clear separation of $m_{\text{WDM}} = 50, 100$ keV from the CDM scenario, which was not apparent in the absence of a lens core. *Right*: Impact of presence of core on the lensing optical depth. The suppression in lensing optical depth with increasing core radius is shown, with the differences from CDM now more pronounced compared to the no-core scenario.

galaxies ($M \sim 10^{10} M_{\odot}$). These studies suggest that WDM alone cannot explain the observed cores in dwarf galaxies, and if cores are required, baryonic feedback is likely the dominant mechanism for core formation in halos. Therefore, proper core modeling necessitates the inclusion of baryons and their effects (feedback, cooling) on DM, which we plan to address in future work using improved high-redshift simulation results. Also the presence of core produces a type-III lensed image near the centre of the lens which is demagnified but if it has sufficient SNR can be detectable through its Morse phase shift (by π) [270]. Which will help to model lens core.

Here we have investigated the impact of incorporating cores within lenses in WDM model. Halos in FDM model similarly develop central cores [271]. These cores in FDM manifest as solitonic cores, arising from the equilibrium between quantum pressure—a consequence of the uncertainty principle—and gravity. The cores in FDM exhibit distinct scaling relations compared to those in WDM. Implementation of FDM core profiles in our framework could potentially enhance constraints on the FDM particle mass parameter. We will explore this in our future study.

5.7 Conclusions

Because of their inherent simplicity, GWs are unaffected by extinction, and selection effects in GW searches are well modelled. This makes GW strong lensing a cleaner probe of the nature of DM, as compared to, e.g., optical lensing. Constraints on the mass of the WDM/FDM particle expected from future GW strong lensing observations are significantly better than the current bounds [211, 217].

In our observables there is no degeneracy between the DM properties and cos-

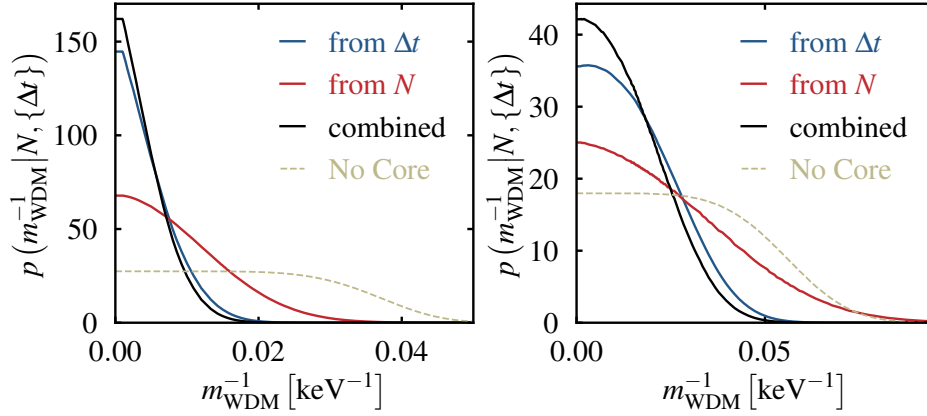


Figure 5.17: Posterior distribution of m_{WDM}^{-1} . Lensed events are simulated in CDM and the inference of m_{WDM}^{-1} using templates with a core-SIS lens profile where the core radius is given by Equation 5.21. The *left* and *right* panels correspond to merger rates of $5 \times 10^5 \text{ yr}^{-1}$ and $5 \times 10^4 \text{ yr}^{-1}$ respectively, both assuming an observation period of 10 yrs. For comparison, dashed lines show the inference of m_{WDM}^{-1} using templates without a central core in the lens (SIS model).

mological parameters. This should allow us to constrain both the nature of DM and cosmological parameters simultaneously from future observations. A wrong model of the HMF can bias our measurements. However, we should be able to identify the right HMF model from the data using Bayesian model selection. We discussed different potential systematic errors in our analysis and ways to mitigate them in Section 5.6.

A number of obstacles need to be addressed before this technique can be applied to real data. Properties of astrophysical sources and lenses determine both the number of lensed events and the distribution of their time delays. Some of the relevant parameters, such as the redshift distribution of BBH mergers, can be inferred from the large number of unlensed GW signals as well as the stochastic GW background. For other parameters, such as the distribution of the lens properties, will need to rely on large-scale cosmological simulations and galaxy surveys.

In this work, we have assumed that the lenses are modelled by simple SISs, whose parameters are obtained from the HMF using a simple prescription. Our current analysis neglects effects of halo substructure and baryonic effects. We are developing more accurate lens models and methods to account for detector selection effects in upcoming upgrades. False positives in strongly lensed signal identification can contaminate the observational sample, but modeling contamination effects in the catalog enables unbiased inference of DM properties. Additionally, strongly lensed BNS with EM counterparts could allow detailed probing of lens galaxy profiles, potentially providing tighter constraints on DM properties.

6 | Conclusions and Future Directions

This thesis has explored two important aspects of GW strong lensing: its potential as a cosmological probe and its ability to constrain the nature of DM. The planned XG detectors with improved sensitivity will detect millions of GWs, with thousands being strongly lensed. We have developed methods to use these strongly lensed GW events for cosmography and to determine the nature of DM. Through detailed analysis, we have demonstrated that GW lensing offers a promising new window into extracting cosmological parameters, particularly valuable for probing the intermediate redshift regime ($z \sim 10$) that is rarely explored by other methods. This is important given the current tension between low and high redshift measurements in cosmology. Our work has shown that GW strong lensing can place better constraints on the mass of DM particles than current bounds for both WDM and FDM models. We have also shown that there is no strong degeneracy between the mass of DM particles and cosmological parameters in our observables. Thus, GW lensing could, in principle, enable simultaneous constraints on cosmological parameters and DM properties. The intrinsic simplicity of GW signals provides significant advantages over traditional optical lensing studies, particularly in terms of reduced systematic uncertainties and better-modeled selection effects.

Several important developments need to be completed before these methods can be turned into a viable observational program. The SIS model we currently use for lenses is an oversimplified model, and future work will focus on incorporating more realistic lens models with halo substructure and baryonic effects, along with better prescriptions for mapping the mass distribution of DM halos to lens properties [272]. Extension to BNS systems offers unique advantages despite their lower redshift reach ($z \lesssim 2$ even for XG detectors). While the lensing optical depth of BNS will be smaller compared to BBHs which could be observed out to very large redshifts ($z \sim 10 - 100$), BNS mergers are expected to be numerous ($\sim 10^6$ detections per year in XG [273]). Their long signal duration in the detector band allows their properties to be measured with better accuracy, and some will produce observable EM counterparts. These BNS with EM counterparts could allow us to probe the detailed profile of the lensing galaxy, potentially enabling better constraints on the nature of DM [274]. Data from EM observations and cosmological simulations will improve our understanding of lens distributions. For upcoming detector upgrades [275–277], we are working on forecasting expected constraints on

cosmological parameters with proper modeling of detector selection functions [278]. Our Bayesian analysis framework requires computing template time delay distributions for many points in the parameter space of cosmology, DM mass, and other astrophysical parameters. Currently, generating these template distributions is computationally expensive. To address this challenge, we plan to develop surrogate models for faster computation, enabling us to include more parameters and obtain reliable constraints. These improvements will be valuable as detector sensitivity increases and our catalog of lensed events grows, making our methods effective tools to study cosmology and the nature of DM.

List of publications

Papers relevant to the thesis

1. **Souvik Jana**, Shasvath J Kapadia, Tejaswi Venumadhav and Parameswaran Ajith.
Cosmography Using Strongly Lensed Gravitational Waves from Binary Black Holes,
[Phys. Rev. Lett.](#), 130:261401 (2023), [arXiv:2211.12212](#)
2. **Souvik Jana**, Shasvath J Kapadia, Tejaswi Venumadhav, Surhud More, and Parameswaran Ajith.
Strong-lensing cosmography using third-generation gravitational-wave detectors,
[Classical Quantum Gravity](#), 41(24):245010 (2024), [arXiv:2405.17805v2](#)
3. **Souvik Jana**, Shasvath J Kapadia, Tejaswi Venumadhav, Surhud More, and Parameswaran Ajith.
Probing the nature of dark matter using strongly lensed gravitational waves,
[arXiv:2408.05290](#)
4. **Souvik Jana**, Shasvath J Kapadia, Tejaswi Venumadhav, Surhud More, and Parameswaran Ajith.
Probing the nature of dark matter using strongly lensed gravitational waves: Characterisation of systematic errors (In prep)

List of Figures

1.1	Gravitational wave polarisations	17
2.1	Focusing of GW	29
2.2	Parametric path of GW ray	31
2.3	Deflection of GW by a point mass M	32
2.4	Sketch of gravitational lensing system	33
2.5	Effect of convergence and shear: shape distortions	37
2.6	Time delay surfaces for varying source-lens configurations	40
2.7	Critical curves and caustic of an axially symmetric lens with no singularity	48
2.8	Critical curves and caustics of a SIS lens	52
3.1	Evolution of Jeans mass	64
3.2	Gaussian probability distribution of density perturbations at different smoothing scales	67
4.1	Lensing optical depth and converting a luminosity distance distribution to source redshift distributions assuming different cosmologies	77
4.2	The distribution of velocity dispersion of lenses and halo mass function	78
4.3	Imprint of cosmology on the number of lensed events	81
4.4	Expected constraints from GW strong lensing on the cosmological parameters and comparison with Planck 2018	82
4.5	Expected constraints from GW strong lensing on the cosmological parameters for different values of merger rate, R	83
4.6	Prospective constraints on parameters w_0 and Ω_m from GW strong lensing in w CDM model of cosmology	84
4.7	Variation of precision in measuring cosmological parameter with the variation of source population	86

4.8	Effect of errors in measuring the source redshift distribution on the measurement of cosmological parameters	87
4.9	Biased measurement of cosmological parameters due to wrong halo mass function	89
4.10	p-p plot: reflection of bias for the recovery using wrong HMF, a statistical quantification of the bias	90
4.11	Distribution of pairwise Bayes factors	92
4.12	Expected constraints after accounting for contamination effect and p-p plot for different recovery tests showing an unbiased recovery of the cosmological parameters	94
5.1	Power spectrum, halo mass function and distribution of velocity dispersion of halos in WDM model	100
5.2	Expected distributions of time delay between strongly lensed GW signals, corresponding to different values of m_{WDM}	104
5.3	Posterior distribution of m_{WDM}^{-1} computed from the number of lensed events and time delay distribution separately, along with the combined posterior.	105
5.4	The constraints on m_{ψ} and m_{wdm}^{-1}	106
5.5	Recovery when dark matter is truly warm	107
5.6	Source populations models and corresponding strong lensing time delay distributions	109
5.7	Posterior distributions of $m_{\text{WDM}'}^{-1}$ for different source distribution models.	110
5.8	Errors in measuring source redshift distribution in XG era	111
5.9	Effect of measurement error of source redshift distribution on the inference of m_{wdm}^{-1}	112
5.10	Posteriors of m_{WDM}^{-1} inferred using different HMF models: Biased recovery when wrong HMF model is used for recovery	113
5.11	Cumulative distribution of logarithmic Bayes factors comparing different HMF models.	114
5.12	Correlation with cosmological parameters.	115
5.13	Posterior of m_{WDM}^{-1} when cosmological parameters are fixed and when marginalised over the cosmological parameters.	116
5.14	Posterior distributions of m_{WDM}^{-1} for different values of contamination fraction for two different merger rates.	117

5.15	Distribution of 95% confidence limits on m_{WDM}^{-1} derived from 1200 independent catalogs of merger events, assuming two different merger rates	118
5.16	Time delay distributions and strong lensing optical depth when the lens is modelled as core SIS and their variation with m_{WDM}	120
5.17	Posterior distribution of m_{WDM}^{-1} . Lensed events are simulated in CDM and the inference of m_{WDM}^{-1} using templates with a core-SIS lens profile.	121

List of Tables

4.1	Expected number of lensed events and expected constraints on Ω_m and H_0 for different models of redshift distribution of BBH mergers	86
4.2	Expected number of lensed events after considering contamination for and expected constraints on Ω_m and H_0 after accounting for contaminations	93
5.1	Upper bounds (95% limit) on m_{WDM}^{-1} across various redshift distribution models, analyzed for three merger rates ranging from optimistic to pessimistic scenarios.	109
5.2	The 95% confidence limits on m_{WDM}^{-1} for different merger rates and different values of $\kappa_0 = \alpha/\epsilon$, where α is the false alarm probability and ϵ is the efficiency of the lensing identification method. Note that κ_0 is in units of 10^{-9} . These limits are derived from the posterior distributions shown in Figure 5.14.	117

Bibliography

- [1] Albert Einstein. Approximative integration of the field equations of gravitation. *Sitzungsber. Preuss. Akad. Wiss. Berlin (Math. Phys.)*, 1916:688–696, 1916.
- [2] Albert Einstein. Über gravitationswellen. *Sitzungsberichte der Königlich Preussischen Akademie der Wissenschaften (Berlin)*, Seite 154-167., 1918.
- [3] Michele Maggiore. *Gravitational Waves: Volume 1: Theory and Experiments*, volume 1. Oxford university press, 2008.
- [4] Bernard Schutz. *A first course in general relativity*. Cambridge university press, 2009.
- [5] B. S. Sathyaprakash and Bernard F. Schutz. Physics, astrophysics and cosmology with gravitational waves. *Living Reviews in Relativity*, 12(1):2, Dec 2009.
- [6] Dimmelmeier, H., Font, J. A., and Müller, E. Relativistic simulations of rotational core collapse ii. collapse dynamics and gravitational radiation. *A&A*, 393(2):523–542, 2002.
- [7] H. Dimmelmeier, C. D. Ott, H.-T. Janka, A. Marek, and E. Müller. Generic gravitational-wave signals from the collapse of rotating stellar cores. *Phys. Rev. Lett.*, 98:251101, Jun 2007.
- [8] The LIGO Scientific Collaboration, J Aasi, B P Abbott, et al. Advanced ligo. *Classical and Quantum Gravity*, 32(7):074001, mar 2015.
- [9] F Acernese et al. *Classical and Quantum Gravity*, 32(2):024001, dec 2014.
- [10] T. Akutsu et al. Kagra: 2.5 generation interferometric gravitational wave detector. *Nature Astronomy*, 3(1):35–40, Jan 2019.
- [11] F Matichard et al. Seismic isolation of advanced ligo: Review of strategy, instrumentation and performance. *Classical and Quantum Gravity*, 32(18):185003, aug 2015.
- [12] F Acernese et al. Advanced virgo: a second-generation interferometric gravitational wave detector. *Classical and Quantum Gravity*, 32(2):024001, dec 2014.
- [13] M. Bailes et al. Gravitational-wave physics and astronomy in the 2020s and 2030s. *Nature Reviews Physics*, 3(5):344–366, May 2021.

-
- [14] Gregory Harry, Timothy P. Bodiya, and Riccardo DeSalvo. Optical Coatings and Thermal Noise in Precision Measurement. 2012.
- [15] V.B. Braginsky and S.P. Vyatchanin. Thermodynamical fluctuations in optical mirror coatings. *Physics Letters A*, 312(3):244–255, 2003.
- [16] M. Tse et al. Quantum-enhanced advanced ligo detectors in the era of gravitational-wave astronomy. *Phys. Rev. Lett.*, 123:231107, Dec 2019.
- [17] M. G. Beker et al. Improving the sensitivity of future gw observatories in the 1–10 hz band: Newtonian and seismic noise. *General Relativity and Gravitation*, 43(2):623–656, Feb 2011.
- [18] David Reitze et al. Cosmic explorer: The u.s. contribution to gravitational-wave astronomy beyond ligo, 2019.
- [19] M Punturo et al. The einstein telescope: a third-generation gravitational wave observatory. *Classical and Quantum Gravity*, 27(19):194002, sep 2010.
- [20] Marica Branchesi et al. Science with the einstein telescope: a comparison of different designs. *Journal of Cosmology and Astroparticle Physics*, 2023(07):068, July 2023.
- [21] R X Adhikari et al. A cryogenic silicon interferometer for gravitational-wave detection. *Classical and Quantum Gravity*, 37(16):165003, jul 2020.
- [22] K. Ackley et al. Neutron Star Extreme Matter Observatory: A kilohertz-band gravitational-wave detector in the global network. *PASA*, 37:e047, November 2020.
- [23] Pau Amaro-Seoane et al. Laser interferometer space antenna, 2017.
- [24] Jun Luo, Li-Sheng Chen, Hui-Zong Duan, Yun-Gui Gong, Shoucun Hu, Jianghui Ji, Qi Liu, Jianwei Mei, Vadim Milyukov, Mikhail Sazhin, Cheng-Gang Shao, Viktor T Toth, Hai-Bo Tu, Yamin Wang, Yan Wang, Hsien-Chi Yeh, Ming-Sheng Zhan, Yonghe Zhang, Vladimir Zharov, and Ze-Bing Zhou. Tianqin: a space-borne gravitational wave detector. *Classical and Quantum Gravity*, 33(3):035010, January 2016.
- [25] Wen-Rui Hu and Yue-Liang Wu. The taiji program in space for gravitational wave physics and the nature of gravity. *National Science Review*, 4(5):685–686, 10 2017.
- [26] Seiji Kawamura et al. Space gravitational-wave antennas DECIGO and B-DECIGO. *International Journal of Modern Physics D*, 28(12):1845001, January 2019.
- [27] Seiji Kawamura et al. Current status of space gravitational wave antenna decigo and b-decigo, 2020.
- [28] Jan Harms et al. Lunar Gravitational-wave Antenna. *Astrophys. J.*, 910(1):1, 2021.

-
- [29] B. P. Abbott, R. Abbott, T. D. Abbott, et al. Observation of gravitational waves from a binary black hole merger. *Physical Review Letters*, 116(6):061102, 2016.
- [30] B. P. Abbott et al. Tests of general relativity with gw150914. *Physical Review Letters*, 116(22):221101, 2016.
- [31] B. P. Abbott et al. Gw170817: Observation of gravitational waves from a binary neutron star inspiral. *Physical Review Letters*, 119(16):161101, 2017.
- [32] B. P. Abbott et al. Multi-messenger observations of a binary neutron star merger. *The Astrophysical Journal Letters*, 848(2):L12, 2017.
- [33] B. P. Abbott et al. Gravitational waves and gamma-rays from a binary neutron star merger: Gw170817 and grb 170817a. *The Astrophysical Journal Letters*, 848(2):L13, 2017.
- [34] D. Kasen, B. Metzger, J. Barnes, E. Quataert, and E. Ramirez-Ruiz. Origin of the heavy elements in binary neutron-star mergers from a gravitational-wave event. *Nature*, 551:80–84, 2017.
- [35] B. D. Metzger. Kilonovae. *Living Reviews in Relativity*, 20(1):3, 2017.
- [36] B. P. Abbott et al. A gravitational-wave standard siren measurement of the hubble constant. *Nature*, 551:85–88, 2017.
- [37] R. Abbott et al. Gw190412: Observation of a binary-black-hole coalescence with asymmetric masses. *Physical Review D*, 102(4):043015, 2020.
- [38] R. Abbott et al. Gw190521: A binary black hole merger with a total mass of 150 m_{\odot} . *Physical Review Letters*, 125(10):101102, 2020.
- [39] R. Abbott et al. Properties and astrophysical implications of the 150 m_{\odot} binary black hole merger gw190521. *The Astrophysical Journal Letters*, 900(1):L13, 2020.
- [40] R. Abbott et al. Gw190814: Gravitational waves from the coalescence of a 23 solar mass black hole with a 2.6 solar mass compact object. *The Astrophysical Journal Letters*, 896(2):L44, 2020.
- [41] R. Abbott et al. Gw190425: Observation of a compact binary coalescence with total mass $\sim 3.4m_{\odot}$. *The Astrophysical Journal Letters*, 892(1):L3, 2020.
- [42] R. Abbott et al. Observation of gravitational waves from two neutron star–black hole coalescences. *The Astrophysical Journal Letters*, 915(1):L5, 2021.
- [43] R. Abbott et al. Population properties of compact objects from the second ligo-virgo gravitational-wave transient catalog. *The Astrophysical Journal Letters*, 913(1):L7, 2021.
- [44] R. Abbott et al. Gwtc-3: Compact binary coalescences observed by ligo and virgo during the second part of the third observing run. *arXiv e-prints*, 2021.

-
- [45] R. Abbott et al. Population of merging compact binaries inferred using gravitational waves through gwtc-3. *Phys. Rev. X*, 13:011048, Mar 2023.
- [46] B. P. Abbott et al. Gw170817: Measurements of neutron star radii and equation of state. *Phys. Rev. Lett.*, 121:161101, Oct 2018.
- [47] Brian D. Metzger. Kilonovae. *Living Reviews in Relativity*, 23(1):1, Dec 2019.
- [48] Masamune Oguri. Effect of gravitational lensing on the distribution of gravitational waves from distant binary black hole mergers. *Monthly Notices of the Royal Astronomical Society*, 480(3):3842–3855, 08 2018.
- [49] Otto A Hannuksela, Thomas E Collett, Mesut Çalışkan, and Tjonnie G F Li. Localizing merging black holes with sub-arcsecond precision using gravitational-wave lensing. *Monthly Notices of the Royal Astronomical Society*, 498(3):3395–3402, 08 2020.
- [50] Samson H. W. Leong, Justin Janquart, Aditya Kumar Sharma, Paul Martens, Parameswaran Ajith, and Otto A. Hannuksela. Constraining binary mergers in AGN disks using the non-observation of lensed gravitational waves. 8 2024.
- [51] Giovanni Tambalo, Miguel Zumalacárregui, Liang Dai, and Mark Ho-Yeuk Cheung. Gravitational wave lensing as a probe of halo properties and dark matter. 12 2022.
- [52] Mesut Çalışkan, Neha Anil Kumar, Lingyuan Ji, Jose M. Ezquiaga, Roberto Cotesta, Emanuele Berti, and Marc Kamionkowski. Probing wave-optics effects and low-mass dark matter halos with lensing of gravitational waves from massive black holes. *Physical Review D*, 108(12), December 2023.
- [53] Anuj Mishra, N. V. Krishnendu, and Apratim Ganguly. Unveiling microlensing biases in testing general relativity with gravitational waves, 2023.
- [54] Srashti Goyal, Aditya Vijaykumar, Jose María Ezquiaga, and Miguel Zumalacárregui. Probing lens-induced gravitational-wave birefringence as a test of general relativity. *Phys. Rev. D*, 108:024052, Jul 2023.
- [55] S. Basak, A. Ganguly, K. Haris, S. Kapadia, A. K. Mehta, and P. Ajith. Constraints on compact dark matter from gravitational wave microlensing. *The Astrophysical Journal Letters*, 926(2):L28, February 2022.
- [56] A. Barsode, S. J. Kapadia, and P. Ajith. Constraints on Compact Dark Matter from the Nonobservation of Gravitational-wave Strong Lensing. *Astrophys. J.*, 975(1):48, 2024.
- [57] Souvik Jana, Shasvath J. Kapadia, Tejaswi Venumadhav, and Parameswaran Ajith. Cosmography using strongly lensed gravitational waves from binary black holes. *Phys. Rev. Lett.*, 130:261401, Jun 2023.

-
- [58] Souvik Jana, Shasvath J. Kapadia, Tejaswi Venumadhav, Surhud More, and Parameswaran Ajith. Probing the nature of dark matter using strongly lensed gravitational waves from binary black holes, 2024.
- [59] Emilio E. Falco Peter Schneider, Jürgen Ehlers. Gravitational lenses. Oct 1999.
- [60] Ramesh Narayan and Matthias Bartelmann. Lectures on gravitational lensing. *arXiv*, 1996. Formation of Structure in the Universe, Proceedings of the 1995 Jerusalem Winter School.
- [61] Takahiro T. Nakamura. Gravitational lensing of gravitational waves from inspiraling binaries by a point mass lens. *Phys. Rev. Lett.*, 80:1138–1141, Feb 1998.
- [62] Ryuichi Takahashi and Takashi Nakamura. Wave Effects in the Gravitational Lensing of Gravitational Waves from Chirping Binaries. *ApJ*, 595(2):1039–1051, October 2003.
- [63] Massimo Meneghetti. Introduction to gravitational lensing: Lecture scripts. Lecture Notes.
- [64] Ryuichi Takahashi and Takashi Nakamura. Wave effects in the gravitational lensing of gravitational waves from chirping binaries. *The Astrophysical Journal*, 595(2):1039, oct 2003.
- [65] Peter Schneider, Jürgen Ehlers, and Emilio E. Falco. *Gravitational Lenses*. Astronomy and Astrophysics Library. Springer-Verlag, Berlin, 1992.
- [66] David W. Hogg. Distance measures in cosmology, 2000.
- [67] W. L. Burke. Multiple Gravitational Imaging by Distributed Masses. *ApJL*, 244:L1, February 1981.
- [68] Prasenjit Saha. Lensing degeneracies revisited. *The Astronomical Journal*, 120(4):1654, oct 2000.
- [69] M. V. Gorenstein, E. E. Falco, and I. I. Shapiro. Degeneracies in Parameter Estimates for Models of Gravitational Lens Systems. *ApJ*, 327:693, April 1988.
- [70] Simon Birrer and Adam Amara. Lenstronomy: multi-purpose gravitational lens modelling software package, 2018.
- [71] Simon Birrer et al. lenstronomy ii: A gravitational lensing software ecosystem. *Journal of Open Source Software*, 6(62):3283, 2021.
- [72] Planck Collaboration, Aghanim, N., Akrami, Y., Ashdown, M., Aumont, J., and others. Planck 2018 results - vi. cosmological parameters. *A&A*, 641:A6, 2020.
- [73] Michael T. Busha, Fred C. Adams, Risa H. Wechsler, and August E. Evrard. Future evolution of cosmic structure in an accelerating universe. *The Astrophysical Journal*, 596(2):713, oct 2003.

- [74] P. J. E. Peebles. *The large-scale structure of the universe*. 1980.
- [75] T. Padmanabhan. *Structure Formation in the Universe*. 1993.
- [76] Houjun Mo, Frank C. van den Bosch, and Simon White. *Galaxy Formation and Evolution*. 2010.
- [77] Aurel Schneider. Dark matter structures and the free streaming scale. 2012.
- [78] William H. Press and Paul Schechter. Formation of Galaxies and Clusters of Galaxies by Self-Similar Gravitational Condensation. *ApJ*, 187:425–438, February 1974.
- [79] M. Davis, G. Efstathiou, C. S. Frenk, and S. D. M. White. The evolution of large-scale structure in a universe dominated by cold dark matter. *ApJ*, 292:371–394, May 1985.
- [80] Juhan Kim, Changbom Park, and Sang-Min Lee. The new horizon run cosmological n-body simulations. *Journal of The Korean Astronomical Society*, 44(6):217–234.
- [81] Samuel W. Skillman, Michael S. Warren, Matthew J. Turk, Risa H. Wechsler, Daniel E. Holz, and P. M. Sutter. Dark sky simulations: Early data release, 2014.
- [82] Neal Katz, David H. Weinberg, and Lars Hernquist. Cosmological simulations with treesph. *The Astrophysical Journal Supplement Series*, 105:19, July 1996.
- [83] Y. Dubois, Pichon, et al. Dancing in the dark: galactic properties trace spin swings along the cosmic web. *Monthly Notices of the Royal Astronomical Society*, 444(2):1453–1468, 08 2014.
- [84] Nishikanta Khandai, Tiziana Di Matteo, Rupert Croft, Stephen Wilkins, Yu Feng, Evan Tucker, Colin DeGraf, and Mao-Sheng Liu. The massiveblack-ii simulation: the evolution of haloes and galaxies to $z \sim 0$. *Monthly Notices of the Royal Astronomical Society*, 450(2):1349–1374, April 2015.
- [85] M. Vogelsberger, Genel, et al. Properties of galaxies reproduced by a hydrodynamic simulation. *Nature*, 509(7499):177–182, 5 2014.
- [86] Joop Schaye, Crain, et al. The eagle project: simulating the evolution and assembly of galaxies and their environments. *Monthly Notices of the Royal Astronomical Society*, 446(1):521–554, 11 2014.
- [87] S. G. Murray, C. Power, and A. S. G. Robotham. How well do we know the halo mass function? *Monthly Notices of the Royal Astronomical Society: Letters*, 434(1):L61–L65, July 2013.
- [88] Zarija Lukić, Katrin Heitmann, Salman Habib, Sergei Bashinsky, and Paul M. Ricker. The Halo Mass Function: High-Redshift Evolution and Universality. *ApJ*, 671(2):1160–1181, December 2007.

-
- [89] Suman Bhattacharya, Katrin Heitmann, Martin White, Zarija Lukić, Christian Wagner, and Salman Habib. Mass Function Predictions Beyond Λ CDM. *ApJ*, 732(2):122, May 2011.
- [90] Aurel Schneider, Robert E. Smith, and Darren Reed. Halo mass function and the free streaming scale. *Monthly Notices of the Royal Astronomical Society*, 433(2):1573–1587, 06 2013.
- [91] Ravi K. Sheth, H. J. Mo, and Giuseppe Tormen. Ellipsoidal collapse and an improved model for the number and spatial distribution of dark matter haloes. *Monthly Notices of the Royal Astronomical Society*, 323(1):1–12, 05 2001.
- [92] Martin White. The mass function. *The Astrophysical Journal Supplement Series*, 143(2):241–255, December 2002.
- [93] Peter S. Behroozi, Risa H. Wechsler, and Charlie Conroy. The average star formation histories of galaxies in dark matter halos from $z = 0$ –8. *The Astrophysical Journal*, 770(1):57, may 2013.
- [94] A. Jenkins, C. S. Frenk, S. D. M. White, J. M. Colberg, S. Cole, A. E. Evrard, H. M. P. Couchman, and N. Yoshida. The mass function of dark matter haloes. *Monthly Notices of the Royal Astronomical Society*, 321(2):372–384, 02 2001.
- [95] S. G. Murray, C. Power, and A. S. G. Robotham. HMFcalc: An online tool for calculating dark matter halo mass functions. *Astronomy and Computing*, 3:23–34, November 2013.
- [96] Michele Maggiore, Chris Van Den Broeck, Nicola Bartolo, et al. Science case for the einstein telescope. *Journal of Cosmology and Astroparticle Physics*, 2020(03):050, mar 2020.
- [97] Matthew Evans, Alessandra Corsi, Chaitanya Afle, Alena Ananyeva, K. G. Arun, et al. Cosmic explorer: A submission to the nsf mpsac nggw subcommittee, 2023.
- [98] Evan D Hall and Matthew Evans. Metrics for next-generation gravitational-wave detectors. *Classical and Quantum Gravity*, 36(22):225002, oct 2019.
- [99] Bernard F. Schutz. Determining the hubble constant from gravitational wave observations. *Nature*, 323(6086):310–311, Sep 1986.
- [100] Daniel E. Holz and Scott A. Hughes. Using gravitational-wave standard sirens. *The Astrophysical Journal*, 629(1):15, aug 2005.
- [101] Hsin-Yu Chen, Maya Fishbach, and Daniel E Holz. A two per cent hubble constant measurement from standard sirens within five years. *Nature*, 562(7728):545–547, 2018.
- [102] Will M. Farr, Maya Fishbach, Jiani Ye, and Daniel Holz. A Future Percent-Level Measurement of the Hubble Expansion at Redshift 0.8 With Advanced LIGO. *Astrophys. J. Lett.*, 883(2):L42, 2019.

- [103] Zhi-Qiang You, Xing-Jiang Zhu, Gregory Ashton, Eric Thrane, and Zong-Hong Zhu. Standard-siren cosmology using gravitational waves from binary black holes. *Astrophys. J.*, 908(2):215, 2021.
- [104] Jose María Ezquiaga and Daniel E. Holz. Spectral Sirens: Cosmology from the Full Mass Distribution of Compact Binaries. *Phys. Rev. Lett.*, 129(6):061102, 2022.
- [105] Banafsheh Shiralilou, Geert Raaijmakers, Bastien Duboef, Samaya Nissanke, Francois Foucart, Tanja Hinderer, and Andrew Williamson. Measuring Hubble Constant with Dark Neutron Star-Black Hole Mergers. 7 2022.
- [106] Nabila Aghanim, Yashar Akrami, Mark Ashdown, J Aumont, C Baccigalupi, M Ballardini, AJ Banday, RB Barreiro, N Bartolo, S Basak, et al. Planck 2018 results-vi. cosmological parameters. *Astronomy & Astrophysics*, 641:A6, 2020.
- [107] Adam G. Riess, Wenlong Yuan, Lucas M. Macri, Dan Scolnic, Dillon Brout, Stefano Casertano, David O. Jones, Yukei Murakami, Gagandeep S. Anand, Louise Breuval, Thomas G. Brink, Alexei V. Filippenko, Samantha Hoffmann, Saurabh W. Jha, W. D’arcy Kenworthy, John Mackenty, Benjamin E. Stahl, and WeiKang Zheng. A comprehensive measurement of the local value of the hubble constant with 1 km s⁻¹ mpc⁻¹ uncertainty from the hubble space telescope and the sh0es team. *The Astrophysical Journal Letters*, 934(1):L7, jul 2022.
- [108] Adam G. Riess. The expansion of the universe is faster than expected. *Nature Reviews Physics*, 2(1):10–12, Jan 2020.
- [109] Jian-Ping Hu and Fa-Yin Wang. Hubble tension: The evidence of new physics. *Universe*, 9(2), 2023.
- [110] D. Scolnic et al. How many kilonovae can be found in past, present, and future survey data sets? *The Astrophysical Journal*, 852(1):L3, dec 2017.
- [111] M. Fishbach, R. Gray, I. Magaña Hernandez, et al. A standard siren measurement of the hubble constant from gw170817 without the electromagnetic counterpart. *The Astrophysical Journal Letters*, 871(1):L13, jan 2019.
- [112] Francesca Calore, Alessandro Cuoco, Tania Regimbau, Surabhi Sachdev, and Pasquale Dario Serpico. Cross-correlating galaxy catalogs and gravitational waves: A tomographic approach. *Phys. Rev. Res.*, 2:023314, Jun 2020.
- [113] Suvodip Mukherjee, Alex Krolewski, Benjamin D. Wandelt, and Joseph Silk. Cross-correlating dark sirens and galaxies: measurement of h_0 from gwtc-3 of ligo-virgo-kagra, 2022.
- [114] Jonathan R. Gair, Archisman Ghosh, Rachel Gray, Daniel E. Holz, Simone Mastroianni, Suvodip Mukherjee, Antonella Palmese, Nicola Tamanini, Tessa Baker, Freija Beirnaert, Maciej Bilicki, Hsin-Yu Chen, Gergely Dály, Jose Maria Ezquiaga, Will M. Farr, Maya Fishbach, Juan Garcia-Bellido, Tathagata Ghosh, Hsiang-Yu Huang, Christos Karathanasis, Konstantin Leyde, Ignacio Magaña

- Hernandez, Johannes Noller, Gregoire Pierra, Peter Raffai, Antonio Enea Romano, Monica Seglar-Arroyo, Danièle A. Steer, Cezary Turcki, Maria Paola Vaccaro, and Sergio Andrés Vallejo-Peña. The hitchhiker's guide to the galaxy catalog approach for dark siren gravitational-wave cosmology. *The Astronomical Journal*, 166(1):22, jun 2023.
- [115] Nicola Borghi, Michele Mancarella, Michele Moresco, Matteo Tagliazucchi, Francesco Iacovelli, Andrea Cimatti, and Michele Maggiore. Cosmology and astrophysics with standard sirens and galaxy catalogs in view of future gravitational wave observations. *The Astrophysical Journal*, 964(2):191, March 2024.
- [116] J.M. Lattimer. Neutron stars and the nuclear matter equation of state. *Annual Review of Nuclear and Particle Science*, 71(Volume 71, 2021):433–464, 2021.
- [117] S. E. Woosley, S. Blinnikov, and Alexander Heger. Pulsational pair instability as an explanation for the most luminous supernovae. *Nature*, 450(7168):390–392, Nov 2007.
- [118] Belczynski, K., Heger, A., Gladysz, W., Ruiter, A. J., Woosley, S., Wiktorowicz, G., Chen, H.-Y., Bulik, T., O'Shaughnessy, R., Holz, D. E., Fryer, C. L., and Berti, E. The effect of pair-instability mass loss on black-hole mergers. *A&A*, 594:A97, 2016.
- [119] S. E. Woosley. Pulsational pair-instability supernovae. *The Astrophysical Journal*, 836(2):244, feb 2017.
- [120] A. Heger and S. E. Woosley. The nucleosynthetic signature of population iii. *The Astrophysical Journal*, 567(1):532, mar 2002.
- [121] S. Mastrogiovanni, K. Leyde, C. Karathanasis, E. Chassande-Mottin, D. A. Steer, J. Gair, A. Ghosh, R. Gray, S. Mukherjee, and S. Rinaldi. On the importance of source population models for gravitational-wave cosmology. *Phys. Rev. D*, 104(6):062009, 2021.
- [122] Suvodip Mukherjee. The redshift dependence of black hole mass distribution: is it reliable for standard sirens cosmology? *Mon. Not. Roy. Astron. Soc.*, 515(4):5495–5505, 2022.
- [123] C. Messenger and J. Read. Measuring a cosmological distance-redshift relationship using only gravitational wave observations of binary neutron star coalescences. *Phys. Rev. Lett.*, 108:091101, 2012.
- [124] T. G. F. Li, W. Del Pozzo, and C. Messenger. Measuring the redshift of standard sirens using the neutron star deformability. In *13th Marcel Grossmann Meeting on Recent Developments in Theoretical and Experimental General Relativity, Astrophysics, and Relativistic Field Theories*, pages 2019–2021, 2015.
- [125] C. Messenger, Kentaro Takami, Sarah Gossan, Luciano Rezzolla, and B. S. Sathyaprakash. Source Redshifts from Gravitational-Wave Observations of Binary Neutron Star Mergers. *Phys. Rev. X*, 4(4):041004, 2014.

-
- [126] Jose María Ezquiaga and Daniel E. Holz. Jumping the gap: Searching for ligo’s biggest black holes. *The Astrophysical Journal Letters*, 909(2):L23, March 2021.
- [127] Jose María Ezquiaga and Daniel E. Holz. Spectral sirens: Cosmology from the full mass distribution of compact binaries. *Physical Review Letters*, 129(6), August 2022.
- [128] Hsin-Yu Chen, Jose María Ezquiaga, and Ish Gupta. Cosmography with next-generation gravitational wave detectors, 2024.
- [129] Enis Belgacem, Yves Dirian, Stefano Foffa, and Michele Maggiore. Modified gravitational-wave propagation and standard sirens. *Phys. Rev. D*, 98(2):023510, 2018.
- [130] Michele Mancarella, Edwin Genoud-Prachex, and Michele Maggiore. Cosmology and modified gravitational wave propagation from binary black hole population models. *Phys. Rev. D*, 105:064030, Mar 2022.
- [131] Aditya Vijaykumar, M. V. S. Saketh, Sumit Kumar, Parameswaran Ajith, and Tirthankar Roy Choudhury. Probing the large scale structure using gravitational-wave observations of binary black holes. *Phys. Rev. D*, 108:103017, Nov 2023.
- [132] Sumit Kumar, Aditya Vijaykumar, and Alexander H. Nitz. Detecting baryon acoustic oscillations with third-generation gravitational wave observatories. *The Astrophysical Journal*, 930(2):113, may 2022.
- [133] Shun-Sheng Li, Shude Mao, Yuetong Zhao, and Youjun Lu. Gravitational lensing of gravitational waves: a statistical perspective. *MNRAS*, 476(2):2220–2229, May 2018.
- [134] Ken K. Y. Ng, Kaze W. K. Wong, Tom Broadhurst, and Tjonnie G. F. Li. Precise LIGO lensing rate predictions for binary black holes. *Phys. Rev. D*, 97(2):023012, January 2018.
- [135] Fei Xu, Jose María Ezquiaga, and Daniel E. Holz. Please repeat: Strong lensing of gravitational waves as a probe of compact binary and galaxy populations. *The Astrophysical Journal*, 929(1):9, apr 2022.
- [136] Lilan Yang, Shichao Wu, Kai Liao, Xuheng Ding, Zhiqiang You, Zhoujian Cao, Marek Biesiada, and Zong-Hong Zhu. Event rate predictions of strongly lensed gravitational waves with detector networks and more realistic templates. *Monthly Notices of the Royal Astronomical Society*, 509(3):3772–3778, 11 2021.
- [137] Ish Gupta, Chaitanya Afle, K. G. Arun, Ananya Bandopadhyay, et al. Characterizing gravitational wave detector networks: From a[#] to cosmic explorer, 2024.
- [138] Graham P Smith, Andrew Robertson, Guillaume Mahler, et al. Discovering gravitationally lensed gravitational waves: predicted rates, candidate selection, and localization with the Vera Rubin Observatory. *Monthly Notices of the Royal Astronomical Society*, 520(1):702–721, 01 2023.

- [139] A. Renske A. C. Wierda, Ewoud Wempe, Otto A. Hannuksela, Léon V. E. Koopmans, and Chris Van Den Broeck. Beyond the detector horizon: Forecasting gravitational-wave strong lensing. *The Astrophysical Journal*, 921(2):154, November 2021.
- [140] K. Haris, Ajit Kumar Mehta, Sumit Kumar, Tejaswi Venumadhav, and Parameswaran Ajith. Identifying strongly lensed gravitational wave signals from binary black hole mergers, 2018.
- [141] Ewoud Wempe, Léon V. E. Koopmans, A. Renske A. C. Wierda, Otto Akseli Hannuksela, and Chris van den Broeck. A lensing multi-messenger channel: Combining ligo-virgo-kagra lensed gravitational-wave measurements with euclid observations, 2022.
- [142] S. Birrer, M. Millon, D. Sluse, A. J. Shajib, F. Courbin, L. V. E. Koopmans, S. H. Suyu, and T. Treu. Time-Delay Cosmography: Measuring the Hubble Constant and other cosmological parameters with strong gravitational lensing. 10 2022.
- [143] Kai Liao, Xi-Long Fan, Xu-Heng Ding, Marek Biesiada, and Zong-Hong Zhu. Precision cosmology from future lensed gravitational wave and electromagnetic signals. *Nature Commun.*, 8(1):1148, 2017. [Erratum: *Nature Commun.* 8, 2136 (2017)].
- [144] Joshua A. Frieman, Bruce Bassett, et al. The Sloan Digital Sky Survey-II Supernova Survey: Technical Summary. *AJ*, 135(1):338–347, January 2008.
- [145] R. Kessler, J. Marriner, et al. The difference imaging pipeline for the transient search in the dark energy survey. *The Astronomical Journal*, 150(6):172, nov 2015.
- [146] Eric C. Bellm. The zwicky transient facility, 2014.
- [147] LSST Science Collaboration, Paul A. Abell, et al. Lsst science book, version 2.0, 2009.
- [148] R. Hounsell, D. Scolnic, R. J. Foley, et al. Simulations of the wfirst supernova survey and forecasts of cosmological constraints. *The Astrophysical Journal*, 867(1):23, October 2018.
- [149] Scott D. Barthelmy et al. The burst alert telescope (bat) on the swift midex mission. *Space Science Reviews*, 120(3):143–164, Oct 2005.
- [150] Adam Goldstein, Rachel Hamburg, et al. Updates to the fermi gbm targeted sub-threshold search in preparation for the third observing run of ligo/virgo, 2019.
- [151] Mandana Amiri, Bridget C. Andersen, et al. The first chime/frb fast radio burst catalog. *The Astrophysical Journal Supplement Series*, 257(2):59, December 2021.
- [152] Christopher S. Kochanek. The Analysis of Gravitational Lens Surveys. II. Maximum Likelihood Models and Singular Potentials. *ApJ*, 419:12, December 1993.

- [153] Christopher S. Kochanek. Is There a Cosmological Constant? *ApJ*, 466:638, August 1996.
- [154] C. S. Kochanek. The Saas Fee Lectures on strong gravitational lensing. In *33rd Advanced Saas Fee Course on Gravitational Lensing: Strong, Weak, and Micro*, 7 2004.
- [155] Kyu-Hyun Chae. Cosmological Parameters from the SDSS DR5 Velocity Dispersion Function of Early-Type Galaxies through Radio-selected Lens Statistics. *ApJL*, 658(2):L71–L74, April 2007.
- [156] Masamune Oguri. Gravitational Lens Time Delays: A Statistical Assessment of Lens Model Dependences and Implications for the Global Hubble Constant. *ApJ*, 660(1):1–15, May 2007.
- [157] Dan Coe and Leonidas A. Moustakas. Cosmological Constraints from Gravitational Lens Time Delays. *ApJ*, 706(1):45–59, November 2009.
- [158] David Harvey. A 4 per cent measurement of H_0 using the cumulative distribution of strong lensing time delays in doubly imaged quasars. *MNRAS*, 498(2):2871–2886, October 2020.
- [159] Alessandro Sonnenfeld. Statistical strong lensing. II. Cosmology and galaxy structure with time-delay lenses. *A&A*, 656:A153, December 2021.
- [160] Dan Maoz. Quasar lensing statistics and $\Omega(\Lambda)$: What went wrong? *IAU Symp.*, 225:413, 2005.
- [161] Salvatore Vitale, Will M. Farr, Ken K. Y. Ng, and Carl L. Rodriguez. Measuring the star formation rate with gravitational waves from binary black holes. *The Astrophysical Journal Letters*, 886(1):L1, nov 2019.
- [162] M. Sereno, Ph. Jetzer, A. Sesana, and M. Volonteri. Cosmography with strong lensing of LISA gravitational wave sources. *Monthly Notices of the Royal Astronomical Society*, 415(3):2773–2781, 08 2011.
- [163] Otto A Hannuksela, Thomas E Collett, Mesut Çalışkan, and Tjonnie G F Li. Localizing merging black holes with sub-arcsecond precision using gravitational-wave lensing. *Monthly Notices of the Royal Astronomical Society*, 498(3):3395–3402, 08 2020.
- [164] Xikai Shan, Xuechun Chen, Bin Hu, and Rong-Gen Cai. Microlensing sheds light on the detection of strong lensing gravitational waves, 2023.
- [165] Michal Dominik, Krzysztof Belczynski, Christopher Fryer, Daniel E. Holz, Emanuele Berti, Tomasz Bulik, Ilya Mandel, and Richard O’Shaughnessy. Double compact objects. ii. cosmological merger rates. *The Astrophysical Journal*, 779(1):72, nov 2013.
- [166] Masamune Oguri, Atsushi Taruya, Yasushi Suto, and Edwin L. Turner. Strong gravitational lensing time delay statistics and the density profile of dark halos. *The Astrophysical Journal*, 568(2):488, apr 2002.

- [167] Peter S. Behroozi, Risa H. Wechsler, and Charlie Conroy. The Average Star Formation Histories of Galaxies in Dark Matter Halos from $z = 0-8$. *ApJ*, 770(1):57, June 2013.
- [168] Michal Dominik, Krzysztof Belczynski, Christopher Fryer, Daniel E Holz, Emanuele Berti, Tomasz Bulik, Ilya Mandel, and Richard O’Shaughnessy. Double compact objects. ii. cosmological merger rates. *The Astrophysical Journal*, 779(1):72, 2013.
- [169] Krzysztof Belczynski, Vassiliki Kalogera, and Tomasz Bulik. A comprehensive study of binary compact objects as gravitational wave sources: Evolutionary channels, rates, and physical properties. *The Astrophysical Journal*, 572(1):407, jun 2002.
- [170] Krzysztof Belczynski, Vassiliki Kalogera, et al. Compact object modeling with the startrack population synthesis code. *The Astrophysical Journal Supplement Series*, 174(1):223, jan 2008.
- [171] Pavel Kroupa, Christopher A. Tout, and Gerard Gilmore. The distribution of low-mass stars in the galactic disc. *Monthly Notices of the Royal Astronomical Society*, 262(3):545–587, 06 1993.
- [172] Pavel Kroupa and Carsten Weidner. Galactic-field initial mass functions of massive stars. *The Astrophysical Journal*, 598(2):1076, dec 2003.
- [173] Louis-Gregory Strolger, Adam G. Riess, Tomas Dahlen, et al. The hubble higher z supernova search: Supernovae to $z \approx 1.6$ and constraints on type ia progenitor models*. *The Astrophysical Journal*, 613(1):200, sep 2004.
- [174] Krzysztof Belczynski, Daniel E. Holz, Tomasz Bulik, and Richard O’Shaughnessy. The first gravitational-wave source from the isolated evolution of two stars in the 40–100 solar mass range. *Nature*, 534(7608):512–515, Jun 2016.
- [175] Piero Madau and Mark Dickinson. Cosmic star-formation history. *Annual Review of Astronomy and Astrophysics*, 52(1):415–486, 2014.
- [176] Steven Murray, Chris Power, and Aaron Robotham. Hmfcalc: An online tool for calculating dark matter halo mass functions, 2013.
- [177] Stefano Rinaldi and Walter Del Pozzo. (H)DPGMM: a hierarchy of Dirichlet process Gaussian mixture models for the inference of the black hole mass function. *Mon. Not. Roy. Astron. Soc.*, 509(4):5454–5466, 2021.
- [178] Ravi K. Sheth, H. J. Mo, and Giuseppe Tormen. Ellipsoidal collapse and an improved model for the number and spatial distribution of dark matter haloes. *Monthly Notices of the Royal Astronomical Society*, 323(1):1–12, 05 2001.
- [179] Jeremy Tinker, Andrey V. Kravtsov, Anatoly Klypin, Kevork Abazajian, Michael Warren, Gustavo Yepes, Stefan Gottlöber, and Daniel E. Holz. Toward a halo mass

- function for precision cosmology: The limits of universality. *The Astrophysical Journal*, 688(2):709, dec 2008.
- [180] E.E. Falco, M.V. Gorenstein, and I.I. Shapiro. On model-dependent bounds on H_0 from gravitational images : application to Q 0957+561 A, B. *ApJ*, 289:L1–L4, February 1985.
- [181] C. S. Kochanek. What do gravitational lens time delays measure? *The Astrophysical Journal*, 578(1):25, oct 2002.
- [182] Jason S.C. Poon, Stefano Rinaldi, Justin Janquart, Harsh Narola, and Otto A. Hannuksela. Galaxy lens reconstruction based on strongly lensed gravitational waves: similarity transformation degeneracy and mass-sheet degeneracy.
- [183] Justin Janquart, Anupreeta More, and Chris Van Den Broeck. Ordering the confusion: a study of the impact of lens models on gravitational-wave strong lensing detection capabilities. *Monthly Notices of the Royal Astronomical Society*, 519(2):2046–2059, 12 2022.
- [184] Mesut Çalışkan, Jose María Ezquiaga, Otto A. Hannuksela, and Daniel E. Holz. Lensing or luck? false alarm probabilities for gravitational lensing of gravitational waves. *Phys. Rev. D*, 107:063023, Mar 2023.
- [185] Gianfranco Bertone and Dan Hooper. History of dark matter. *Rev. Mod. Phys.*, 90:045002, Oct 2018.
- [186] A. Arbey and F. Mahmoudi. Dark matter and the early universe: A review. *Progress in Particle and Nuclear Physics*, 119:103865, 2021.
- [187] Bernard Carr and Florian Kühnel. Primordial black holes as dark matter candidates. *SciPost Physics Lecture Notes*, may 2022.
- [188] Kim Griest and Marc Kamionkowski. Supersymmetric dark matter. *Physics Reports*, 333-334:167–182, 2000.
- [189] Jonathan L. Feng. Dark matter candidates from particle physics and methods of detection. *Annual Review of Astronomy and Astrophysics*, 48(1):495–545, 2010.
- [190] Anne M Green and Bradley J Kavanagh. Primordial black holes as a dark matter candidate. *Journal of Physics G: Nuclear and Particle Physics*, 48(4):043001, feb 2021.
- [191] S. D. M. White, C. S. Frenk, and M. Davis. Clustering in a neutrino-dominated universe. *ApJ*, 274:L1–L5, November 1983.
- [192] M. Kawasaki, Naoshi Sugiyama, and T. Yanagida. Gravitino warm dark matter motivated by gauge-mediated supersymmetry breaking theories. *Modern Physics Letters A*, 12(17):1275–1282, 1997.
- [193] A. Boyarsky, M. Drewes, T. Lasserre, S. Mertens, and O. Ruchayskiy. Sterile neutrino dark matter. *Progress in Particle and Nuclear Physics*, 104:1–45, 2019.

- [194] E. Komatsu, K. M. Smith, J. Dunkley, C. L. Bennett, B. Gold, G. Hinshaw, N. Jarosik, D. Larson, M. R. Nolta, L. Page, D. N. Spergel, M. Halpern, R. S. Hill, A. Kogut, M. Limon, S. S. Meyer, N. Odegard, G. S. Tucker, J. L. Weiland, E. Wollack, and E. L. Wright. Seven-year wilkinson microwave anisotropy probe (wmap*) observations: Cosmological interpretation. *The Astrophysical Journal Supplement Series*, 192(2):18, jan 2011.
- [195] Shaun Cole, Will J. Percival, John A. Peacock, Peder Norberg, Carlton M. Baugh, Carlos S. Frenk, Ivan Baldry, Joss Bland-Hawthorn, Terry Bridges, Russell Cannon, Matthew Colless, Chris Collins, Warrick Couch, Nicholas J. G. Cross, Gavin Dalton, Vincent R. Eke, Roberto de Propris, Simon P. Driver, George Efstathiou, Richard S. Ellis, Karl Glazebrook, Carole Jackson, Adrian Jenkins, Ofer Lahav, Ian Lewis, Stuart Lumsden, Steve Maddox, Darren Madgwick, Bruce A. Peterson, Will Sutherland, Keith Taylor, and The 2dFGRS Team. The 2dF Galaxy Redshift Survey: power-spectrum analysis of the final data set and cosmological implications. *Monthly Notices of the Royal Astronomical Society*, 362(2):505–534, 09 2005.
- [196] Max Tegmark, Daniel J. Eisenstein, Michael A. Strauss, David H. Weinberg, Michael R. Blanton, Joshua A. Frieman, Masataka Fukugita, James E. Gunn, Andrew J. S. Hamilton, Gillian R. Knapp, Robert C. Nichol, Jeremiah P. Ostriker, Nikhil Padmanabhan, Will J. Percival, David J. Schlegel, Donald P. Schneider, Roman Scoccimarro, Uro š Seljak, Hee-Jong Seo, Molly Swanson, Alexander S. Szalay, Michael S. Vogeley, Jaiyul Yoo, Idit Zehavi, Kevork Abazajian, Scott F. Anderson, James Annis, Neta A. Bahcall, Bruce Bassett, Andreas Berlind, Jon Brinkmann, Tamás Budavari, Francisco Castander, Andrew Connolly, Istvan Csabai, Mamoru Doi, Douglas P. Finkbeiner, Bruce Gillespie, Karl Glazebrook, Gregory S. Hennesy, David W. Hogg, Željko Ivezić, Bhuvnesh Jain, David Johnston, Stephen Kent, Donald Q. Lamb, Brian C. Lee, Huan Lin, Jon Loveday, Robert H. Lupton, Jeffrey A. Munn, Kaike Pan, Changbom Park, John Peoples, Jeffrey R. Pier, Adrian Pope, Michael Richmond, Constance Rockosi, Ryan Scranton, Ravi K. Sheth, Albert Stebbins, Christopher Stoughton, István Szapudi, Douglas L. Tucker, Daniel E. Vanden Berk, Brian Yanny, and Donald G. York. Cosmological constraints from the sdss luminous red galaxies. *Phys. Rev. D*, 74:123507, Dec 2006.
- [197] G. Kauffmann, S. D. M. White, and B. Guiderdoni. The formation and evolution of galaxies within merging dark matter haloes. *Monthly Notices of the Royal Astronomical Society*, 264(1):201–218, 09 1993.
- [198] Anatoly Klypin, Andrey V. Kravtsov, Octavio Valenzuela, and Francisco Prada. Where are the missing galactic satellites? *The Astrophysical Journal*, 522(1):82, sep 1999.
- [199] Ben Moore, Sebastiano Ghigna, Fabio Governato, George Lake, Thomas Quinn, Joachim Stadel, and Paolo Tozzi. Dark matter substructure within galactic halos. *The Astrophysical Journal*, 524(1):L19, sep 1999.
- [200] Paul Bode, Jeremiah P. Ostriker, and Neil Turok. 556(1):93, jul 2001.

- [201] Stacy Y. Kim, Annika H. G. Peter, and Jonathan R. Hargis. Missing Satellites Problem: Completeness Corrections to the Number of Satellite Galaxies in the Milky Way are Consistent with Cold Dark Matter Predictions. *Phys. Rev. Lett.*, 121(21):211302, 2018.
- [202] W. J. G. de Blok. The core-cusp problem. *Advances in Astronomy*, 2010:1–14, 2010.
- [203] David N. Spergel and Paul J. Steinhardt. Observational evidence for self-interacting cold dark matter. *Physical Review Letters*, 84(17):3760–3763, April 2000.
- [204] Wayne Hu, Rennan Barkana, and Andrei Gruzinov. Fuzzy cold dark matter: The wave properties of ultralight particles. *Physical Review Letters*, 85(6):1158–1161, August 2000.
- [205] Matteo Viel, George D. Becker, James S. Bolton, and Martin G. Haehnelt. Warm dark matter as a solution to the small scale crisis: New constraints from high redshift lyman- α forest data. *Phys. Rev. D*, 88:043502, Aug 2013.
- [206] Katarina Markovič and Matteo Viel. Lyman- α forest and cosmic weak lensing in a warm dark matter universe. *Publications of the Astronomical Society of Australia*, 31:e006, 2014.
- [207] Christophe Yèche, Nathalie Palanque-Delabrouille, Julien Baur, and Héliou du Mas des Bourboux. Constraints on neutrino masses from lyman-alpha forest power spectrum with boss and xq-100. *Journal of Cosmology and Astroparticle Physics*, 2017(06):047, jun 2017.
- [208] Bruno Villaseñor, Brant Robertson, Piero Madau, and Evan Schneider. New constraints on warm dark matter from the lyman- α forest power spectrum. *Phys. Rev. D*, 108:023502, Jul 2023.
- [209] S. Vegetti, S. Birrer, G. Despali, C. D. Fassnacht, D. Gilman, Y. Hezaveh, L. Perreault Levasseur, J. P. McKean, D. M. Powell, C. M. O’Riordan, and G. Vernardos. Strong gravitational lensing as a probe of dark matter, 2023.
- [210] Wolfgang Enzi, Riccardo Murgia, Oliver Newton, Simona Vegetti, Carlos Frenk, Matteo Viel, Marius Cautun, Christopher D Fassnacht, Matt Auger, Giulia Despali, John McKean, Léon V E Koopmans, and Mark Lovell. Joint constraints on thermal relic dark matter from strong gravitational lensing, the Ly α forest, and Milky Way satellites. *Monthly Notices of the Royal Astronomical Society*, 506(4):5848–5862, 07 2021.
- [211] Ryan E Keeley, A M Nierenberg, et al. Jwst lensed quasar dark matter survey – ii. strongest gravitational lensing limit on the dark matter free streaming length to date. *Monthly Notices of the Royal Astronomical Society*, 535(2):1652–1671, 11 2024.
- [212] Brandon Bozek, David J. E. Marsh, Joseph Silk, and Rosemary F. G. Wyse. Galaxy UV-luminosity function and reionization constraints on axion dark matter. *Monthly Notices of the Royal Astronomical Society*, 450(1):209–222, 04 2015.

- [213] Hsi-Yu Schive, Tzihong Chiueh, Tom Broadhurst, and Kuan-Wei Huang. Contrasting galaxy formation from quantum wave dark matter, ψ_{dm} , with λcdm , using planck and hubble data. *The Astrophysical Journal*, 818(1):89, feb 2016.
- [214] P. S. Corasaniti, S. Agarwal, D. J. E. Marsh, and S. Das. Constraints on dark matter scenarios from measurements of the galaxy luminosity function at high redshifts. *Phys. Rev. D*, 95:083512, Apr 2017.
- [215] Vid Iršič, Matteo Viel, Martin G. Haehnelt, James S. Bolton, and George D. Becker. First constraints on fuzzy dark matter from lyman- α forest data and hydrodynamical simulations. *Phys. Rev. Lett.*, 119:031302, Jul 2017.
- [216] David J. E. Marsh and Jens C. Niemeyer. Strong constraints on fuzzy dark matter from ultrafaint dwarf galaxy eridanus ii. *Phys. Rev. Lett.*, 123:051103, Jul 2019.
- [217] Neal Dalal and Andrey Kravtsov. Not so fuzzy: excluding fdm with sizes and stellar kinematics of ultra-faint dwarf galaxies, 2022.
- [218] Gianfranco Bertone, Djuna Croon, Mustafa A. Amin, Kimberly K. Boddy, Bradley J. Kavanagh, Katherine J. Mack, Priyamvada Natarajan, Toby Opferkuch, Katelin Schutz, Volodymyr Takhistov, Christoph Weniger, and Tien-Tien Yu. Gravitational wave probes of dark matter: challenges and opportunities. *arXiv e-prints*, page arXiv:1907.10610, July 2019.
- [219] Pau Amaro-Seoane and Heather Audley et al. Laser interferometer space antenna, 2017.
- [220] Bradley J. Kavanagh, David A. Nichols, Gianfranco Bertone, and Daniele Gaggero. Detecting dark matter around black holes with gravitational waves: Effects of dark-matter dynamics on the gravitational waveform. *Phys. Rev. D*, 102:083006, Oct 2020.
- [221] Kenji Kadota, Jeong Han Kim, Pyungwon Ko, and Xing-Yu Yang. Gravitational wave probes on self-interacting dark matter surrounding an intermediate mass black hole, 2023.
- [222] Brito Richard, Cardoso Vitor, and Pani Paolo. Superradiance. Jul 2015.
- [223] Asimina Arvanitaki and Sergei Dubovsky. Exploring the string axiverse with precision black hole physics. *Phys. Rev. D*, 83:044026, Feb 2011.
- [224] Asimina Arvanitaki, Masha Baryakhtar, and Xinlu Huang. Discovering the qcd axion with black holes and gravitational waves. *Phys. Rev. D*, 91:084011, Apr 2015.
- [225] Richard Brito, Shrobana Ghosh, Enrico Barausse, Emanuele Berti, Vitor Cardoso, Irina Dvorkin, Antoine Klein, and Paolo Pani. Gravitational wave searches for ultralight bosons with ligo and lisa. *Phys. Rev. D*, 96:064050, Sep 2017.
- [226] Masha Baryakhtar, Robert Lasenby, and Mae Teo. Black hole superradiance signatures of ultralight vectors. *Phys. Rev. D*, 96:035019, Aug 2017.

- [227] Nataliya K. Porayko, Xingjiang Zhu, Yuri Levin, Lam Hui, et al. Parkes pulsar timing array constraints on ultralight scalar-field dark matter. *Phys. Rev. D*, 98:102002, Nov 2018.
- [228] Liang Dai, Shun-Sheng Li, Barak Zackay, Shude Mao, and Youjun Lu. Detecting lensing-induced diffraction in astrophysical gravitational waves. *Phys. Rev. D*, 98:104029, Nov 2018.
- [229] Masamune Oguri and Ryuichi Takahashi. Probing dark low-mass halos and primordial black holes with frequency-dependent gravitational lensing dispersions of gravitational waves. *The Astrophysical Journal*, 901(1):58, sep 2020.
- [230] Han Gil Choi, Chanung Park, and Sunghoon Jung. Small-scale shear: Peeling off diffuse subhalos with gravitational waves. *Phys. Rev. D*, 104:063001, Sep 2021.
- [231] Zucheng Gao, Xian Chen, Yi-Ming Hu, Jian-Dong Zhang, and Shun-Jia Huang. A higher probability of detecting lensed supermassive black hole binaries by LISA. *Monthly Notices of the Royal Astronomical Society*, 512(1):1–10, 02 2022.
- [232] Xiao Guo and Youjun Lu. Probing the nature of dark matter via gravitational waves lensed by small dark matter halos. *Phys. Rev. D*, 106:023018, Jul 2022.
- [233] Mesut Çalışkan, Neha Anil Kumar, Lingyuan Ji, Jose M. Ezquiaga, Roberto Cotesta, Emanuele Berti, and Marc Kamionkowski. Probing wave-optics effects and dark-matter subhalos with lensing of gravitational waves from massive black holes, 2023.
- [234] Shuo Cao, Jingzhao Qi, Marek Biesiada, Tonghua Liu, Jin Li, and Zong-Hong Zhu. Measuring the viscosity of dark matter with strongly lensed gravitational waves. *Monthly Notices of the Royal Astronomical Society: Letters*, 502(1):L16–L20, 12 2020.
- [235] Cao, Shuo, Qi, Jingzhao, Cao, Zhoujian, Biesiada, Marek, Cheng, Wei, and Zhu, Zong-Hong. Direct measurement of the distribution of dark matter with strongly lensed gravitational waves. *A&A*, 659:L5, 2022.
- [236] Evan D Hall and Matthew Evans. Metrics for next-generation gravitational-wave detectors. *Classical and Quantum Gravity*, 36(22):225002, 2019.
- [237] K. Haris, Ajit Kumar Mehta, Sumit Kumar, Tejaswi Venumadhav, and Parameswaran Ajith. Identifying strongly lensed gravitational wave signals from binary black hole mergers. *arXiv e-prints*, page arXiv:1807.07062, July 2018.
- [238] Fei Xu, Jose Maria Ezquiaga, and Daniel E. Holz. Please Repeat: Strong Lensing of Gravitational Waves as a Probe of Compact Binary and Galaxy Populations. *Astrophys. J.*, 929(1):9, 2022.
- [239] Shun-Sheng Li, Shude Mao, Yuetong Zhao, and Youjun Lu. Gravitational lensing of gravitational waves: A statistical perspective. *Mon. Not. Roy. Astron. Soc.*, 476(2):2220–2229, 2018.

- [240] Suvodip Mukherjee, Tom Broadhurst, Jose M. Diego, Joseph Silk, and George F. Smoot. Impact of astrophysical binary coalescence time-scales on the rate of lensed gravitational wave events. *Mon. Not. Roy. Astron. Soc.*, 506(3):3751–3759, 2021.
- [241] Andrew Robertson, Graham P. Smith, Richard Massey, Vincent Eke, Mathilde Jauzac, Matteo Bianconi, and Dan Ryczanowski. What does strong gravitational lensing? The mass and redshift distribution of high-magnification lenses. *MNRAS*, 495(4):3727–3739, July 2020.
- [242] Justin Janquart, Anupreeta More, and Chris Van Den Broeck. Ordering the confusion: A study of the impact of lens models on gravitational-wave lensing detection capabilities. *arXiv e-prints*, page arXiv:2205.11499, May 2022.
- [243] Anupreeta More and Surhud More. Improved statistic to identify strongly lensed gravitational wave events. *Mon. Not. Roy. Astron. Soc.*, 515(1):1044–1051, 2022.
- [244] Michele Maggiore, Chris Van Den Broeck, Nicola Bartolo, Enis Belgacem, Daniele Bertacca, Marie Anne Bizouard, Marica Branchesi, Sebastien Clesse, Stefano Foffa, Juan García-Bellido, et al. Science case for the einstein telescope. *Journal of Cosmology and Astroparticle Physics*, 2020(03):050, 2020.
- [245] David Reitze, Rana X. Adhikari, Stefan Ballmer, Barry Barish, Lisa Barsotti, Gari-Lynn Billingsley, Duncan A. Brown, Yanbei Chen, Dennis Coyne, Robert Eisenstein, Matthew Evans, Peter Fritschel, Evan D. Hall, Albert Lazzarini, Geoffrey Lovelace, Jocelyn Read, B. S. Sathyaprakash, David Shoemaker, Joshua Smith, Calum Torrie, Salvatore Vitale, Rainer Weiss, Christopher Wipf, and Michael Zucker. Cosmic Explorer: The U.S. Contribution to Gravitational-Wave Astronomy beyond LIGO. In *Bulletin of the American Astronomical Society*, volume 51, page 35, September 2019.
- [246] Adrian Jenkins, CS Frenk, Simon DM White, Jorg M Colberg, Shaun Cole, August E Evrard, HMP Couchman, and N Yoshida. The mass function of dark matter haloes. *Monthly Notices of the Royal Astronomical Society*, 321(2):372–384, 2001.
- [247] J. M. Bardeen, J. R. Bond, N. Kaiser, and A. S. Szalay. The Statistics of Peaks of Gaussian Random Fields. *ApJ*, 304:15, May 1986.
- [248] Matteo Viel, Julien Lesgourgues, Martin G. Haehnelt, Sabino Matarrese, and Antonio Riotto. Constraining warm dark matter candidates including sterile neutrinos and light gravitinos with wmap and the lyman- α forest. *Phys. Rev. D*, 71:063534, Mar 2005.
- [249] Aurel Schneider, Robert E. Smith, Andrea V. Macciò, and Ben Moore. Non-linear evolution of cosmological structures in warm dark matter models. *Monthly Notices of the Royal Astronomical Society*, 424(1):684–698, 07 2012.
- [250] Souvik Jana, Shasvath J Kapadia, Tejaswi Venumadhav, Surhud More, and Parameswaran Ajith. Strong-lensing cosmography using third-generation gravitational-wave detectors, 2024.

-
- [251] R Abbott, TD Abbott, F Acernese, K Ackley, C Adams, N Adhikari, RX Adhikari, VB Adya, C Affeldt, D Agarwal, et al. Gwtc-3: Compact binary coalescences observed by ligo and virgo during the second part of the third observing run. *arXiv preprint arXiv:2111.03606*, 2021.
- [252] R. Abbott et al. Population of merging compact binaries inferred using gravitational waves through gwtc-3. *Phys. Rev. X*, 13:011048, Mar 2023.
- [253] Salvatore Vitale and Matthew Evans. Parameter estimation for binary black holes with networks of third-generation gravitational-wave detectors. *Phys. Rev. D*, 95:064052, Mar 2017.
- [254] Thomas E. Collett. The population of galaxy–galaxy strong lenses in forthcoming optical imaging surveys. *The Astrophysical Journal*, 811(1):20, sep 2015.
- [255] Srashti Goyal, Harikrishnan D., Shasvath J. Kapadia, and Parameswaran Ajith. Rapid identification of strongly lensed gravitational-wave events with machine learning. *Phys. Rev. D*, 104:124057, Dec 2021.
- [256] Xiaoshu Liu, Ignacio Magaña Hernandez, and Jolien Creighton. Identifying strong gravitational-wave lensing during the second observing run of advanced ligo and advanced virgo. *The Astrophysical Journal*, 908(1):97, February 2021.
- [257] Anupreeta More and Surhud More. Improved statistic to identify strongly lensed gravitational wave events. *Monthly Notices of the Royal Astronomical Society*, 515(1):1044–1051, 06 2022.
- [258] Justin Janquart, K Haris, Otto A Hannuksela, and Chris Van Den Broeck. The return of golum: improving distributed joint parameter estimation for strongly lensed gravitational waves. *Monthly Notices of the Royal Astronomical Society*, 526(2):3088–3098, 09 2023.
- [259] Jose María Ezquiaga, Wayne Hu, and Rico K. L. Lo. Identifying strongly lensed gravitational waves through their phase consistency. *Phys. Rev. D*, 108:103520, Nov 2023.
- [260] Rico K. L. Lo and Ignacio Magaña Hernandez. Bayesian statistical framework for identifying strongly lensed gravitational-wave signals. *Phys. Rev. D*, 107:123015, Jun 2023.
- [261] Sourabh Magare, Anupreeta More, and Sunil Choudhary. Slick: Strong lensing identification of candidates kindred in gravitational wave data. *Monthly Notices of the Royal Astronomical Society*, 535(1):990–999, 10 2024.
- [262] A. Barsode, S. Goyal, and P. Ajith. Fast and efficient bayesian method to search for strongly lensed gravitational waves, 2024.
- [263] Aniruddha Chakraborty and Suvodip Mukherjee. Glance – gravitational lensing authenticator using non-modelled cross-correlation exploration of gravitational

- wave signals. *Monthly Notices of the Royal Astronomical Society*, 532(4):4842–4863, 07 2024.
- [264] Souvik Jana, Shasvath J Kapadia, Tejaswi Venumadhav, Surhud More, and Parameswaran Ajith. Strong-lensing cosmography using third-generation gravitational-wave detectors. *Classical and Quantum Gravity*, 41(24):245010, nov 2024.
- [265] Scott Tremaine and James E. Gunn. Dynamical role of light neutral leptons in cosmology. *Phys. Rev. Lett.*, 42:407–410, Feb 1979.
- [266] Andrea V. Macciò, Sinziana Paduroiu, Donnino Anderhalden, Aurel Schneider, and Ben Moore. Cores in warm dark matter haloes: a catch 22 problem. *Monthly Notices of the Royal Astronomical Society*, 424(2):1105–1112, 08 2012.
- [267] Craig J. Hogan and Julianne J. Dalcanton. New dark matter physics: Clues from halo structure. *Phys. Rev. D*, 62:063511, Aug 2000.
- [268] Francisco Villaescusa-Navarro and Neal Dalal. Cores and cusps in warm dark matter halos. *Journal of Cosmology and Astroparticle Physics*, 2011(03):024, mar 2011.
- [269] R. Kormann, P. Schneider, and M. Bartelmann. Isothermal elliptical gravitational lens models. *A&A*, 284:285–299, April 1994.
- [270] Liang Dai and Tejaswi Venumadhav. On the waveforms of gravitationally lensed gravitational waves, 2017.
- [271] A. Burkert. Fuzzy dark matter and dark matter halo cores. *The Astrophysical Journal*, 904(2):161, nov 2020.
- [272] Souvik Jana, Shasvath J Kapadia, Tejaswi Venumadhav, Surhud More, and Parameswaran Ajith. Effect of lens models on strong lensing cosmography using gravitational waves. In Prep.
- [273] Vishal Baibhav, Emanuele Berti, Davide Gerosa, Michela Mapelli, Nicola Giacobbo, Yann Bouffanais, and Ugo N. Di Carlo. Gravitational-wave detection rates for compact binaries formed in isolation: Ligo/virgo o3 and beyond. *Phys. Rev. D*, 100:064060, Sep 2019.
- [274] K N Maity et al. Constraining dark matter substructure using multi-messenger observations of binary neutron star mergers.
- [275] Peter Fritschel, Kevin Kuns, Jenne Driggers, et al. LSC Post-O5 Study Group, Report of the lsc post-o5 study group. *LIGO-T2200287-v3*, 2024.
- [276] R X Adhikari, Koji Arai, Aidan Brooks, et al. LIGO Voyager. *LIGO-M2300123*, 2024.
- [277] R X Adhikari, K Arai, A F Brooks, C Wipf, O Aguiar, et al. A cryogenic silicon interferometer for gravitational-wave detection. *Classical and Quantum Gravity*, 37(16):165003, jul 2020.

- [278] K N Maity, Souvik Jana, Tejaswi Venumadhav, and Parameswaran Ajith. Strong-lensing cosmography using upgraded second-generation gravitational-wave detectors.